

ABSTRACT

Novak, James Paul *Synthesis, Optical and Electronic Investigations of Organically Bridged Metal Nanoparticle Arrays* (North Carolina State University, Under the direction of Dan L. Feldheim)

The study of metal nanoparticles has been a growing field over the past 10 years. Many investigations have been performed that investigate the optical and electronic properties of these nanoparticles. Studies have been published that show the properties of individual nanoparticles and also large aggregates of nanoparticles. An area that has been largely ignored is the effect of symmetry and interparticle distance on electronic and optical coupling. This has largely been due to the lack of synthetic methods that allow precise control over the number of particles in an array, the symmetry that these particles obtain, and the interparticle distance in these arrays.

This dissertation will discuss methods for synthesizing organic bridges that template the interparticle geometry to molecular dimensions. The discussion continues with characterization of these nanoparticle arrays. The role of symmetry and interparticle distance will be in the forefront as these nanoparticle arrays are investigated for linear electromagnetic coupling and non-linear optical response. Spectroscopy will be shown that directly addresses the position of this linking bridge. In addition, electrochemical behavior is shown as a function of interparticle coupling.

*Synthesis, Optical and Electronic Investigations of Organically Bridged
Metal Nanoparticle Arrays*

James Paul Novak

A Dissertation submitted in partial fulfillment of the
Requirements by the North Carolina State University
Department of Chemistry for the Degree of
Doctor of Philosophy

Raleigh, June 2001

Approved by:

Daniel L. Feldheim
Chair of Advisory Committee

Christopher B. Gorman

Edmond F. Bowden

Kenneth W. Hanck

Dedication

I dedicate this work to my Pop-Pop. He was my inspiration to never stop learning and achieve the highest level in everything I do.

Personal Biography

James Paul Novak was born January 16, 1972 in New Jersey. Within a few months his parents moved him to Raleigh, NC where they remained until high school.

After graduating from Cocoa Beach H.S. in Florida he returned to the University of North Carolina at Wilmington. While completing a B.S. in Chemistry at UNCW, he worked with Prof. S. Bart Jones doing undergraduate research. The focus of this research was investigating band-broadening mechanisms in HPLC sponsored by the YMC Corp., now owned by Waters, Inc. During his senior year at UNCW he met his now wife, Margaret Trussell Clarke. After graduation in 1994, the market was slim for chemists. Several years of paying rent by mowing lawns and working at a bicycle shop passed before starting to work at BASF in Research Triangle Park. During this time, the acceptance letter arrived to attend the Graduate Program in the Department of Chemistry at North Carolina State University. After completing the first year of classes, Jamie was the first student to join the research group of then new Professor Dan Feldheim. About this same time, Jamie and Margie were married, June 14, 1997. The next 4 years were full of hard work performing exciting new science. The outcome of these past few years is outlined in the following chapters.

Acknowledgements

I would like to thank my wife Margie for putting up with me and giving me so much support over the past few years. I would like to thank all my family for encouragement through the tough times. I would like to thank my advisor, Professor Dan Feldheim, for the invaluable knowledge that I have gained. I would like to thank all the members of the Feldheim Group for making graduate school fun.

TABLE OF CONTENTS

List of Figures and Schemes	ix
List of Tables	xiv
Preface	xv
Chapter One: Introduction and Background	1
Chapter One References.....	11
Scope	15
Chapter Two: Synthesis of Phenyl-Acetylene Bridges for Nanoparticle	
Templates	16
Introduction	17
General Reaction Procedures	24
Synthesis	29
Chapter Two References	61
Chapter Three: Synthesis of Organically Bridged Metal Nanoparticle	
Arrays	62
Introduction	63
Experimental	65
Results and Discussion: Au Nanoparticle Arrays	69
Results and Discussion: Ag Nanoparticle Arrays	74

Conclusions	77
Chapter Three References	78
Chapter Four: Electromagnetic Coupling in Organically- Bridged	
Nanoparticle Arrays.	80
Introduction	81
Theoretical Considerations	82
Experimental	86
Results and Discussion: Au Nanoparticle Arrays	87
Results and Discussion: Ag Nanoparticle Arrays	93
Conclusions	99
Chapter Four References	100
Chapter Five: Non-Linear Optical Properties of Symmetrically Controlled	
Nanoparticle Arrays	102
Introduction	103
Background	104
Experimental	108
Results and Discussion	110
Conclusions	117
Chapter Five References	119

Chapter Six: Single Molecule Surface Enhanced Raman Spectroscopy of Organized Nanoparticle Arrays	121
Introduction	122
Experimental	126
Results and Discussion	127
Conclusions	136
Chapter Six References	138
Chapter Seven: Electronic Coupling in Nanoparticle Arrays	140
Introduction	141
Experimental	146
Results and Discussion: Thiolate Covered Nanoparticle Dimers	148
Results and Discussion: PPh ₃ Nanoparticle Dimers	152
Conclusions	156
Chapter Seven References	158
Chapter Eight: Separation Methods for Organically Bridged Nanoparticle Arrays	159
Introduction	160
Experimental	162
Results and Discussion: Centrifugation Methods	163
Results and Discussion: HPLC-GPC Methods	167

Conclusions	171
Chapter Eight References	173
Reflection	184

List of Figures and Schemes

Scheme 2.1. Proposed Linking Procedure	17
Scheme 2.2. Mechanism for Pd(0)/Cu catalyzed Heck Coupling.....	18
Scheme 2.3. Synthetic route to linear molecular bridges.....	22
Scheme 2.4. Synthetic route to trigonal planer molecular bridges	23
Scheme 2.5. Synthetic route to tetrahedral molecular bridges.....	24
Scheme 2.6. Synthetic route to porphyrin based molecular bridges	25
Figure 3.1. Phenyl acetylene based linking bridge structures.	66
Figure 3.2. Transmission Electron Microscopy images of templated nanoparticle dimers. Images show that nanoparticles are not touching. Symmetry matches that of PA7-2 linker used in experiment	70
Figure 3.3. Transmission Electron Microscopy images showing 10 nm Au nanoparticle trimers. Longer linker, PA3-3 shows greater interparticle distance compared to PA2-3.	71
Figure 3.4. Transmission Electron Microscopy images of Au nanoparticle arrays. PA4-4 (top) linker yields 10 nm tetrahedral array symmetry. Tetra-thiol porphyrin (bottom) yield square planar 5 nm nanoparticle arrays.	72
Figure 3.5. TEM images of 30 nm Ag dimers. Particle arrays were linked with PA7-2 (top) and PA3-2 (bottom).	75

Figure 3.6. Transmission Electron Microscopy images of 10 nm Ag trimers using PA3-3.	76
Figure 4.1. Resultant UV-VIS absorbance spectrum obtained by adding 10 nm Au nanoparticle sol to linker solution. Broadband absorbance at 600nm is characteristic of irreversible aggregation.	88
Figure 4.2. UV-VIS spectra for 10nm Au trimers vs. time. No change in the surface plasmon resonance was observed over one hour.....	89
Figure 4.3. UV-VIS spectra for 10 nm Au dimers vs. time. Overall time change is 40 min.	90
Figure 4.4. Calculated extinction maxima for Au nanoparticle arrays as a function of symmetry. Adapted from ref. 7b.....	91
Figure 4.5. Calculated extinction spectra compared to experimental observations for Au dimers (black) and monomers (red). Calculated spectra were corrected for concentration and orientation averaging in solution. Courtesy of Colby A. Foss, Jr.	92
Figure 4.6. Molecular Structures of phenylacetylene linkers used to template Ag dimers.....	94
Figure 4.7. UV Vis spectra of 30 nm Ag dimers as a function of interparticle separation. Scans are offset for clarity.	95
Figure 4.8. Calculated extinction spectra for 60 nm Ag dimers as a function of separation distance. Adapted from reference 11	96

Figure 5.1. Schematic of Hyper Rayleigh Scattering apparatus	108
Figure 5.2. Hyper Rayleigh Scattering Plot.	110
Figure 5.3. Concentration dependence plot for nanoparticle arrays. First Hyperpolarizability values are calculated from the slope of linear fit....	111
Figure 5.4. Molecular structures of phenylacetylene bridges used in HRS experiments.	114
Scheme 6.1. Cartoon of apparatus for obtaining dark-field or Raman images (A.) and Raman spectrum (B.).....	128
Figure 6.1. Atomic Force Microscopy image of 30 nm Ag dimers on Quartz. Marked particles indicate dimer structures	129
Figure 6.2. Dark-field (A.) and Raman (B.) images of 30nm Ag nanoparticle dimers. Marked particle scatters in both images.	130
Figure 6.3. Single molecule SERS spectrum for phenylacetylene based nanoparticle linker. Marked peaks correspond with positions normally assigned for molecular functional groups	131
Figure 6.4. Concurrent SERS images of 30 nm Ag dimers. Scans are obtained using one second integration times at 10 second intervals. Marked particles exhibit “blinking” associated with single molecule spectroscopy	132
Figure 6.5. Polarization dependence of SERS spectra of 30nm PA7-2 linked Ag dimers.....	134

Figure 6.6. Cartoon of expected results from SERS polarization experiments. Single linkers will only be observed at specific angles. Multiple linkers could be observed at multiple angles.	135
Figure 7.1. Possible mechanisms for peak splitting for redox events on coupled nanoparticle dimers. Also shown are possible shifts in the voltammogram that would be observed based on each mechanism.	145
Figure 7.2. Differential pulse voltammogram of C8-SH coated Au nanoparticles. Scan taken in 50 mM Bu ₄ NClO ₄ in DCM	149
Figure 7.3. Differential pulse voltammograms of C8-SH coated Au nanoparticles. Monomer (blue) and PA7-2 linked (red) scans taken in 50 mM Bu ₄ NClO ₄ in DCM	150
Figure 7.4. Differential pulse voltammograms of C8-SH coated Au nanoparticles. Monomer (blue) and PA3-2 linked (red) scans taken in 50 mM Bu ₄ NClO ₄ in DCM	151
Figure 7.5. Differential pulse voltammograms of PPh ₃ coated Au nanoparticle dimers vs. separation distance. Monomers (green), PA7-2 (blue) and PA3-2 (red) scans were taken in 50 mM Bu ₄ NClO ₄ in DCM.....	153
Figure 7.6. Data fit (green) to voltammogram (red) of PA3-2 linked PPh ₃ coated Au nanoparticles. Deconvolution shows that $\Delta E = 150$ mV.....	155

Figure 8.1. TEM images of trimer (top) and dimer (bottom) Au nanoparticle arrays separated by centrifugation	164
Figure 8.2. Histogram noting TEM derived nanoparticle dimer array concentrations pre- (left) and post- (right) separation. Desired nanoparticle array concentrations is increased by separation.....	165
Figure 8.3. Histogram noting TEM derived nanoparticle trimer array concentrations pre- (left) and post- (right) separation. Desired nanoparticle array concentrations is increased by separation.....	166
Figure 8.4. HPLC-GPC chromatograms of a) 10 nm Au, b) 30nm Au, c) mixture of 10 nm and 30 nm Au nanoparticles.....	168
Figure 8.5. HPLC-GPC chromatograms of Au nanoparticle monomers and linked dimers, trimers, and tetramers.....	169

List of Tables

Table 5.1. Selected first hyperpolarizability values for Au nanoparticle arrays. Values are corrected based on TEM derived concentrations.	112
Table 5.2. Comparison of first hyperpolarizability values of nanoparticle trimers to well known molecular chromophores.	117
Table 7.1. Calculated ΔE values based on interparticle separation.....	156
Table 8.1. Percentage of nanoparticle arrays before and after centrifugation by centrifugation.	164
Table 8.2. Retention times of peaks from chromatograms in Figure 8.5.....	170
Table 8.3. Percentage of nanoparticle composition from dimer sample separated using HPLC-GPC methods.....	170

Preface

Many changes in our lives have happened over the past century. We have seen science direct our lives with the development of the electronic and communications age. Especially prevalent are the changes in the past 20 years following advances in solid-state circuitry. Moore's Trend Law has predicted that the number of components in a circuit would double every two years. This line is currently being followed and dictates that manufacturing processes will reach a fundamental limit within 10 years. This fact leads us to search for new methods for making smaller electronic components. Through the ability to manipulate small components and incorporate them into manufacturing, nanotechnology has emerged.

Nanotechnology is concerned with the study of things on a sub-micron scale and includes many disciplines of science. Due to this wide coverage, it is not uncommon for biologists, biochemists, chemists, physicists and engineers to work together towards a common goal. The chemist will play an ever-increasing role in nanotechnology as the size requirements dictate manipulation of single molecules or clusters of molecules. This has been shown in the literature over the past few years.

Chapter 1

Introduction and Background

As we enter the new millennium, fast paced lifestyles and consumer demand has pushed the development of smaller electronic devices. It is now commonplace to see portable devices such as phones, radios and computers everywhere you look. One reason for the availability of these devices is advancements in solid state circuit manufacturing. Industry has been increasing the density of chip based components as a way to shrink solid state devices. However, current methods for shrinking integrated devices are reaching their limits.

Following the current rate of miniaturization, Moore's law predicts we will reach the physical limits of current lithographic manufacturing methods within 10 years¹. The closer we get to these limits the more pronounced they become. For example, in photolithography, equipment such as higher power, shorter wavelength lasers allow circuit components to be made in the 100 nm range². However, these techniques require highly specialized alignment of masks, which is slow and costly due to the precision required. In addition, as the components become smaller, the ability to connect them and wire together a circuit is difficult. These types of limitations prompt a need for new methods to manufacture integrated devices. Nanotechnology could be the key that opens the door to ultra-small integrated devices.

For many years chemistry has focused on the study of molecules while engineers and physicists focused on micron scale structures. The size regime in between, from 5-100 nm, was largely ignored until about 10 years ago and now is rich with new discoveries. The ability to study atoms, molecules, and groups of

molecules on a nanometer (10^{-9} m) length scale has emerged following advances in analytical instrumentation. One large branch of research in this size regime is nanoparticles. Nanoparticles have been synthesized with various compositions including metals³, metal oxides⁴, semiconductors⁵, polymers⁶, and hybrids⁷ of these main groups. Many aspects of nanoparticles have been studied. Measurements have been made on solution phase colloidal systems and surface bound⁸ systems. These experiments have shown interesting physical properties. Because of the electronic and optical properties of nanoparticles, they are being used as building blocks for more complex structures.

Richard Feynman had remarkable insight as he proposed more than 50 years ago that there is “plenty of room at the bottom”⁹. He was referring to the ability to manipulate matter on an increasingly smaller, molecular level. Scientists are starting these types of manipulations in several areas, notably chemical and self-assembly and mechanical manipulation.

Mechanical manipulation has emerged as a way to build certain types of nanostructures. The movement of single atoms and molecules across a surface has been shown using an STM¹⁰. Binnig and co-workers first demonstrated this by spelling their company name, IBM, using Xe atoms. The probe tip pushes the atoms across a surface into a desired pattern. This type of work has allowed the study of quantum confinement¹¹ and molecule rotations¹². Nanoparticles have been manipulated using similar methods¹³.

In contrast to mechanical manipulation is chemical or self-assembly. We define chemical assembly as structures made by chemically directed solution phase materials. Self-assembled monolayers (SAM's) are made by chemical assembly. A SAM is an ordered array of molecules on a flat surface. SAM's have been shown to have potential to be used in many ways such as chemical sensors, separations, and protective coatings. Much of the SAM's literature¹⁴ describes thiolates on gold, but molecular assembly is also observed on other substrates.

Chemical assembly has also been shown on colloidal systems. SAM's on nanoparticles have been demonstrated¹⁵. Simple SAM's on nanoparticles were first demonstrated to gain nanoparticle stabilization. Examples include citrates¹⁶ and water-soluble phosphines^{3a,b} for aqueous particles. Non-aqueous alkane thiolates have also been shown to greatly stabilize nanoparticles^{3e} in organic mediums. These particle based SAM's appear to follow the same chemistry that has been developed on flat surfaces. Similar trends developed on a surface apply to nanoparticles that allow for replacement or exchange of the protecting layer to manipulate surface chemistry.

Interesting structures have been made using chemical assembly to direct the assembly of nanoparticles. This suggests that nanoparticles can be used as building blocks to form more complex structures. Ordered films and arrays¹⁷, core-shell structures¹⁸, multi-layer systems¹⁹, polymer capsules²⁰ have all been made using nanoparticles as templates. These might have uses in medical screening²¹, chemical sensing²², single electron devices²³, or catalysis²⁴.

Multi-layer nanoparticle systems have been synthesized using many different techniques. These architectures can be built using electrostatic interactions¹⁹ or covalent bonding²⁵. Electrostatic structures are usually built using poly-cationic cross-linkers combined with anionic nanoparticles. Many covalent systems utilize the di-thiol molecule. The structures can be based on complete coverage of a surface²⁶ or directed coverage²⁷ based on surface patterning. These layered structures also show interesting optical and electronic behaviors, such as .

Nanoparticles have been used as templates for other structures. Core shell structures have been made using several methods¹⁸. Core shell structures have been made using two different metals, for example, by plating a silver layer on a gold nanoparticle. Metal on semiconductor and vice versa have been shown. Additional types of core/shell structures involve attaching a layer of small particles on a single large particle⁴⁵.

Polymer shells have been synthesized on nanoparticles. They were first used to stabilize nanoparticles²⁸ but have also been used as nanovesicles by removing the metal support²⁰. These types of structures can combine metals and inorganic materials.

Multi-particle arrays and films have also been studied. Simple dropcast films show hexagonal symmetry²⁹. Multi particle arrays have been made through aggregation with salt³⁰ or bifunctionalized ligand³¹. Both of these methods proceed without control of aggregation number or symmetry. Complimentary strands of DNA have been shown to aggregate particles³¹. Alkane Di-thiols will aggregate

particles. Careful choice of ligands allows increasing control. Controlling the amount of linking molecule allows more control of aggregation number. This has been shown using selective strands of DNA. Linkers can also be designed to control interparticle shapes and geometry³². This Dissertation will explore building controlled aggregates of nanoparticles with discrete numbers of particles.

As many of these interesting structures are developed they are also explored for optical and electronic behaviors. Depending on the size, nanoparticles can have properties of their bulk counterparts or atomic state³³. For example, Au nanoparticles less than two nanometers show electronic behavior that can be addressed with quantum mechanics. When the particles are larger than two nanometers they can act like free electron metals whose electronic properties are described with classical expressions. Some of the behaviors are described below.

Optical properties of nanoparticles have been known for many centuries. Since the Roman Empire, “Ruby Glass”, composed of Au nanoparticles embedded in glass, has been used in stained glass windows. This red color is from the plasmon resonance. The plasmon resonance is simply based on a delocalized electron cloud that exists on the surface of the nanoparticles³⁴. These electrons absorb light at certain energy and oscillate back and forth with the frequency of light. The plasmon resonance has also been shown on rough surfaces but is not seen on smaller particles less than 2nm. Below this transition point, the electrons exist in quantum energy states. Generally metal particles show a plasmon absorbance in the visible region. The exact position of the plasmon absorbance

depends on many factors, including size, shape, and solvent dielectric constants³⁵. If the specific characteristics are known the plasmon resonance can be a quick analytical tool for analyzing the size and concentration of nanoparticle solutions.

Nanoparticles have shown some interesting optical properties. They have been investigated as single particles and coupled systems. Single particle studies have shown that the plasmon resonance is dependent on surface chemistry. Changes in surface chemistry can be accomplished by switching solvents or capping ligands. Decreasing the solvent dielectric will usually red-shift the plasmon absorbance. This is due to the electrons being damped on the surface. Changing the surface ligand can have a dramatic affect on the optical properties. For example, when alkane-thiolates are bound to the surface of a gold nanoparticle the plasmon resonance all but disappears^{3e,15}.

Optical properties of coupled nanoparticle systems have also been investigated. Nanoparticles can optically couple when they are in close enough proximity to each other so that there is interaction between their plasmon electron clouds. These interactions have been treated theoretically by several groups³⁵, and will be discussed in detail in Chapter 4. This type of optical coupling has been shown to be useful in a DNA sensor³¹. The coupled optical properties have been shown in cast films²⁹ and crosslinked multilayer³³ systems. Optical coupling in discrete nanoparticle arrays has also been investigated^{32b-d}.

Non-linear optical (NLO) behavior has also been reported. Hyper Rayleigh Scattering was reported for Silica particles³⁶. HRS was used as a tool to investigate

the surface interface of a nanoparticle. For possible use in optical devices, metal nanoparticles were studied for second Harmonic Generation using HRS. Incredibly large NLO response was observed for Au nanoparticles³⁷. These results were more impressive when the particles were aggregated with salt showing that symmetry plays a role. This was investigated further showing that decreasing symmetry increases NLO response^{38,39}.

Another area of optical investigation is Surfaced Enhanced Raman Spectroscopy (SERS). It has been shown that nanoparticles show enhancement factors⁴⁰ of 10^6 for Raman spectra compared to a neat solution. Also reported were the “hot” particles, which have specific geometries to maximize the polarization transfer between the surface and analyte. This resulted in enhancement of 10^{14} with dye molecules⁴¹.

In addition to optical properties, electronic behavior of nanoparticles has been investigated. Electronic conduction through individual particles has been investigated using the STM⁴². IV properties showing Coulomb staircases were observed indicating single electron tunneling. It has been shown that the energy of the staircase can be shifted based on the surface chemistry of the particle⁴³.

Combining mainstream techniques like lithography with self-assembly has yielded new nanostructures. This type of measurement removes the mechanical aspect of the STM. Au and CdSe nanoparticles were deposited between lithographically prepared electrodes using wet chemical techniques⁴⁴. Coulomb staircases were observed indicating single electron tunneling characteristics. These

techniques are limited in the requirement for extremely low temperatures to avoid thermal noise.

While studying single particles is fundamentally interesting, bulk electronic measurements can generate similar electronic responses. Charging of nanoparticles is similar to SET behavior. If a nanoparticle is small enough, an energy barrier must be crossed to overcome the electrostatic repulsion between electrons confined to the surface. Adding or removing an electron changes the charge. If nanoparticles are all the same size, they all charge at the same energy, similar to redox events in molecular systems. The charging energy is described using

$$E=e/2C$$

Where e is the fundamental electron charge and C is the capacitance. Collective charging peaks have been observed for monodisperse nanoparticle solutions⁴⁵. These bulk measurements can be done in solution or on a surface⁴⁶.

As described above nanoparticles show many interesting behaviors. Many of these properties show promise towards the development of a single electron, quantum computer. However, there are still areas that need investigating. Assembly methods are making progress but at the present time it is barely possible to make connections to a single nanoparticle for measurements. Seemingly, making connections to 10^{12} single particles to make a network consistent with today's computers seems almost impossible. There needs to be a way to connect to large numbers of discrete particle arrays to meet this demand. In the following chapters, a method for connecting large quantities of nanoparticle arrays with

discrete aggregation numbers ($n = 1, 2, 3, \text{ or } 4$) and with precise geometry and interparticle spacing is described. This may also lead to a way to bridge the size gap between lithographic and molecular systems.

Chapter One References

1. a) Moore's Trend Law, B E Deal, *Interface*, **1997**, 6, 18 b) RR Schaller, *IEEE Spectrum*, **1997**, 6, 53 c) M Schulz, *Nature*, **1999**, 399, 729
2. JC Ellenbogen, "A Brief Overview of Nanoelectronic Devices" Presentation Transcript, GOMAC98, Arlington, VA, June 13-16, 1998
3. a) G. Schmid ed. "Clusters and Colloids" New York, VCH, **1994** b) G. Schmid *Chem. Rev.* **1992**, 92, 1709 and references therein c) **Pt**- TS Ahmadi, ZL Wang, TC Green, A Hengleim, MA El-Sayed, *Science* **1996**, 272, 1924 d) **Pd**- MT Reetz, W. Heilbig, *J. Am. Chem. Soc.*, **1994**, 116, 740 e) **Au** -M Brust, M Walker, D Bethell, JJ Schriffin, RJ Whymann, *Chem Comm.* **1994**, 801; RW Murray, et al *J. Am. Chem. Soc.*, **1996**, 118, 4212 f) **Ag**-PC Ohara, DV Leff, JR Heath, WM Gelbert, *Phys. Rev. Lett.* **1995**, 75, 3466 g) RL Whetten, *Adv. Mat.* **1996**, 8, 428 h) RP Andres, *Science* **1996**, 273, 1690 i) KC Graber, *Langmuir*, **1996**, 12, 2353 k) PC Lee, D Meisel, *J. Phys. Chem.* **1982**, 86, 3391
4. K Ariga, Y Lvov, M Onda, I Ichinose, T kunitake, *Chem, Lett.* 1997, 125; b) YM Lvov, JF Rusling, Dt Thomsen F Papadimitrakopoulos, T Kawakami, T kunitake, *Chem. Comm.* **1998**, 1229
5. a) B Ludolph, M A Malik, P O'Brien, Nrevaprasedu *J. Chem. Soc. Chem. Comm.* **1998**, 1849 b) C B Murray, DJ Norris, MG Bawendi *J. Am. Chem. Soc.*, **1993**, 115, 8706; c) CB Murray, CR Kagen, MG Bawendi, *Science*, **1995**, 270, 1335
6. P Baker, D Matthews, A Hope, *Aust. J. Chem*, **1994**, 47, 1; b) Z Qi, PG Pickup, *Chem. Mater.* **1997**, 9 2394
7. a) SL Wetcott, SJ Oldenburg, TR Lee, NJ Halas, *Chem. Phys. Lett.* **1999**, 30, 651; b) C /barthet, AJ Hickey, DB Cairns, SP Armes, *Adv. Mat.* **1999**, 11 (5) 408
8. a) C Roos, M Schmidt, J Ebenhoch, F. Baumann, B Deubzer, J. Weis, *Adv. Mat.* **1999**, 11, 761; b) RH Morriss, LF Collins, *J. Chem. Phys.* **1964**, 414, 3357; c) RG Freeman, MB Hommer, KC Graber, MA Jackson, KA Allison, MJ Natan, *J. Phys. Chem.* **1996**, 100, 718
9. RP Feynman, *Engineering and Science*, **1959**,22
10. a) FP Zambrini, RM Crooks, *J. Am. Chem. Soc.* **1998**, 120, 9700; b) SL Brandow, WJ Dressick CS Dulcey, TS Koloski, LM Shirey, J. Schmidt, JM Calvert, *J. Vac. Sci. Tech. B.* **1997**, 15, 1818

11. AP Alivisatos, *Science*, **1996**, 271, 933
12. JK Gimzewski, C Joachim, RR Schlittler, V. Lanlais, H Tang, I Johannsen, *Science*, **1998**, 281, 531
13. R Resh, C Baur, A Bugacov, BE Koel, A Madhukar, AAG Requicha, P. Will, *Langmuir*, **1998**, 14, 23, 6613.
14. A Ullman, *Chem. Rev.* **1996**, 96, 1533
15. MJ Hostetler, RW Murray, Current Opinions in Colloid and Interface *Science*, **1997**, 2, 42; b) AC Templeton, WP Wuelfling, RW Murray, *Acc. Chem. Res.* **2000**, 33, 27
16. DA Handley in Colloidal Gold. Principles, Methods, and Applications, Vol I. MA Hayat, Ed. Academic Press, New York, 1989, 13-32; b) J. Turkavich, PC Stevenson, J. Hiller, *Discuss. Farad. Soc.* **1951**, 11, 55
17. a) KV Sarathy, PJ Thomas, GV Kulkarni, CNR Rao, *J. Phys. Chem. B* **1999**, 103, 399 b) CB Murray, CR Kagen, MG Bawendi, *Science*, **1996**, 270, 1335; c) JJ Shiang, JR Heath, CP Collier, RJSaykelly, *J. Phys. Chem. B* **1998**, 102, 3425
18. a) T. Cassegneau, JH Felder, *J Phys. Chem. B* **1999**, 103, 1789; b) PV Kamat, BJ Shanghavi, *J. Phys. Chem.B.* **1997**, 101, 7675
19. RG Freeman, KC Graber, KJ Allison, RM Bright, JA Davis, AP Guthrie, MB Hommer, MA Jackson, PC Smith, DG Walker, MJ Natan, *Science*, **1995**, 267, 1629; b) KV Sarathy, PJ Thomas, GU Kulkarni, CNR Rao, *J. Phys. Chem. B.* **1999**, 103, 399; c) DL Feldheim, TE Mallouk, *Chem. Commun.* **1996**, 2592; d) DL Feldheim, KC Graber, MJ Natan, TE Mallouk, *J. Am. Chem. Soc.* **1996**, 118, 7640; e) S. Peschel, G. Schmid, *Angew. Chem. Intl. Ed. Eng.* **1995**, 34, 1442
20. SM Marinakos, DA Shultz, DL Feldheim, *Adv. Mat.* **1999**, 11, 1 34; b) S. M. Marinakos, J. P. Novak, L. C. Brousseau, III, A. B. House, E. M. Edeki, J. C. Feldhaus, D. L. Feldheim. *J. Am. Chem. Soc.* **1999**, 121: (37) 8518-8522.
21. JJ Storhoff, R Elghanian, R Mucic, CA Mirkin, RL Letsinger, *J. Am. Chem. Soc.* **1998**, 286, 101
22. WL Shaiu, DD Larson, J Vensneka, E Henderson, *Nuc. Acids Res.* **1993**, 21, 99
23. RP Andres, T Bein, M Dorogi, S Feng, JI Henderson, CP Kubiak, W Mahoney, RG Osifchin, R Reifengerger, *Science*, **1996**, 272, 1323.

24. a) LN Lewis, **Chem. Rev.** 1993, 93, 2693; b) V. Kesevan, PS Sirvanand, S Chandrasekaran, Y Koltypin, A. Genanken. *Angew. Chem. Intl Ed.* **1999**, 38, 3521; c) Y Okahata, HJ Lim, GI Nakamuza S Hacklya, *J. Am. Chem. Soc.* **1988**, 110, 2495.
25. Sarathy, PJ Thomas, GU Kulkarni, CNR Rao, *J. Phys. Chem. B.* **1999**, 103, 399. *Chem. Soc.* 1996, 118, 8721
26. PV Kamat, BJ Shanghavi, *J. Phys. Chem. B.* **1997**, 101, 7675
27. BE Baker, NJ Kline, PJ Treado, MJ Natan, *J. Am. Chem. Soc.* **1996**, 118, 8721
28. SP Armes, M Aldissi, S. Agnew, S. Gottesfeld, *Langmuir*, **1990**, 6, 1745
29. JJ Shiang, JR Heath, CP Collier, RJSaykelly, *J. Phys. Chem. B* **1998**, 102, 3425
30. a) KV Sarathy, PJ Thomas, GV Kulkarni, CNR Rao, *J. Phys. Chem. B* **1999**, 103, 399 b) CB Murray, CR Kagen, MG Bawendi, *Science*, **1996**, 270, 1335
31. CA Mirkin, RL Letsinger, RC Mucic, JJ Storhoff, *Nature*, **1996**, 382, 607
32. a) X. Peng, TE Wilson, AP Alivisatons, PG Schultz, *Angew. Chem. Intl, Ed. Engl.* **1997**, 36, 145; b) LC Brousseau, JP Novak, SM Marinakos, DL Feldheim, *Adv. Mat.* **1999**, 11, 447; c) JP Novak, DL Feldheim, *J. Am. Chem. Soc.*, **2000**, 122, 3979; d) W.P. McConnell, J.P. Novak, L.C. Brousseau, III, R.R. Fuierer, R.C. Tenent, D.L. Feldheim, *J. Phys. Chem. B.* **2000**, 104: (38) 8925-8930
33. DL Feldheim, CD Keating, *Chem. Soc. Rev.* **1998**, 27, 1
34. RG Freeman, KC Graber, KJ Allison, RM Bright, JA Davis, AP Guthrie, MB Hommer, MA Jackson, PC Smith, DG Walter, MJ Natan, *Science*, **1995**, 267, 1629;
35. a) M.L. Sandrock, CA Foss, Jr. *J. Phys. Chem. B* **1999**, 103, 11398 and references therein; b) M Quinten, U Kreibig, *Surface Science* **1986**, 172, 557; c) U. Kreibig, A. Hilger, H. Hovel, M. Quinten, "Optical Properties of Free and Embedded Metal Clusters: Recent Results" in *Large Clusters of Atoms and Molecules*, TP Martin(Ed.) Kluwer, Netherlands, **1996**, 475-493; d) EJ Zeman, GC Schatz, *J. Phys. Chem.* **1987**, 91, 634; e) WH Yang, GC Schatz, RP Van Duyne, *J. Chem Phys.* **1995**, 103(5) 869; f) WT Doyle, *Phys. Rev. B.* **1989**, 39(14)9852; g) BT Draine, J. Goodman, *The Astrophysical Journal*, **1993**, 405, 685; h) EM Purcell, CR Pennypacker, *The Astrophysical Journal*, **1973**, 186, 705

36. FW Vance, BI Lemon, JA Eckoff, JT Hupp, *J. Phys. Chem. B*, **1998**, 102 (11), 1845
37. FW Vance, BI Lemon, JT Hupp, *J. Phys. Chem. B*, **1998**, 102 (50), 10091
38. JP Novak, LC Brousseau, FW Vance, RC Johnson, BI Lemon, JT Hupp, DL Feldheim, *J. Am. Chem. Soc.* **2000**, 122, 12029-12030
39. ML Sandrock, CD Pibel, FM Geiger, CA Foss, Jr. *J. Phys. Chem. B*, **1998**, 103 (14), 2668
40. JA Creighton, in *Surface Enhanced Raman Scattering*, edited by RK Chang, TE Furtak, Plenum, New York, **1982**; b) H Abe, K Manzel, W Schulze, *J. Chem. Phys.* 1981, 74, 792; c) K Manzel, W Schulze, M Moskovits, *Chem. Phys. Lett.* **1982**, 85, 183
41. a) S Nie, SR Emory, *Science*, **1997**, 275, 1102; b) SR Emory, S Nie, *J. Phys. Chem. B* **1998**, 102, 493; c) SR Emory, WE Haskins, S Nie, *J. Am. Chem. Soc.* **1998**, 120, 8009
42. RP Andres, T Bein, M Dorogi, S Feng, JI Henderson, CP Kubiak, W Mahoney, RG Osifchin, R Reifenberger, *Science*, **1996**, 272, 1323
43. LC Brousseau, III, Q Zhao, DASchultz, DL Feldheim, *J. Am. Chem. Soc.* **1998** 120 (30), 7645
44. DL Klein, PL McEuen, JE bowen Katari, R Roth, AP Alivisatos, *Appl. Phys. Lett.* **1996**, 68 2574
45. a) AC Templeton, WP Wuefling, RW Murray, *Acc. Chem. Res.* **2000**, 33, 27
b) S Chen, RS Ingram, MJ Hostetler, JJ Pietron, RW Murray, TG Schaff, TG Khoury, MM Alvarez, RL Whetten, *Science*, **1998**, 280, 2098 c) JF Hicks, AC Templeton, S Chen, KM Sheron, R Jasti, RW Murray, J Deburd, TG Schaff, RL Whetten, *Anal. Chem.* **1999**, 71, 3703 d) JJ Pietron, JF Hicks, RW Murray, *J. Am. Chem. Soc.* **1999**, 121, 3303
46. S. Chen, *J. Phys. Chem. B.* **2000**, 104 (4) 663

Scope

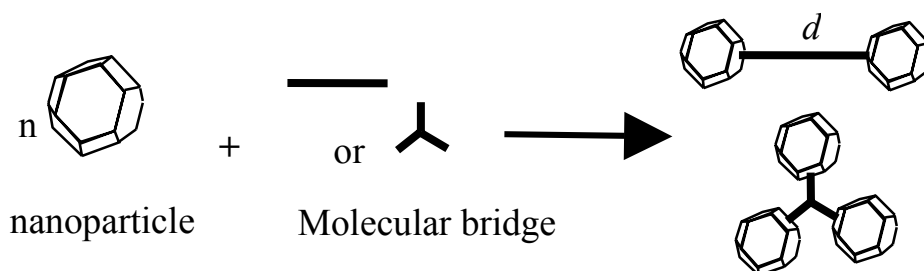
As the introduction describes nanotechnology and its applications to nanoparticles I will now show how chemistry can be used to assemble nanoparticles into highly ordered arrays. Chapter 2 begins this journey by describing the synthesis of the phenyl-acetylene based bridge molecules. Chapter 3 will outline the method for combining the organic bridge with our nanoparticles of choice. Also described is the control over array symmetry and interparticle distance. The following chapters will outline the optical properties of these organically bridged nanoparticle systems. These optical properties show how electromagnetic coupling is a function of distance and symmetry between nanoparticles. Chapter 4 will focus on the linear optical properties. Experimental spectra are described using theoretical calculations. Chapter 5 describes the NLO measurements, which aid in identification of array symmetry in solution. Chapter 6 shows how SERS can be used to show the existence of a single linker between the particles. As we begin Chapter 7, we leave the discussion of optical properties and discuss the electronic coupling between nanoparticles. To round out the synthesis, Chapter 8 outlines some new methods for separation of these nanostructures. Let the journey begin.

Chapter 2
Synthesis of Phenyl-Acetylene Bridges for
Nanoparticle Templates

Introduction

It has been suggested that nanoparticles, based on their electronic and optical properties, could be used as a platform to build new electronic devices¹. Before we can address the device-like properties of nanoparticles we must first be able to study fundamental interparticle interactions of discrete numbers of particles. One of the major obstacles of studying nanoscale materials are methods of assembly. It is difficult to assemble large numbers of arrays containing nanoparticles with known aggregation number and controlled geometry. This chapter describes the synthesis of organic linker molecules to be used as templates for organized nanoparticle arrays.

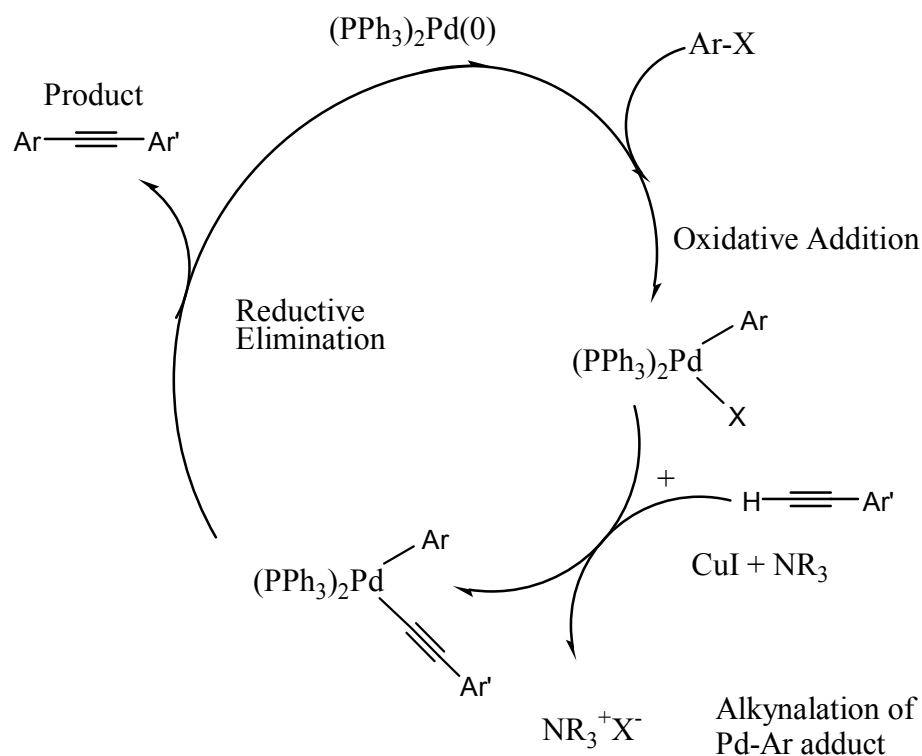
Our strategy towards the assembly of nanoparticle arrays is to design a molecular bridge with terminal end groups that can hold nanoparticles into discrete arrays. This is depicted in **Scheme 2.1**. This method would work by



Scheme 2.1. Proposed linking procedure

spontaneously organizing nanoparticle arrays with symmetry and number of particles controlled by the linking molecule².

We have chosen phenyl-acetylene-based bridges for several reasons. First, these molecules are rigid and can be designed with varying lengths and shapes. Second, there are previously published synthetic schemes for building similar type molecules³. These methods can easily be adapted to form linking molecules with a variety of shapes and sizes. Lastly, these molecules can be synthesized with a wide range of terminal end groups⁴ that can bind covalently with the nanoparticle of choice. Specifically, we have designed and synthesized phenyl-acetylene molecules with $D_{\infty h}$, D_{3h} , D_{4h} , and T_d symmetry with thiol end groups to template gold and silver nanoparticle arrays².



Scheme 2.2. Mechanism for Pd(0)/Cu catalyzed Heck Coupling.

The basic mechanism for this synthesis has previously been described as a Heck coupling⁵. The method involves a Pd(0)/Cu catalyzed coupling of an aryl iodide with terminal acetylene. The mechanism is shown in **Scheme 2.2**. It has been described in the following manner. The Pd(PPh₃)₂ adduct is generated in situ from Pd₂(dba)₃ and PPh₃. This complex then couples to the aryl iodide through oxidative addition, Step 1. Under basic conditions the terminal proton on the acetylene then combines with the Cu. This Cu complex then combines with the Pd(PPh₃)₂-Ar-I complex by alkynylation. The Pd(PPh₃)₂ adduct then leaves via reductive elimination. This step regenerates the Pd catalyst and leaves the coupled phenyl acetylene as a product. Yields have been reported greater than 95% and vary greatly depending on the substituents on the aryl ring³.

The above-described mechanism allows for many types of molecular architectures to be made. Our molecular linkers were synthesized in the following manner. A step-wise growth of linear chains was done first. This leaves a library of various length molecules to build from. These chains were then combined with a core molecule of desired symmetry and then terminated with a desired end group to provide the linker of choice. Linear chains, with D_{∞h} symmetry, were produced using 1,4-substituted benzene or trans-*meso* substituted porphyrin cores. Trigonal Planer, with D_{3h} symmetry, was achieved with 1,3,5, - substituted benzene cores. Square planer, D_{4h} symmetry was accomplished using 5,10,15,20-meso-substitued porphyrin cores. Tetrahedral cores were generated using a tetra-phenyl methane core.

The step-wise growth of the chains was made possible by careful choice of protecting groups³. It is desirable to have selective deprotection on each side. This was achieved through silane and triazene chemistry⁶. The first step in synthesis was to create Compound 1, 1-diethyl triazene, 4-trimethylsilyl ethynal-benzene. This was synthesized in 10-gram quantities with a 95+% yield. This molecule is important due to the selectively deprotecting triazene and TMS groups on each end. Variations of this monomer can be made by the addition of solubilizing alkyl groups in the 2,6-positions of the phenyl ring. The batch is divided into two halves with each undergoing a selective deprotection for the triazene or TMS, to generate an aryl iodide or terminal acetylene, respectively. The two molecules are then recombined using the Heck coupling. This deprotection and recombination can be repeated several times in order to facilitate controlled chain growth.

Core molecules were chosen based on symmetry. These core molecules have substituted multiple halogen substituents in which to couple arms to. 1,4 - Di-iodo benzene was used for linear chains, as shown in Scheme 2.3. 1,3,5 – tribromo benzene was used for trigonal planer linkers(Scheme 2.4). Tetrahedral was synthesized by iodination of tetraphenyl methane using I₂ and sodium periodate⁷ (Scheme 2.5). In addition to these phenyl based core molecules, Porphyrin templated structures were also made (Scheme 2.6).

Porphyrins were chosen do to their rigid structure and potential for optical activity. Porphyrins were synthesized using the Lindsey Method⁸, in which aldol condensation of an aldehyde and pyrrole yields a desired structure. 5,15 *meso*-

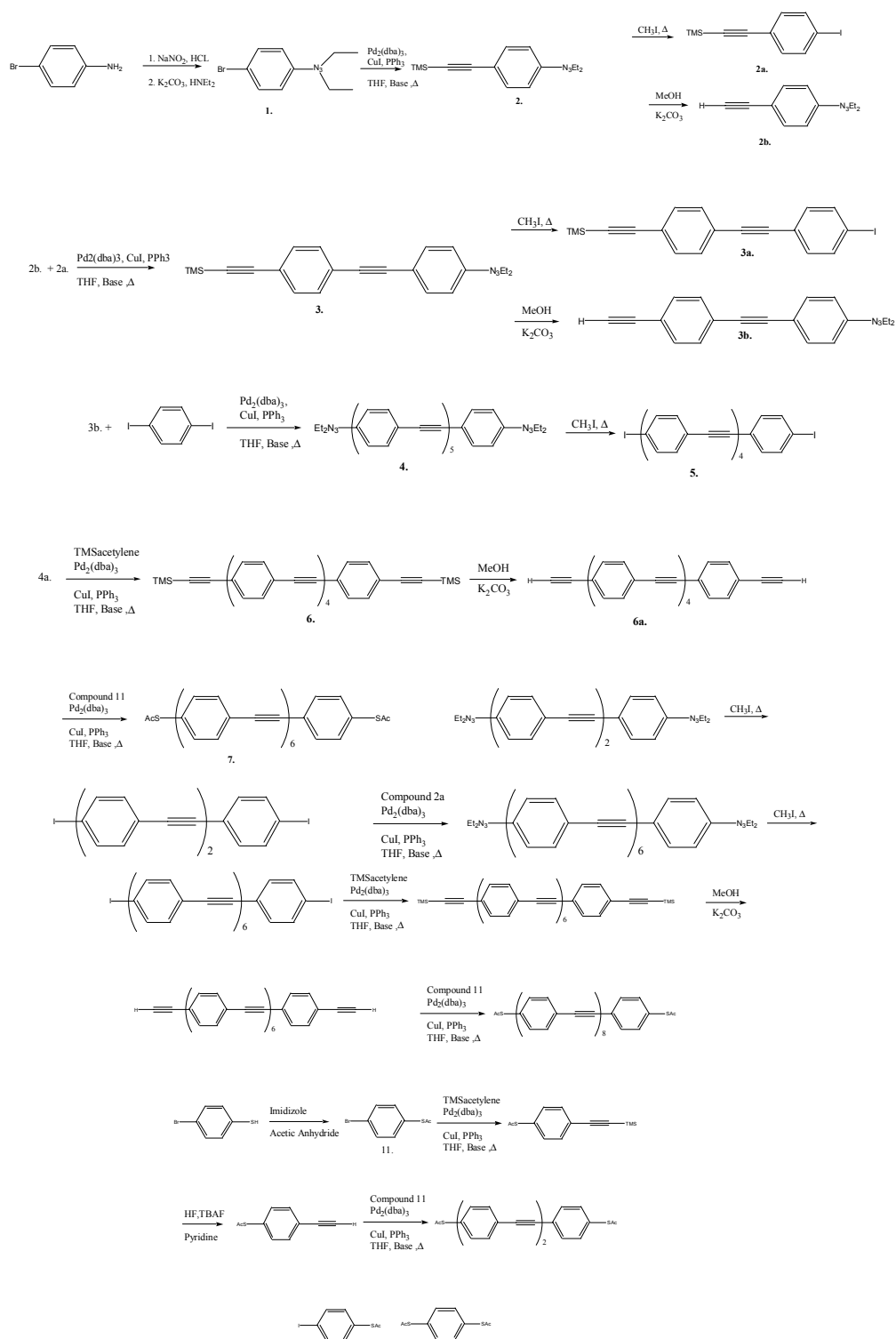
substituted porphyrins were generated as a linear linker using 4-substituted benzaldehyde and *meso*-mesityl-dipyrromethane. Tetra-*meso*-alkynal porphyrins⁹ were generated using a 4-thiobenzyl-phenyl propynal¹⁰ and pyrrole.

When designing the linker structures, we must pay attention to the packing dimensions of the nanoparticles. The length of the arms will be dependent on the diameter of nanoparticle to be linked. This is not important if we are templating two particles. However, More than two requires consideration to packing density and void space. Using geometry, a simple relationship can be derived to make sure the arm lengths are correct. The arm length can be determined using the following equations:

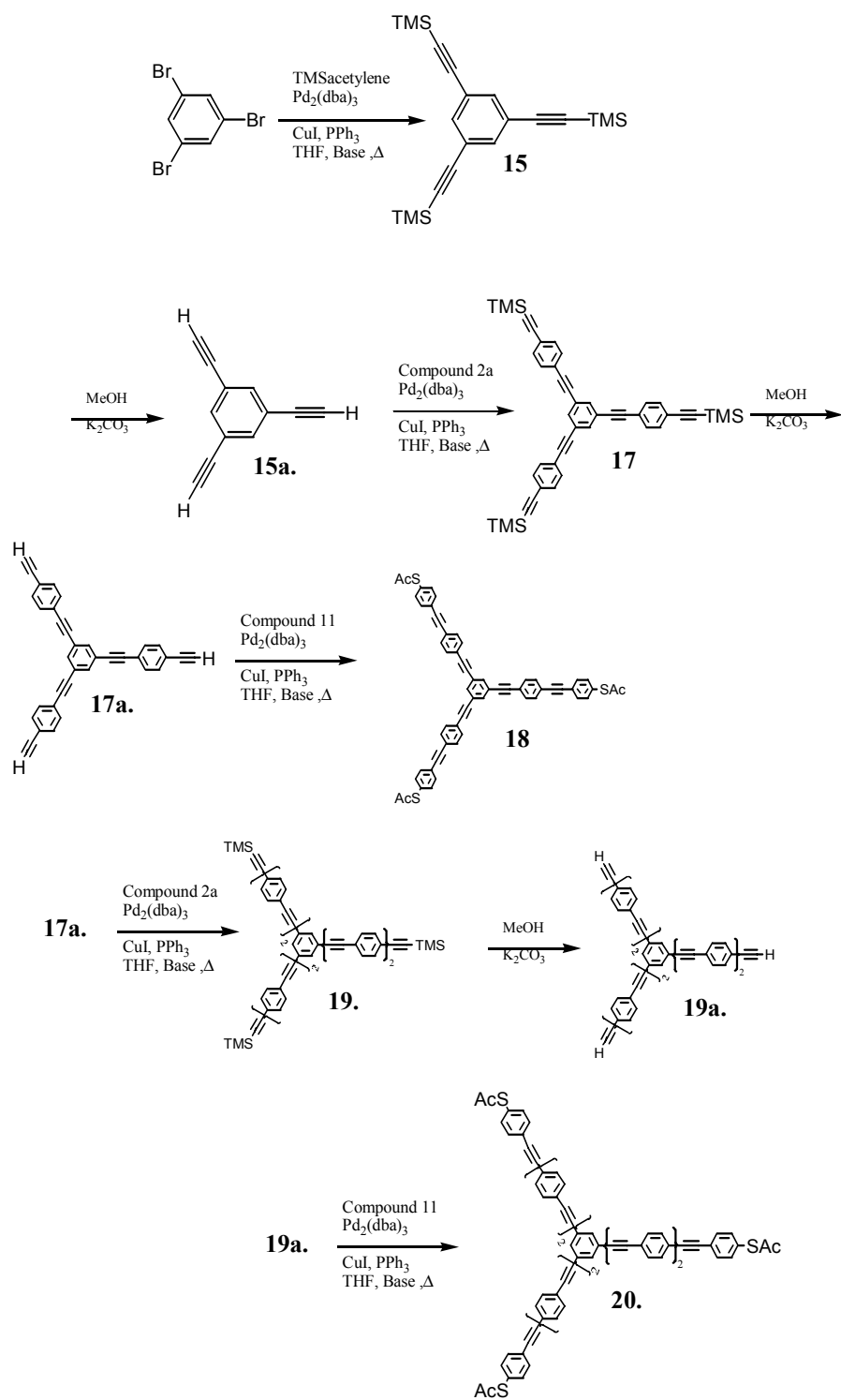
$$\text{For trimers: } X = R/\text{Cos } 30^\circ - R \quad (2.1)$$

$$\text{For tetrahedron: } X = R/\text{Cos } 35^\circ - R \quad (2.2)$$

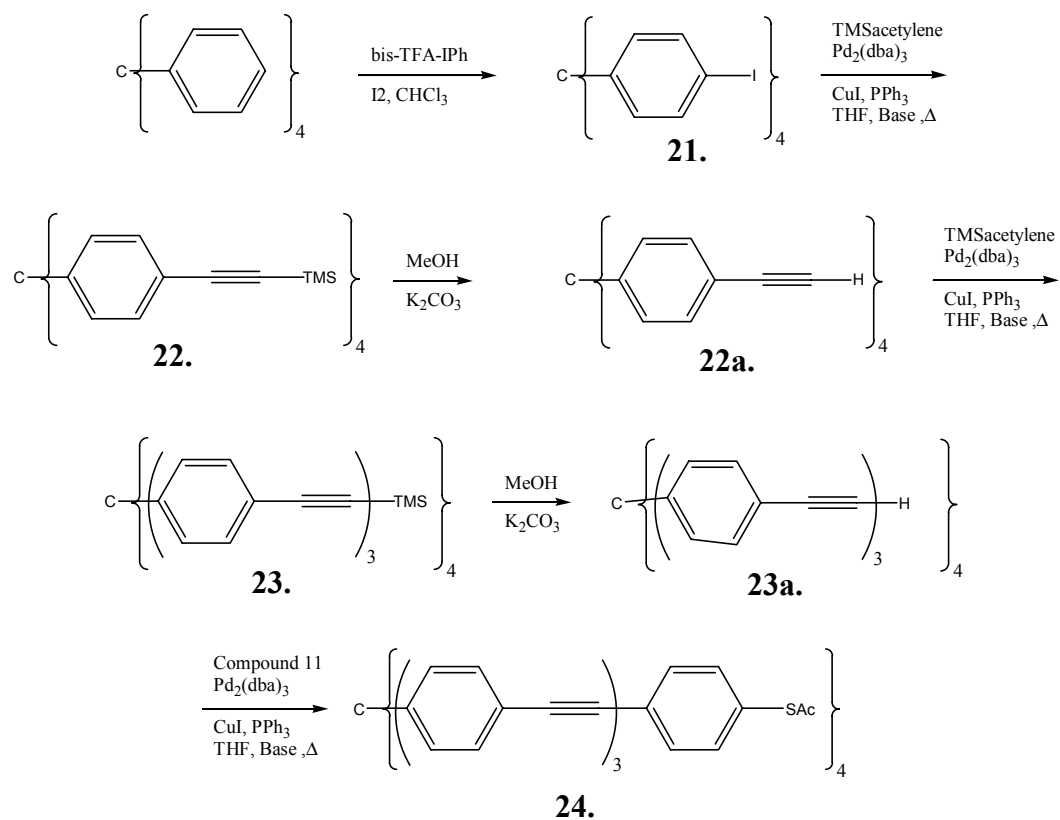
In each equation, X is the length of the arm in nm and R is the radius of the nanoparticle in nm. Using an average length of 0.8nm per phenyl acetylene unit we can estimate how many PA units are required to fit the minimum interparticle spacing.



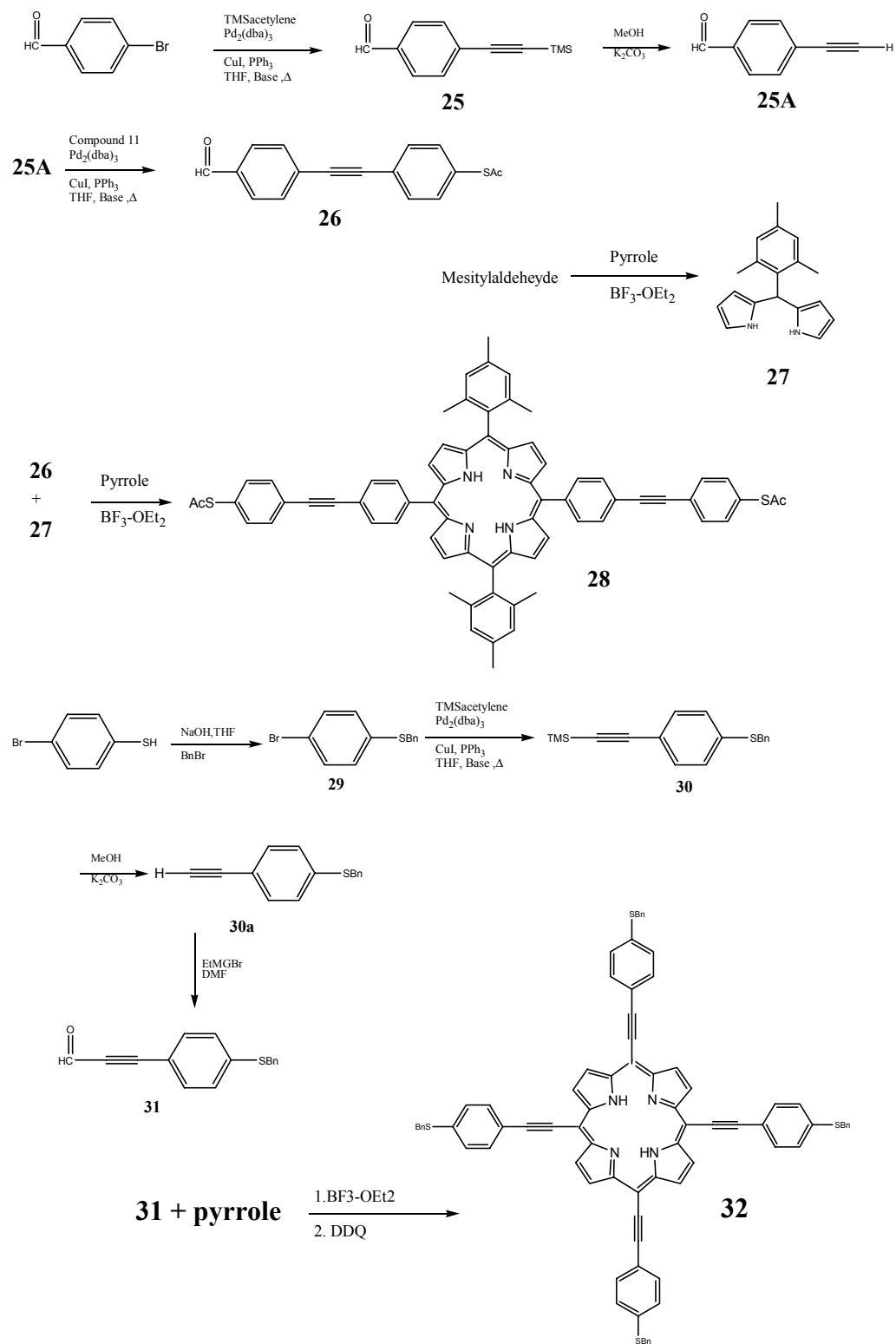
Scheme 2.3. Synthetic route to linear molecular bridges.



Scheme 2.4. Synthetic route to trigonal planer molecular bridges.



Scheme 2.5. Synthetic route to tetrahedral molecular bridges.



Scheme 2.6. Synthetic route to Porphyrin based molecular bridges.

General Reaction Procedures

All reagents were obtained from Fisher Scientific or Sigma-Aldrich. All chemicals were used as received unless otherwise noted. Solvents were distilled under inert gas. THF, benzene, and toluene were distilled over sodium/benzophenone. Triethyl amine and Hunig's base (N,N-diisopropyl ethyl amine) were distilled over P₂O₅. An 18M Ω , Millipore system was used for Reactions requiring water. All reaction glassware was dried in an oven at 120° C prior to use. Silica gel (40 μ m, Fischer Brand) was obtained from Fisher Scientific. Solvents were removed on a Büchi roto-evaporator using a water aspirator and controlled temperature bath. NMR data were acquired on a GE-Varian 200 or 300Mhz.

Deprotection steps are as follows. The silylated alkyne was dissolved in methanol and/or dichloromethane. A catalytic amount of potassium carbonate was added and the reaction stirred overnight at room temperature. Upon completion the mixture was roto-vapped to dryness and dissolved in dichloromethane. The crude product was then filtered through a 2cm thick silica plug on a coarse frit to yield the free alkyne, which was used without further purification. Slight modifications are described for each material.

Di-ethyl triazenes were converted to aryl iodide using iodo-methane. The triazene was charged into a heavy walled screw-top flask. The flask was evacuated and back filled with argon. Freshly distilled methyl iodide was transferred into the flask using a cannula or syringe under argon. The flask was then degassed using a

freeze-pump-thaw method (3x) and brought to less approximately one torr pressure as indicated by vacuum gauge. The flask was then sealed and reacted overnight at 120° C. (Note: this reaction proceeds under high temperature and pressure. Appropriate precautions should be taken.) Upon completion the reaction was cooled and excess methyl iodide was removed by vacuum transfer. The residue was then dissolved in ether and filtered through a 2cm plug of silica on a coarse frit. The plug was washed with ether until product was completely eluted. The solvent was then removed and resulting product was used without further purification. Slight differences are described for each material.

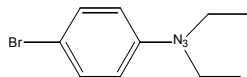
The general procedure for coupling the aryl iodide and terminal acetylene proton is as follows. All reactions were carried out under air/moisture free conditions using standard schlenk line techniques. All solvents were dried under inert conditions using standard methods. The solid catalysts, tirs(dibenzylideneacetone)dipalladium(0), Pd₂(dba)₃, (2 mol %), Triphenyl Phosphine, PPh₃, (20 mol %, 5 equivalents based on Pd(0)), and Copper Iodide, CuI, (10 mol %) were charged along with solid reactants into a schlenk flask of appropriate size. The flask was evacuated and backfilled with argon gas. Solvents, anhydrous THF (2ml/mmol) and base (0.7ml/mmol), were added by syringe. The flask was then sealed and reacted overnight at approximately 70° C. Upon completion, the reaction was subject to aqueous work up, extracting with ether or other suitable solvent (3x). The combined organic layers were dried, magnesium

sulfate, and concentrated before separation by column chromatography (silica gel).

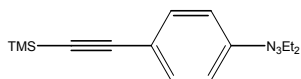
Slight modifications are described for each material.

In Conclusion, rigid organic linkers were synthesized to template metal nanoparticles. Linkers were made with varying geometries. Different chain lengths were available for the linear chains and trigonal planer structures. These linkers were synthesized with thiol terminated end groups to facilitate binding to Au and Ag nanoparticles. The use of these linkers is described in Chapter 3 of this dissertation.

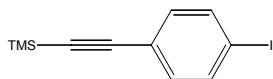
Synthesis



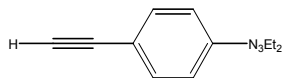
Compound 1. 4-N,N-diethyltriazeno-bromobenzene In a 500ml erlenmeyer flask, 20.5 g(120 mmols) 4-Bromoaniline was dissolved in 200ml of 1.3M HCl and cooled to 0°C in an ice water bath. In a separate 50ml erlenmeyer flask, 12.3g NaNO₂ was dissolved in 40ml H₂O and cooled to 0°C. While stirring, the NaNO₂ solution was added dropwise to the 4-bromoaniline over a period of one hour then stirred for an additional 1 hour at 0°C. Upon completion, the solution was added dropwise to 25 g K₂CO₃, 19ml HNEt₂, and 150ml water-cooled to 0°C in a 1L Erlenmeyer flask. The temperature of this reaction must not exceed 4°C. The reaction was stirred for one to three hours until a brown oil appears at the bottom of the flask. The oil was recovered by extraction with Et₂O (3x, 150ml). The organic layers were combined and dried with MgSO₄. The solvent was removed by rotary evaporation to yield a brown oil. The solid precipitate composed of unreacted starting material was removed by passing the reaction mixture through a plug of SiO₂ with Et₂O to yield 23.56g (75.6%) of the desired product. ¹H-NMR. 7.358(4H, dd, J1=27.2 Hz, J2=6.48 Hz, Ar-H); 3.752(4H, q, Et-CH₂); 1.26(6H, t, Et-CH₃)



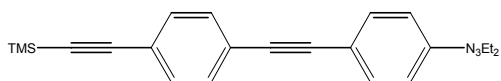
Compound 2¹⁴. 4-N,Ndiethyltriazeno,-trimethylsilyl-ethynalbenzene A 250ml Schlenk flask was charged with 20.162 g(78.7 mmols) of Compound 1. 1.457 g Pd₂(dba)₃, 1.56 g CuI, and 4.13 g PPh₃, then evacuated and backfilled with inert gas. 156 ml of anhydrous THF and 55 ml of anhydrous Hunig's base were added by syringe. The mixture was stirred to ensure mixing and then 13.5 ml of Trimethylsilylacetylene was added by syringe. The mixture was then degassed by Freeze, pump, thaw, backfilled with argon and stirred for 3 days at 80°C. Upon completion the mixture was rotovaped to remove solvent and then redissolved in 200ml Petroleum Ether(Pet Ether). The resulting mixture was sonicated for 20min and then filtered through a 1 cm silica plug under 1cm of Celite. The eluents were rotovapped to produce 21.2g (98%) of a yellow brown oil as desired product. ¹H-NMR. 7.383(4H, dd, J₁=18 Hz, J₂ = 8.38, Ar-H); 3.765 (4H, q, Et-CH₂); 1.26 (6H, t, Et-CH₃); 0.246(9H, s, TMS-CH₃)



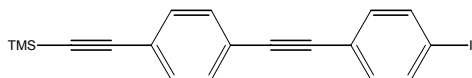
Compound 2A. 4-iodo-trimethylsilylethynyl benzene 10g of molecule 2 was charged in a 100ml heavy-wall, screw top flask. The flask was evacuated backfilled with inert gas. 40ml of freshly distilled methyl iodide was added by cannulation. The flask was degassed and heated to 120°C overnight. The reaction was cooled and excess methyl iodide was recovered by vacuum transfer. The remaining solid was dissolved in Pet Ether and filtered through a silica plug to yield (82%) of a pale yellow solid. ¹H-NMR: 7.407(4H, dd, J₁=91.6 Hz, J₂ = 8.1 Hz, Ar-H), 0.244(9H, s, TMS-CH₃)



Compound 2B. 4-N,N-diethyl triazene, ethynylbenzene 10 g of Molecule 2 (36.6 mmol) was dissolved in 50ml of MeOH. A catalytic amount of K₂CO₃ was added and the mixture stirred at room temp overnight. Upon completion, The solvent was removed by rotary evaporation. The resulting brown oil was filtered on 1cm of silica using CH₂Cl₂ as an eluent. The solvent was removed to yield 7.28g (99%) of the desired product as a yellow/brown oil. ¹H-NMR: 7.383(4H, dd, J₁=18 Hz, J₂ = 8.38, Ar-H); 3.765 (4H, q, Et-CH₂); 3.17(1H, s, CC-H); 1.26 (6H, t, Et-CH₃)

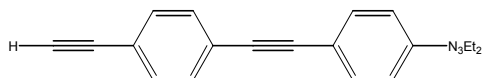


Compound 3. 15.7g (52mmol) 2A, 11.38g 3B, 1.0648 g Pd₂(dba)₃, 1.0776 g CuI, and 2.968g PPh₃ were placed in a schlenk flask, evacuated and backfilled with Argon. 60ml THF and 11ml TEA were added by syringe. The mixture was sealed and stirred for 48 hours at 80°C. The reaction was then cooled and the solvent removed. The residue was filtered through Celite. The solvent was removed and the residue was separated using column chromatography (SiO₂, 5:1 Pet Ether/Et₂O, R_f=0.25) to yield 12.2 g (62%) of a yellow solid. ¹H-NMR: 7.454(dd, 4H, J¹=17.54, J²=8.34, Ar-H), 7.4698(s, 4H, Ar-H), 3.787(q, 4H, Et-CH₂), 1.2912(t, 6H, Et-CH₃), 0.2710(s, 9H, TMS) ¹³C-NMR: 151.36, 132.46, 131.990, 122.66, 122.34, 119.21, 104.93, 96.17, 92.28, 88.96, 0.08

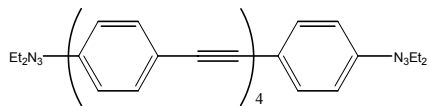


Compound 3A 700mg of molecule 2 was charged in a 50ml heavy-wall, screw top flask. The flask was evacuated back-filled with inert gas. 5ml of freshly distilled methyl iodide was added by cannula. The flask was degassed and heated to 120°C overnight. The reaction was cooled and excess methyl iodide was recovered by

vacuum transfer. The remaining solid was dissolved in Diethyl Ether and filtered through a silica plug to yield 621.5mg (84%) of a pale yellow solid. $^1\text{H-NMR}$: 7.4393(4H, dd, $J_1=86.8$ Hz, $J_2 = 8.2$ Hz, Ar-H), 7.4162(s, 4H, AR-H). 0.231(9H, s, TMS- CH_3)

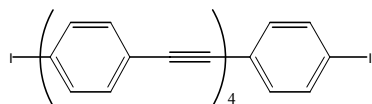


Compound 3B 500mg of Compound 3 was dissolved in 5ml of a 1:1 mixture of Methanol/methylene chloride. A catalytic amount of K_2CO_3 was added and the mixture stirred at room temperature for 4 hours. Upon completion, The solvent was removed by rotary evaporation. The resulting brown oil was filtered on 1cm of silica using CH_2Cl_2 as an eluent. The solvent was removed to yield 0.383 g(95%) of the desired product. $^1\text{H-NMR}$: 7.462(m, 8H, Ar-H); 3.782 (4H, q, Et- CH_2); 3.159(1H, s, CC-H); 1.279 (6H, t, Et- CH_3)

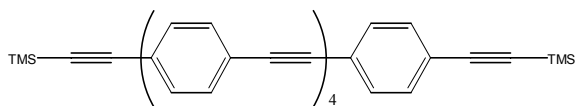


Compound 4 101mg of **Compound 3B**, 53.4mg 1,4-diiodobenzene, 11.6 mg $\text{Pd}_2(\text{dba})_3$, 12 mg CuI , and 15.1 mg PPh_3 were placed in a schlenk flask, evacuated and backfilled with Argon. 10 ml TEA was added by syringe. The mixture was

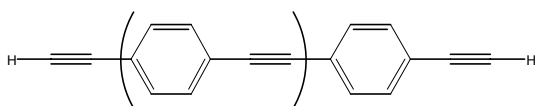
sealed and stirred for 48 hours at 80°C. The reaction was then cooled and the solvent removed. The residue was dissolved in Et₂O filtered through Celite. The solvent was removed and the residue was separated using column chromatography (SiO₂, 5:1 hexanes/Et₂O, R_f=0.20) to yield a yellow solid which was carried on to make **5**. ¹H-NMR: 7.454(dd, 4H, J₁=17.54 Hz, J₂=8.34 Hz, Ar-H), 7.501(m, 20H, Ar-H), 3.742(q, 4H, Et-CH₂), 1.265(t, 6H, Et-CH₃).



Compound 5 The amount of **4** collected above was added to a 25ml heavy-wall, screw top flask. The flask was evacuated back-filled with inert gas. 10ml of freshly distilled methyl iodide was added by syringe. The flask was degassed and heated to 120°C overnight. The reaction was cooled and excess methyl iodide was recovered by vacuum transfer. The remaining solid was dissolved in Diethyl Ether and filtered through a silica plug to yield 25.2mg (23% over two steps) of a pale yellow solid. ¹H-NMR: 7.4705(8H, dd, J₁=89.2 Hz, J₂ = 6.6 Hz, Ar-H), 7.4354(dd, 12H, J₁=23.3 Hz, J₂=7.8 Hz, AR-H).

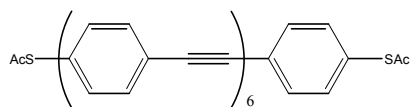


Compound 6 26.2 mg (0.035 mmol) of **5**, 1.9mg Pd₂(dba)₃, 1.5mg CuI, and 2.0 mg PPh₃ were charged into a 50ml Schlenk flask, evacuated and backfilled with inert gas 15 ml of NEt₃ was added by syringe. The mixture was stirred to ensure mixing and then 15 μl of Trimethylsilylacetylene was added by syringe. The mixture was then degassed by Freezepump thaw, backfilled with argon and stirred for 32 hours at 80°C. Upon completion the mixture was rotovaped to remove solvent and then redissolved in Et₂O. The resulting mixture was separated using column chromatography on SiO₂ (1:1 Hexanes/DCM) to yield a yellow solid. The products were carried on to the next step. ¹H-NMR. 7.4453(20H, m, Ar-H); 0.2592(s, 18H, TMS-CH₃)

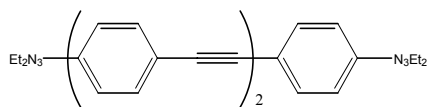


Compound 6A The collected product **6** was dissolved in 10ml of 1:1 MeOH/DCM and a catalytic amount of K₂CO₃ was added. The mixture was stirred overnight at room temp. Upon completion, The solvent was removed by rotary evaporation. The

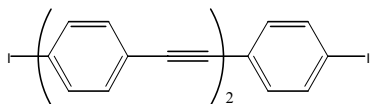
resulting residue was filtered on 1cm of silica using CH_2Cl_2 as an eluent. The solvent was removed to yield 12.2mg(66% over two steps) of the desired product. $^1\text{H-NMR}$: 7.4830(m, 20H, Ar-H); 3.1944(2H, s, CC-H).



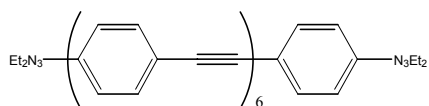
Compound 7 10mg of **6A**, 13.1mg of 4-bromo, thioacetylbenzene, 1 mg $\text{Pd}_2(\text{dba})_3$, 0.6 mg CuI , and 1 mg PPh_3 were placed in a schlenk flask, evacuated and backfilled with Argon. 10 ml TEA was added by syringe. The mixture was sealed and stirred for 48 hours at 80°C . The reaction was then cooled and solvent removed. The residue was filtered through Celite using Et_2O . The solvent was removed and the residue was separated using Column Chromatography on SiO_2 (1:1 hexanes/DCM, $R_f=0.28$) to yield 7.3mg (48%) of a pale yellow solid. $^1\text{H-NMR}$: 7.454(dd, 4H, $J_1=17.54$ Hz, $J_2=8.34$ Hz, Ar-H), 7.501(m, 20H, Ar-H), 2.367(s, 6H, Ac- CH_3)



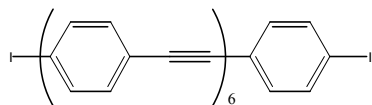
Compound 8 2.78g of 2A, 2.00 1,4-diiodobenzene, 226 mg Pd₂(dba)₃, 22.8 mg CuI, and 207.7 mg PPh₃ were placed in a schlenk flask, evacuated and backfilled with Argon. 10 ml TEA and 30ml THF were added by syringe. The mixture was sealed and stirred for 20 hours at 85°C. The reaction was then cooled and the solvent removed. The residue was filtered through Celite. The solvent was removed and the residue was separated using Column Chromatography on SiO₂(1:1 hexanes/DCM, R_f=0.56) to yield 1.088g (35%) of a yellow solid. ¹H-NMR: 7.475(m, 12H,Ar-H), 3.79(q, 8H, Et-CH₂), 1.2906(t, 12H, Et-CH₃)



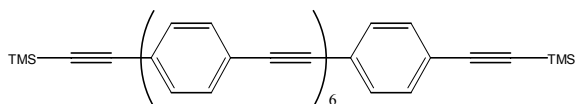
Compound 8A- 1.088 g (2.3mmol) of **8** was added to a 50ml heavy-wall, screw top flask. The flask was evacuated back-filled with inert gas. 20ml of freshly distilled methyl iodide was added by syringe. The flask was degassed and heated to 120°C overnight. The reaction was cooled and excess methyl iodide was recovered by vacuum transfer. The remaining solid was dissolved in Pet Ether and filtered through a silica plug to yield 0.945g (78%) of a pale yellow solid. ¹H-NMR: 7.4876(dd, 8H, J₁=89 Hz, J₂=3.6 Hz, Ar-H), 7.4166(s, 4H, Ar-H).



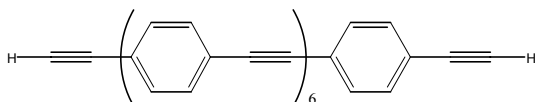
Compound 9 344 mg of **3A**, 298 mg **8A**, 25 mg Pd₂(dba)₃, 8 mg CuI, and 18.6 mg PPh₃ were placed in a schlenk flask, evacuated and backfilled with Argon. 10 ml Hunig's Base and 25 ml THF were added by syringe. The mixture was sealed and stirred for 30 hours at 98°C. The reaction was then cooled and the solvent removed. The residue was filtered through Celite. The solvent was removed and the residue was separated using Column Chromatography on SiO₂ (25:1 hexanes/Et₂O until clear, Final product eluted with DCM) to yield 215 mg (45%) of a bright yellow solid which was carried on to make **5**. ¹H-NMR: 7.51(m, 28H, Ar-H), 3.79(q, 8H, Et-CH₂), 1.2865(t, 12H, Et-CH₃).



Compound 9A- 215 mg (0.25mmol) of **9** was added to a 50ml heavy-wall, screw top flask. The flask was evacuated back-filled with inert gas. 20ml of freshly distilled methyl iodide was added by syringe. The flask was degassed and heated to 120°C overnight. The reaction was cooled and excess methyl iodide was recovered by vacuum transfer. The remaining solid was dissolved in Diethyl Ether and filtered through a silica plug to yield 182 mg (79.8%) of an orange solid. ¹H-NMR: 7.476(dd, 8H, J₁=20 Hz, J₂=5.2 Hz, Ar-H), 7.4962(s, 6H, Ar-H).

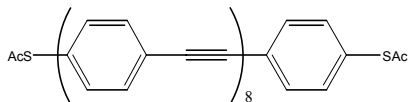


Compound 9B 115 mg (0.035 mmol) of **9A**, 5mg Pd₂(dba)₃, 2 mg CuI, and 5 mg PPh₃ were charged into a 50ml Schlenk flask, evacuated and backfilled with inert gas 20 ml of NEt₃ was added by syringe. The mixture was stirred to ensure mixing and then 50 μl of Trimethylsilylacetylene was added by syringe. The mixture was then degassed by Freeze, pump thaw, backfilled with argon and stirred for 32 hours at 80°C. Upon completion the solvent was removed and then redissolved in Et₂O. The resulting mixture was then extracted 2x with H₂O. The organic phase was dried with MgSO₄. The solvent was removed and redissolved in Hexanes. The mixture was cooled to -10°C in the freezer. The resulting Orange precipitate was collected on a fine frit by vacuum filtration. This product was carried on to the next step. ¹H-NMR. 7.46(28H, m, Ar-H); 0.268(s, 18H, TMS-CH₃)

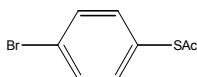


Compound 9C The collected product **9A** was dissolved in 40ml of 1:1 MeOH/DCM and a catalytic amount of K₂CO₃ was added. The mixture was stirred overnight at room temp. Upon completion, The solvent was removed by rotary evaporation. The resulting residue was filtered on 1cm of silica using CH₂Cl₂ as an

eluent. The solvent was removed to yield 37.6 mg(42% over two steps) of the desired product. $^1\text{H-NMR}$: 7.4849(m, 20H, Ar-H); 3.178(2H, s, CC-H).

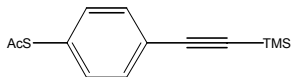


Compound 10 37.6 mg of 9C, 26.9mg of 4-bromo-thioacetyl benzene, 8.8 mg $\text{Pd}_2(\text{dba})_3$, 3.2 mg CuI , and 5.2 mg PPh_3 were placed in a schlenk flask, evacuated and backfilled with Argon. 30 ml TEA was added by syringe. The mixture was sealed and stirred for 3 days at 85°C . The reaction was then cooled and the solvent removed. The residue was redissolved in toluene and filtered through 1cm Celite. The organic phase was then washed with H_2O (2X), dried with MgSO_4 , and rotovapped to dryness. The mixture was taken up in 0.5ml DCM and diluted with EtOH. 21.2mg (40%) of orange crystals were collected by vacuum filtration on a fine frit. $^1\text{H-NMR}$: 7.508(m, 32H, Ar-H), 2.367(s, 6H, Ac- CH_3), $\lambda_{\text{max}} = 344$ nm.



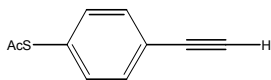
Compound 11 4-bromo, thioacetylbenzene (11) 10g 4-bromothiophenol, 5.5 ml acetic anhydride, 4.72 g Imidazole were dissolved in 150 ml DCM and stirred for 2 days at room temperature. The solvent was then removed by rotary evaporation. The resulting yellow oil was then washed with 30ml Pet Ether/ H_2O (3X). The resulting organic layers were recombined, dried with MgSO_4 , and the solvent removed. The residue was then separated using column chromatography (hexanes, $R_f=0.41$) to yield a white solid. $^1\text{H-NMR}$: 7.394(dd, 4H, $J_1= 54.8$ Hz, $J_2= 8.42$ Hz,

Ar-H), 2.4135(s, 3H, Ac-CH₃): ¹³C-NMR: 192.97, 135.93, 132.34, 127.03, 124.02, 30.18



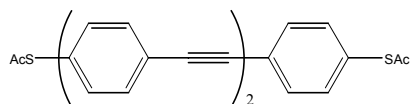
Compound 12 4-thioacetyl-trimethylsilylethynyl benzene(12) 270.9mg

(2.20mmol) 4-bromo, thioacetylbenzene, 43.9 mg Pd₂(dba)₃, 7.3 mg CuI, and 34.4 mg PPh₃ were placed in a schlenk flask, evacuated and backfilled with Argon. 5ml THF and 1.4 ml Hunig's Base were added by syringe. The solution was mixed and 460 μl of trimethylsilylacetylene was added. The mixture was sealed and stirred for 22 hours at 85°C. The reaction was then cooled and the solvent removed. The residue was filtered through Celite using Et₂O. The solvent was removed and the residue was separated using Column Chromatography on SiO₂ (24:1 hexanes/ Et₂O, R_f=0.34) to yield 536mg (73%) of a pale yellow solid. ¹H-NMR: 7.406(dd, 4H, J₁=55 Hz, J₂=8.6 Hz, Ar-H), 2.4273(s, 3H, Ac-CH₃), 0.2502(s, 9H, TMS-CH₃).

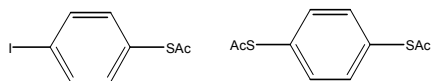


Compound 12A 4-thioacetyl-ethynyl benzene(12A) In a 30ml plastic bottle, 162 mg (0.67 mmol) **4-thioacetyl-trimethylsilylethynyl benzene(12)**, 4 drops conc. HF, 2.5 ml TBAF(1M in THF) were dissolved in 5 ml pyridine. The reaction mixture was stirred at room temperature for 2 hours and then quenched by adding SiO₂ gel. The mixture was then poured into 50ml of 5% HCl and extracted using 2X 20ml

EtOAc. The solvent was removed on the rotary evaporator and further dried on the vacuum manifold to remove remaining pyridine. The residue was then separated using column chromatography (SiO₂, 8:1 Pet Ether/Et₂O, R_f=0.36) to yield 59.4 mg(50%) as a yellow oil that solidified upon standing. ¹H-NMR: 7.4058(dd, 4H, J₁=54.8 Hz, J₂=8.3 Hz, Ar-H), 3.145(s, 1H, CC-H), 2.4301(s, 3H, Ac-CH₃).



Compound 13 PA3-2- 45.5mg(0.26mmol) of **4-thioacetyl-ethynal benzene(12A)**, 44.0 mg of 1,4-diiodobenzene, 5.2 mg Pd₂(dba)₃, 4.9 mg CuI, and 16 mg PPh₃ were placed in a schlenk flask, evacuated and backfilled with Argon. 0.5 ml TEA and 0.1 ml Hunig's Base were added by syringe. The mixture was sealed and stirred for 2 days at 55°C. The reaction was then cooled and diluted with 15 ml Et₂O and filtered through 1cm Celite. The plug was washed with an additional 50 ml Et₂O. The solvent was removed by rotary evaporation. The resulting yellow residue was separated using column chromatography (SiO₂, 2:1 Pet Ether/Et₂O, R_f = 0.30) to yield 32.3mg(63%) of a pale yellow solid. ¹H-NMR: 7.4812(dd, 8H, J₁=31.3 Hz, J₂=8.5 Hz, Ar-H), 7.5181(s, 4H, Ar-H), 2.449(s, 6H, Ac-CH₃).

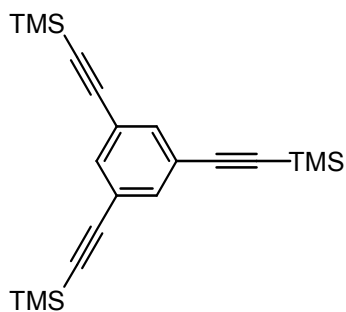


Compounds 14, 14 A 1,4,bis thioacetyl benzene(14),4-

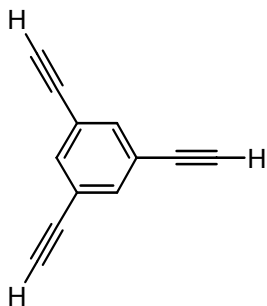
thioacetyl,iodobenzene(14A). 5.025 g 1,4-diiodobenzene(15.2 mmol) was placed in a 50 ml schlenk flask, evacuated, and backfilled with Argon. 15 ml of anhydrous THF was added by syringe. The mixture was then cooled to -78°C in a CO_2 /acetone bath. 30 ml of *t*-buLi(1.5M in pentane) was added dropwise over 1 hour by syringe. The mixture was stirred for 30 min at -78°C then warmed to room temperature and stirred an additional 30min before cooling back to -78°C . A suspension of 0.6082 g powdered Sulfur in 2 ml THF was cannulated onto the mixture while stirring vigorously. The reaction was allowed to warm up to room temperature and stir for one hour. The mixture was then cooled to -10°C and 1.6ml of distilled acetyl chloride was added dropwise by syringe. The mixture was then warmed to room temperature and stirred overnight before being poured into 50ml H_2O . The quenched solution was then extracted with DCM, dried over MgSO_4 , and roto-vapped. Separation using column chromatography (SiO_2 , 3:1 Pet Ether/ Et_2O) yields two products:

Product 1 – 3.3211g (78% yield) of 4-thioacetyl,iodobenzene(14A)($R_f=0.72$) was collected as pale yellow oil which solidified upon standing. $^1\text{H-NMR}$: 7.4353(dd, 4H, $J_1 = 122 \text{ Hz}$, $J_2 = 8.2 \text{ Hz}$, Ar-H), 2.4250(s, 3H, Ac- CH_3).

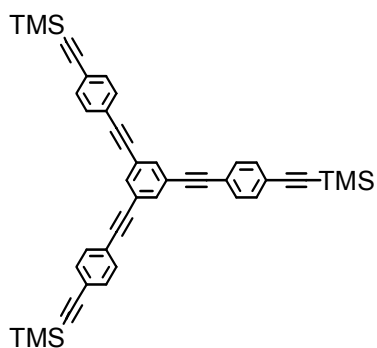
Product 2 – 0.655 g(87.8% of remaining product) of 1,4,bis thioacetyl benzene(14)($R_f=0.44$) was collected as a white solid. $^1\text{H-NMR}$: 7.4543(s, 4H, Ar-H), 2.436(s, 6H, Ac- CH_3).



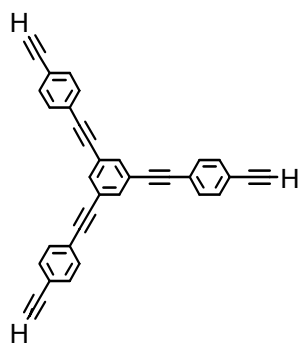
Compound 15- 1,3,5, tris(trimethylsilylethynyl)benzene 5.0036g (15.9mmol) of 1,3,5-tribromobenzene, 438.7 mg Pd₂(dba)₃, 485 mg CuI, and 747 mg PPh₃ were placed in a schlenk flask, evacuated and backfilled with Argon. 30ml THF and 8 ml NEt₃ were added by syringe. The solution was mixed and 7.4 ml of trimethylsilylacetylene was added. The mixture was sealed and stirred for 22 hours at 70°C. The reaction was then cooled and rotovaped to remove the solvent. The residue was filtered through Celite using Et₂O. The solvent was removed and the residue was separated using Column Chromatography (SiO₂, 2:1 Pet Ether/ Et₂O, R_f=0.7) to yield 2.26g (95%) of a white solid. ¹H-NMR: 7.615(s, 3H, Ar-H), 0.261(s, 27H, TMS-CH₃).



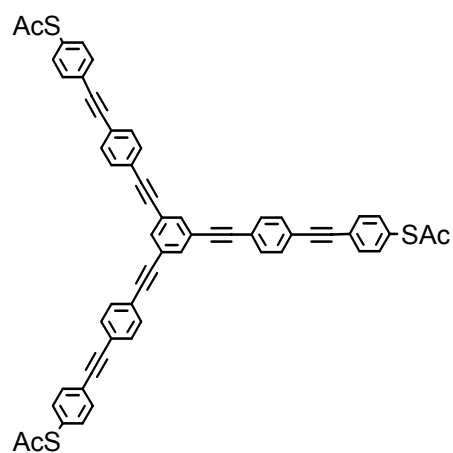
Compound 15A- 1,3,5, triethynyl benzene 227.6 mg of 15 was dissolved in 15ml of MeOH and a catalytic amount of K_2CO_3 was added. The mixture was stirred overnight at room temp. Upon completion, The solvent was removed by rotary evaporation. The resulting residue was filtered on 1cm of silica using CH_2Cl_2 as an eluent. The solvent was removed to yield 113.6 mg (99%) of the desired product as a white solid. 1H -NMR: 7.5704(s, 3H, Ar-H); 3.1052(s, 3H, CC-H).



Compound 17. 324 mg 15A, 2.1006g 2A, 98.9 g $Pd_2(dba)_3$, 160.8 mg CuI, and 262.2 mg PPh_3 were placed in a schlenk flask, evacuated and backfilled with Argon. 15ml THF and 7.5ml TEA were added by syringe. The mixture was sealed and stirred for 48 hours at $80^\circ C$. The reaction was then cooled and the solvent removed. The residue was filtered through Celite. The solvent was removed and the residue was separated using Column Chromatography (SiO_2 , 5:1 Pet Ether/ Et_2O , $R_f=0.36$) to yield a pale yellow solid which was carried on to make 17A. 1H -NMR: 7.6318(s, 3H, Ar-H), 7.4551(s, 12H, Ar-H), 0.26710(s, 27H, TMS- CH_3)

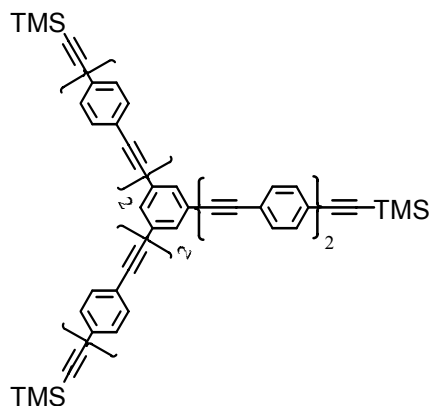


Compound 17A The collected product **17** was dissolved in 20ml of 1:1 MeOH/DCM and a catalytic amount of K_2CO_3 was added. The mixture was stirred overnight at room temp. Upon completion, The solvent was removed by rotary evaporation. The resulting residue was filtered on 1cm of silica using CH_2Cl_2 as an eluent. The solvent was removed to yield 343.5 mg (36% over two steps) of the desired product. 1H -NMR: 7.6317(s, 3H, Ar-H), 7.4845(s, 12H, Ar-H), 3.1915(3H, s, CC-H).



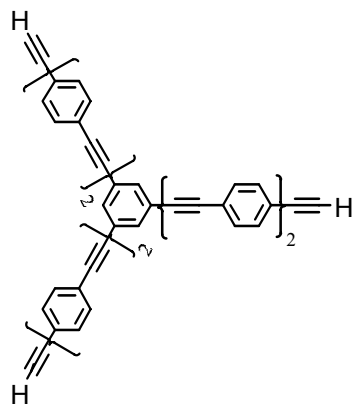
Compound 18 345.3 mg of 17A, 554.4 mg of 4-bromo-thioacetyl benzene, 66.8 mg $Pd_2(dba)_3$, 63.7 mg CuI, and 123.9 mg PPh_3 were placed in a schlenk flask,

evacuated and backfilled with Argon. 5 ml THF and 1.2 ml TEA was added by syringe. The mixture was sealed and stirred for 3 days at 65°C. The reaction was then cooled and the solvent removed. The residue was redissolved in Et₂O and filtered through 1cm Celite. The solvent was removed and the residue was separated using Column Chromatography (SiO₂, 2:1 Pet Ether/DCM, R_f = 0.26) to yield 256 mg (37%) as a pale yellow solid. ¹H-NMR: 7.6318(s, 3H, Ar-H), 7.512(dd, 12H, J₁= 31.2 Hz, J₂ = 8.4 Hz, Ar-H), 7.4558(s, 12H, Ar-H), 2.4612(s, 9H, Ac-H)

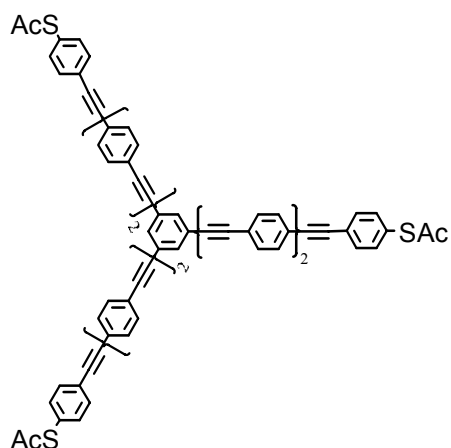


Compound 19. 229 mg (0.5 mmol) 17A, 501 mg 2A, 16.7 mg Pd₂(dba)₃, 14.8 mg CuI, and 36.8 mg PPh₃ were placed in a schlenk flask, evacuated and backfilled with Argon. 60ml THF and 11ml TEA were added by syringe. The mixture was sealed and stirred for 48 hours at 80°C. The reaction was then cooled and rotovaped to remove the solvent. The residue was filtered through Celite using Hexanes. The solvent was removed and the residue was separated using column chromatography (SiO₂, 1:1 Hexanes/DCM, R_f=0.6) to yield a yellow solid. ¹H-

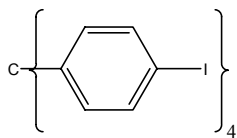
NMR: 7.68(s, 3H, Ar-H), 7.52(s, 12H, Ar-H), 7.46(s, 12H, Ar-H), 0.2610(s, 27H, TMS)



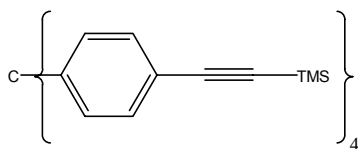
Compound 19A The collected product **19** was dissolved in 25ml of 5:1 MeOH/DCM and a catalytic amount of K_2CO_3 was added. The mixture was stirred overnight at room temp. Upon completion, The solvent was removed by rotary evaporation. The resulting residue was filtered on 1cm of silica using CH_2Cl_2 as an eluent. The solvent was removed to yield a pale yellow solid. 1H -NMR: 7.68(s, 3H, Ar-H), 7.52(s, 12H, Ar-H), 7.46(s, 12H, Ar-H), 3.105(s, 3H, CC-H)



Compound 20 381.7 (0.5 mmol) 19A, 380.6 mg of 4-bromo-thioacetyl benzene, 14 mg Pd₂(dba)₃, 15 mg CuI, and 24 mg PPh₃ were placed in a schlenk flask, evacuated and backfilled with Argon. 30 ml TEA was added by syringe. The mixture was sealed and stirred for 3 days at 85°C. The reaction was then cooled and the solvent removed. The residue was redissolved in Et₂O and filtered through 1cm Celite. The solvent was removed and the residue was separated using Column Chromatography (SiO₂, 1:1 Hexanes/DCM, R_f=0.57) to yield 256 mg (46%) as a yellow solid. ¹H-NMR: 7.6318(s, 3H, Ar-H), 7.512(dd, 12H, J₁=31.2 Hz, J₂=8.4 Hz, Ar-H), 7.4558(s, 24H, Ar-H), 2.4612(s, 9H, Ac-H)

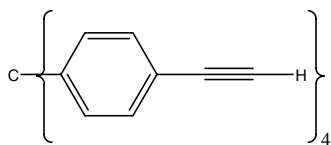


Compound 21(Tetrakis(4-iodophenyl)-methane) 0.815g (2.5mmol) CPh₄, 4.68 g Bis-(trifluoroacetic)-iodo-benzene, and 2.76 g I₂ were dissolved in 16.6 ml(0.15M) CHCl₃. The mixture was degassed using Argon, sealed, and stirred for 4 days at 55°C. The mixture was then washed (2X 10ml) with water. The organic layer was dried over MgSO₄ and the solvent removed to form a pale yellow oil. The solution was then washed with 25 ml EtOH, solvent decanted, 25 ml Acetone, solvent decanted, and then 50ml THF was added. The residue was then placed in the freezer at -10°C where white crystals formed overnight. The crystals were collected using vacuum filtration to yield 2.047g(99%) of a white solid. ¹H-NMR: 7.252(dd, 16H, J₁=140 Hz, J₂= 8.7 Hz, Ar-H).

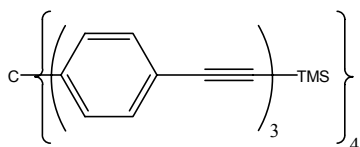


Compound 22- tetrakis(4-trimethylsilylacetylenebenzene)methane. 1.056 g(1.2mmol) of 21, 88.5 mg Pd₂(dba)₃, 91.8 mg CuI, and 252.2 mg PPh₃ were placed in a schlenk flask, evacuated and backfilled with Argon. 20ml TEA and 40ml benzene were added by syringe. The solution was mixed and 765 μl of trimethylsilylacetylene was added. The mixture was sealed and stirred for 2 days at 55°C. The reaction was then cooled and the solvent removed. The residue was filtered through Celite using Et₂O. The solvent was removed and the residue was

separated using Column chromatography (SiO₂, Pet Ether, R_f=0.04) to yield 623mg (73%) of a pale yellow solid. ¹H-NMR: 7.1877(dd, 16H, J₁=58.1 Hz, J₂=8.5 Hz, Ar-H), .2343(s, 36H, TMS-CH₃). ¹³C-NMR: 146.125, 131.62, 131.52, 130.87, 121.34, 104.74, 94.91, 0.103.

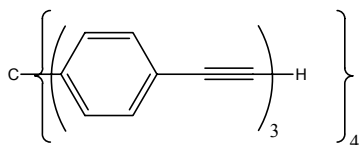


Compound 22A tetrakis(4-ethynylbenzene)methane - 50mg of 22 was dissolved in 20ml of 1:1 MeOH/DCM. A catalytic amount of K₂CO₃ was added and the mixture stirred for 3 hours. Upon completion, The solvent was removed by rotary evaporation. The resulting residue was filtered on 1cm of silica using CH₂Cl₂ as an eluent. The solvent was removed to yield 28.4 mg (95%) of the desired product. ¹H-NMR: 7.2582(dd, 16H, J₁=52.6 Hz, J₂=8.6 Hz, Ar-H), 3.0621(s, 4H, CC-H). ¹³C-NMR: 146.32, 131.92, 131.79, 130.87, 120.43, 83.31, 77.80, 1.178.

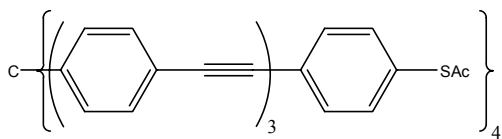


Compound 23, 51.8 mg(0.125 mmol) of 22A,214.6 mg 3A, 10 mg Pd₂(dba)₃, 4.7 mg CuI, and 26.6 mg PPh₃ were placed in a schlenk flask, evacuated and backfilled with Argon. 1 ml TEA and 5ml THF were added by syringe. The mixture was

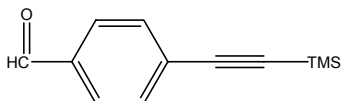
sealed and stirred for 2 days at 55°C. The reaction was then cooled and the solvent removed. The residue was filtered through Celite using Et₂O. The solvent was removed and the residue was separated using Column Chromatography (SiO₂, (5:1 Pet Ether/DCM, Rf=0.08) to yield a pale yellow solid which was carried on to make 23A. ¹H-NMR: 7.4975(s, 16H, Ar-H), 7.4514(s, 32H, Ar-H), 0.2561(s, 36H, TMS-CH₃). ¹³C-NMR: 146.17, 132.05, 131.71, 131.53, 131.30, 123.31, 123.25, 123.74, 123.00, 121.272, 96.58, 91.14, 89.72, 1.162



Compound 23A Products from above(23) were dissolved in 25 ml of 4:1 DCM/MeOH. A catalytic amount of K₂CO₃ was added and the mixture stirred overnight. Upon completion, The solvent was removed by rotary evaporation. The resulting residue was filtered on 1cm of silica using CH₂Cl₂ as an eluent. The eluent was roto-vapped to yield 101.8 mg(67% over two steps) of the desired product. ¹H-NMR: 7.503(s, 16H, Ar-H), 7.4776(s, 32H, Ar-H), 3.1803(s, 4H, CC-H). ¹³C-NMR: 146.18, 132.229, 131.72, 131.67, 131.48, 131.13, 131.15, 131.02, 123.50, 123.37, 122.93, 122.23, 121.26, 91.21, 91.17, 90.90, 89.72, 83.37, 39.29

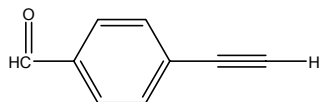


Compound 24 PA4-4; 101.8mg (0.083 mmol), 98.7 mg 11, 6.5 mg Pd₂(dba)₃, 6.1 mg CuI, and 17.5 mg PPh₃ were placed in a schlenk flask, evacuated and back-filled with Argon. 3 ml TEA and 10ml THF were added by syringe. The mixture was sealed and stirred for 2 days at 55°C. The reaction was then cooled and rotovapped to remove the solvent. The residue was filtered through Celite using Et₂O. The solvent was removed and the residue was separated using Column chromatography (SiO₂, 1:1 Pet Ether/DCM) to yield a pale yellow solid which was carried on to make 23A. ¹H-NMR: 7.5189(s, 32H, Ar-H), 7.4855(dd, 16H, J₁=30.9 Hz, J₂=8.5 Hz, Ar-H), 2.4418(s, 12H, Ac-CH₃)

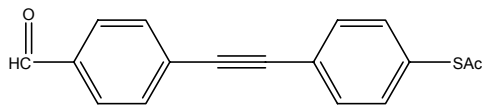


Compound 25 4-trimethylsilylethynyl-benzaldehyde 2.0111g 4-bromobenzaldehyde (10.8mmol), 193.3 mg Pd₂(dba)₃, 102.4 mg CuI, and 569.3mg PPh₃ were placed in a schlenk flask, evacuated and backfilled with Argon. 7 ml TEA and 36ml THF were added by syringe. The solution was mixed and 1.68 ml of trimethylsilylacetylene was added. The mixture was sealed and stirred for 2 days at 60°C. The reaction was then cooled and poured into 75 ml H₂O. This

mixture was then extracted with Et₂O(2X, 50ml), dried over MgSO₄ and the solvent removed. The residue was separated using column chromatography (SiO₂, 10:1 Pet Ether/Et₂O) to yield 2.1405 g (98%) of a pale yellow solid. ¹H-NMR: 9.9998(s, 1H, C(O)-H), 7.7103(dd, 4H, J₁=43.4 Hz, J₂=8.5 Hz, Ar-H), 0.2683(s, 3H, TMS-CH₃). ¹³C-NMR: 191.53, 135.71, 132.60, 129.56, 129.47, 103.96, 99.15, 0.075

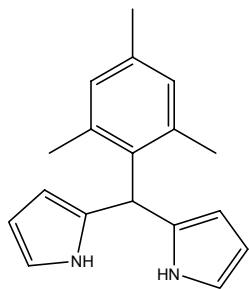


Compound 25A 4-ethynyl-benzaldehyde 0.75 g of 25 was dissolved in ml of MeOH. A catalytic amount of K₂CO₃ was added and the mixture stirred overnight. Upon completion, The solvent was removed by rotary evaporation. The resulting residue was filtered on 1cm of silica using CH₂Cl₂ as an eluent. The solvent was removed to yield 276.6 mg(57%) of the desired product. ¹H-NMR: 10.024(s, 1H, C(O)-H), 7.748(dd, 4H, J₁=40.9 Hz, J₂=7.7 Hz, Ar-H), 3.2977(s, 1H, CC-H). ¹³C-NMR: 191.49, 137.84, 136.08, 129.62, 128.43, 82.75, 81.20



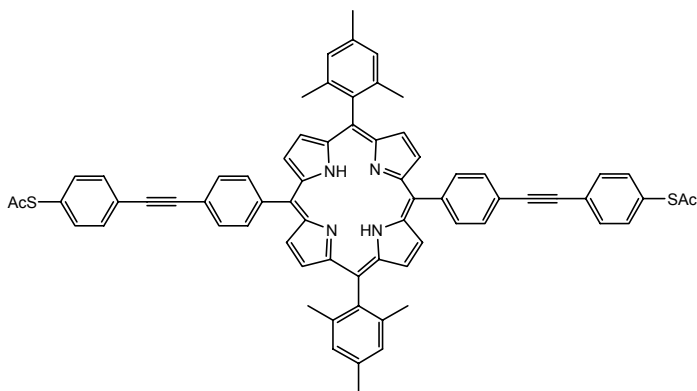
Compound 26 4-(4'-(acetyl)thiophenyl)ethynyl-benzaldehyde 149.8 mg of 25A, 320.4mg of 4-bromo,(acetyl)thiophenol, 27.6 mg Pd₂(dba)₃, 10.2 mg CuI, and 59.5

mg PPh₃ were placed in a schlenk flask, evacuated and back-filled with Argon. 1.2 ml TEA and 4 ml THF were added by syringe. The mixture was sealed and stirred for 30 hours at 60°C. The reaction was then cooled poured into 25 ml H₂O, extracted with Et₂O (3X, 30ml), dried over MgSO₄, and roto-vapped to remove the solvent. The residue was separated using column chromatography (SiO₂, 3:1 Pet Ether/Et₂O, R_f=0.25) to yield 151.7 mg (47%) of the desired product as an orange solid. ¹H-NMR: 10.0314(s, 1H, C(O)-H), 7.7813(dd, 4H, J₁=39.9 Hz, J₂=8.4 Hz, Ar-H), 7.5039(dd, 4H, J₁=31.5 Hz, J₂=8.2 Hz, Ar-H), 2.4487(s, 3H, Ac-CH₃)



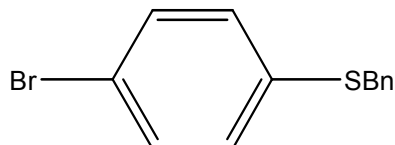
Compound 27 meso-mesityl-dipyrromethane. From ref(Lindsey, tetrahedron, 1994)A solution of Mesitaldehyde (1.47ml, 10mmol) was dissolved in 27.8ml(40mmol) freshly distilled pyrrole and degassed with Argon. 0.369ml of BF₃•OEt₂ was added by syringe and the mixture stirred for 30 min at room temperature. The mixture was then diluted with 50ml DCM and washed with 0.1M NaOH. The organic layers were dried over MgSO₄ and the solvent removed by rotary evaporation and then dried on the vacuum manifold to remove residual pyrrole to yield a light tan solid that was recrystallized from Cyclohexane to yield

1.4 g (55%) the dipyrromethane as a white solid. $^1\text{H-NMR}$: 7.93(bs, 2H, N-H), 6.87(s, 4H, Ar-H), 6.67(t, 2H, Pyrrole-H), 6.18(q, 2H, Pyrrole-H), 6.01(t, 2H, pyrrole-H), 5.92(s, 1H, *meso*-H), 2.633(s, 6H, mesityl-*p*-CH₃), 1.8437(s, 12H, mesityl-*o*-CH₃)

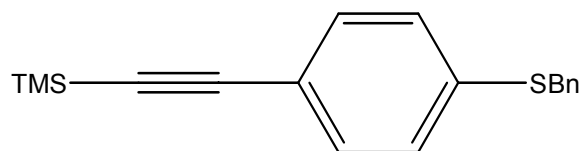


Compound 28-trans-dithiol Porphyrin 68.3 mg (0.258 mmol) of meso-mesityldipyrromethane(27) and 71.2 mg (0.256 mmol) of aldehyde 26 were added to a 50ml schlenk flask, evacuated and backfilled with argon. 25ml CHCl₃ was added by syringe. While stirring, 33 μl of BF₃•OEt₂ (2.5M in CHCl₃) was added by syringe. The mixture was stirred for one hour under argon purge before 48.3 mg DDQ was added. The mixture was stirred for another hour and then the solvent was removed by rotary evaporation. The mixture was separated using column chromatography (SiO₂, 2:1 DCM/Hexanes, R_f=0.7) to yield a dark colored solid. This residue was recrystallized from MeOH to yield 15.9 mg (12%) of the desired porphyrin as a bluish/purple solid. $^1\text{H-NMR}$: 8.765(dd, 8H, J₁=18.2 Hz, J₂=3.2 Hz, β -pyrrole), 8.0765(dd, 8H, J₁=61 Hz, J₂=5.3 Hz, Ar-H), 7.596(dd, 8H, J₁=44.42 Hz,

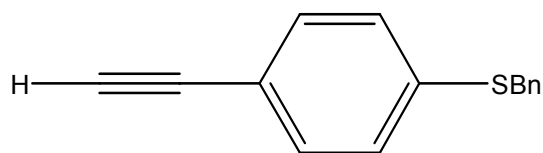
$J_2=5.46$ Hz, Ar-H), 7.288(s, 4H, Mesityl-H), 2.633(s, 6H, mesityl-*p*-CH₃), 2.467(s, 6H, Ac-CH₃), 1.8437(s, 12H, mesityl-*o*-CH₃), -2.791(s, 2H, porphyrin ring inner-H). $\lambda_{\text{max}}=250, 260, 418, 514, 550, 594, 650$



Compound 29 4-bromo,(benzyl)thiophenol 1.9975 g (10.5mmol) 4-bromothiophenol was dissolved in 36ml of THF and 6ml of 2M NaOH in Ethanol. The mixture was degassed by sparging with Argon for 20 min. 1.3 ml of benzyl bromide was added by syringe and the reaction stirred for 3 hours. The solvent was then removed using rotary evaporation and the residue was redissolved in 20 ml Et₂O. The solution was washed with water (2X 30ml), dried over MgSO₄, and the solvent removed to collect 2.923 g (99%) of the desire product as white solid. ¹H-NMR: 7.274(m, 5H, Bn-H), 7.2534(dd, 4H, $J_1=43.04$ Hz, $J_2=8.5$ Hz, Ar-H), 4.0854(s, 2H, Bn-CH₂). ¹³C-NMR: 137.174, 135.570, 131.986, 131.62, 129.110, 128.91, 129.482, 120.451, 39.2304.

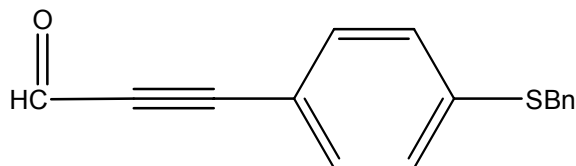


Compound 30 4-trimethylsilyylethynal, (benzyl)thiophenol 2.429 g(7.7 mmol) of Compound 29, 154 mg Pd₂(dba)₃, 72.5 mg CuI, and 404.7 mg PPh₃ were placed in a schlenk flask, evacuated and backfilled with Argon. 5ml TEA and 25ml benzene were added by syringe. The solution was mixed and 1.29 ml of trimethylsilylacetylene was added. The mixture was sealed and stirred for 30 hours at 65°C. The reaction was then cooled and the solvent removed. The residue was filtered through Celite using Et₂O. The solvent was removed and the residue was separated using column chromatography (SiO₂, 5:1 Pet Ether/Et₂O, R_f=0.8) to yield 2.5271g (98%) of a pale yellow solid. ¹H-NMR: 7.2894(dd, 4H, J₁=28.3 Hz, J₂=8.6 Hz, Ar-H), 7.2815(m, 5H, Bn-H), 4.1237(s, 2H, Bn-CH₂), 0.2407(s, 9H, TMS-CH₃).

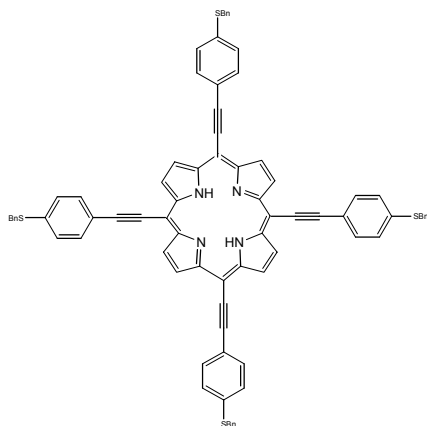


Compound 30A 4-ethynal,(benzyl)thiophenol 1.0012 g of compound 30 was dissolved in 30 ml MeOH. A catalytic amount of K₂CO₃ was added and the mixture stirred overnight. Upon completion, the solvent was removed by rotary evaporation. The resulting residue was filtered on 1cm of silica using 5:1 Pet Ether/Et₂O as an eluent. The solvent was removed to yield 741.6 mg(98%) of the

desired product as a yellow solid. $^1\text{H-NMR}$: 7.3001(dd, 4H, $J_1=28.3$ Hz, $J_2=5.6$ Hz, Ar-H), 7.3021(m, 5H, Bn-H), 4.1437(s, 2H, Bn- CH_2), 3.0807(s, 1H, CC-H).



Compound 31¹⁶4-propynal(benzyl)thiophenol In a 50 ml schlenk flask, 232.1 mg(0.01 mmol) compound 30A as evacuated, backfilled with Argon, and dissolved in 2 ml THF by syringe. The flask was cooled to -78°C and 0.43 ml (1.3 mmol) methyl MgBr (3M in Et_2O) was added dropwise by syringe. The reaction was stirred for 30 min at -78°C and then allowed to warm to room temperature while stirring for 1 hour before cooling back to -78°C . 100 μl (1.3mmol) of DMF was added dropwise by syringe and then stirred for 2 hours while allowing to warm to room temperature. To the mixture was added 20 ml 5% H_2SO_4 (aq.) and 20 ml Et_2O with a trace of hydroquinone before stirring overnight. The phases were then separated and the aqueous phase extracted with H_2O (2X 10ml). The organic layers were all combined, dried over MgSO_4 , and roto-vapped to dryness. The residue was separated using column chromatography (SiO_2 , 5:1 Pet Ether/ Et_2O , $R_f=0.8$) to yield 137.6 mg (42%) was a yellow solid. $^1\text{H-NMR}$: 9.404(s, 1H, C(O)H), 7.3718(dd, 4H, $J_1 = 40.16$ Hz, $J_2=5.6$ Hz, Ar-H), 7.3496(m, 5H, Bn-H), 4.1996(s, 2H, Bn- CH_2). $^{13}\text{C-NMR}$: 176.53, 142.50, 136.116, 133.51, 128.68, 127.54, 127.36, 115.91, 95/13, 89.07, 37.24



Compound 32 tetrakis, thiol porphyrin (HLAnderson, 1998, 1607) 25.5 mg

(0.1011) Compound 31 and 6.9 ul (0.1011) freshly distilled pyrrole were degassed in a 30 ml schlenk flask by purging with argon for 20 min. before dissolving in 10 ml of distilled DCM. The mixture was cooled to -40°C using an acetonitrile/ CO_2 bath before 2 drops of $\text{BF}_3 \bullet \text{OEt}_2$ was added. The mixture was allowed to warm to room temperature while being stirred overnight. 15 mg of DDQ was then added and the reaction was stirred for one hour. The solvent was then removed by rotary evaporation. The resulting residue was then purified using column chromatography (SiO_2 , DCM) to yield (6%) of the desired porphyrin as a green solid. $^1\text{H-NMR}$: 9.2766(s, 8H, β -pyrrole-H), 7.7075(dd, 16H, $J_1=79.84$ Hz, $J_2=5.32$ Hz, Ar-H), 7.4294(m, 40H, Bn-H), 4.3428(s, 8H, Bn- CH_2). λ_{max} , 283, 473, 648, 740, 894

Chapter Two References

1. a) RF Khairutdinov, *Colloid J.* **1997**, 59, 535; b) "Single Charge Tunneling and Coulomb Blockade Phenomena in Nanostructures" NATO ASI Ser. Ser. B 1992, 294
2. a) X. Peng, TE Wilson, AP Alivisatos, PG Schultz, *Angew. Chem. Intl. Ed. Engl.* **1997**, 36, 145; b) LC Brousseau, JP Novak, SM Marinakos, DL Feldheim, *Adv. Mat.* **1999**, 11, 447; c) JP Novak, DL Feldheim, *J. Am. Chem. Soc.*, **2000**, 122, 3979
3. a) J Zhang, JS Moore, Z Xu, RA Aguirre, *J. Am. Chem. Soc.*, 1992, 114, 2273 b) D Su, FM Menger, *Tett. Lett.* **1997**, 38, 1485 c) O. Levastre, S Cobioch, PH Dixneuf, *Tetrahedron*, **1997**, 53, 7595 d) RP Hsung, JR Babcock, CE D Chidsey, LR Sita, *Tetrahedron*, **1995**, 36, 4525 e) RP Hsung, CED Chidsey, LR Sita, *Organometallics*, **1995**, 14, 4808; f) JM Tour, *Chem Rev.* **1996**, 96 (1), 1377; g) L Jones, II, JS Schumm, JM Tour, *J. Org. Chem.* **1997**, 62, 1388
4. DB Janes, VR Kolagunta, RG osifchin, JD Bielefeld, RP Andres, JI Henderson, CP Kubiak, *Superlattices and Microstructures*, **1995**, 18 (4), 275
5. a) K Sonogashira, Y Tohda, N Hagihara, *Tett. Lett.* **1975**, 4467; b) HA Dierk, RF Heck, *J. Organomet. Chem.* **1975**, 93, 259
6. a) H Ku, JR Barrio, *J. Org. Chem.* **1981**, 46, 2280; b) EB Merkushev, *Synthesis*, **1988**, 923
7. Su, FM Menger, *Tett. Lett.* **1997**, 38 (9), 1485
- 8., J Lee, JS Lindsey, *Tetrahedron*, **1994**, 50 (39), 11427
9. HL Anderson, *Tett. Lett.* **1992**, 33 (8), 1101; b) GS Wilson, HL Anderson, *Synlett*, Nov **1996**, 1039
10. Kruithof, RF Shmitz, GW Klumpp, *Tetrahedron* **1982**, 39 (19), 3073

Chapter 3
Synthesis of Organically Bridged Metal
Nanoparticle Arrays

Introduction

Inorganic clusters of nanometer dimensions have been known for many years. Their optical properties have been known since days of the Roman Empire¹. More recently, investigations of inorganic nanoparticles have started to reveal fundamental properties and how they relate to size, shape, and composition². Much of the research has focused on the collective response of single particles or two-dimensional and three-dimensional arrangements of clusters³. Separation distance and interparticle medium greatly affect optical responses and electronic conduction in this arrangements⁴. These observations have prompted the use of nanoparticles in applications dealing with DNA detection⁵ and chemical sensors⁶.

Despite all the advances in studying nanoparticles, fundamental interactions have been largely left alone. One reason fundamental interactions between discrete collections of nanoparticles have not been studied is the lack of assembly methods that control symmetry and interparticle distance. Controlling the number of particles allows us to isolate the effects of symmetry and interparticle distance when studying nanoparticle communications. Herein is described a method for assembling discrete numbers of particles into geometrically defined arrays using organic template molecules⁷.

Richard Feynman proposed nearly 50 years ago that there is “plenty of room at the bottom.”⁸. He was referring to the future, forecasting the ability to manipulate systems on increasingly smaller levels. Chemical assembly is one method to manipulate building blocks on a molecular or nanoscale level.

Feynman's thoughts are coming true. Chemical self-assembly has been used in many areas of nanotechnology to build interesting structures with desired patterns. Most examples use some type of template to control the structure of interest. For example, metal rods and nanotubules have been synthesized using porous membranes⁹. Solid, flat surfaces have been used to synthesize self-assemble monolayers¹⁰ (SAMS). Micelles¹¹ and dendrimers¹² have been used to synthesize nanoparticles. Our strategy for chemical assembly involves having a rigid linker with ends that chemically bind to nanoparticles and hold them with a symmetry the symmetry of the linker.

We have chosen Phenyl acetylene molecules as our linkers. These linkers are advantageous because they are rigid and can be synthesized in various geometries. These type linkers have known synthesis¹³ and can be made with varying end groups. These end groups can be tuned to correspond to the nanoparticle¹⁴ of choice. The synthesis of these linkers has been previously described in Chapter 2 of this dissertation. These structures are shown in Figure 3.1. Our nomenclature describes the number of units in an arm and the number of arms. For example, A PA2-3 linker has 3 arms and 2 phenyl acetylene units per arm.

Gold and Silver nanoparticles are chosen due to their physical properties. These metal nanoparticles are widely studied in the literature and show some remarkable electronic¹⁴ and optical properties¹⁴. These properties will be discussed in forthcoming chapters. Gold¹⁵ and Silver¹⁶ were also chosen for their ease of

synthesis. Preparations have been published that allow for control over size, shape, and size dispersity. These metal nanoparticles are mixed with an organic linker who acts like a template to control the geometry of the resulting array.

Experimental

Linker synthesis was previously described. Linker structures are shown in Figure 3.1. 10nm Gold particles were synthesized using a citrate reduction¹⁵ and used as prepared. Briefly, (0.5 mmol) HAuCl₄ (Aldirch, 99.9%) was dissolved in 500ml H₂O (18MΩ Milli-Q) and brought to a boil. While refluxing, 100ml of 38.8mM Na₃Citrate in water was added rapidly while stirring vigorously. The solution turned a deep garnet red within 30min. The solution was then refluxed an additional 3 hours. The solution was cooled and stored in a dark glass bottle at 4°C. 5nm Au particles and 10nm Ag particles were purchased from Ted Pella, Inc. 30nm Ag particles were prepared in a similar manner to the Au using AgNO₃ (Fisher, 99%) as a starting material. All glassware was washed in a KOH/EtOH bath and rinsed with copious amounts of DI water. Stirbars were cleaned using a piranha solution (3:1, conc. H₂SO₄ and 30% H₂O₂).

Transmission Electron Microscope (TEM) images were obtained on a Philips CM12 Microscope operated at 25kV. Images were obtained using a Gaton CCD camera, model 673-0200. The digital images were stored in Zip Drive format and manipulated using the NIH Image(Macintosh) or SCion Image (PC) software.

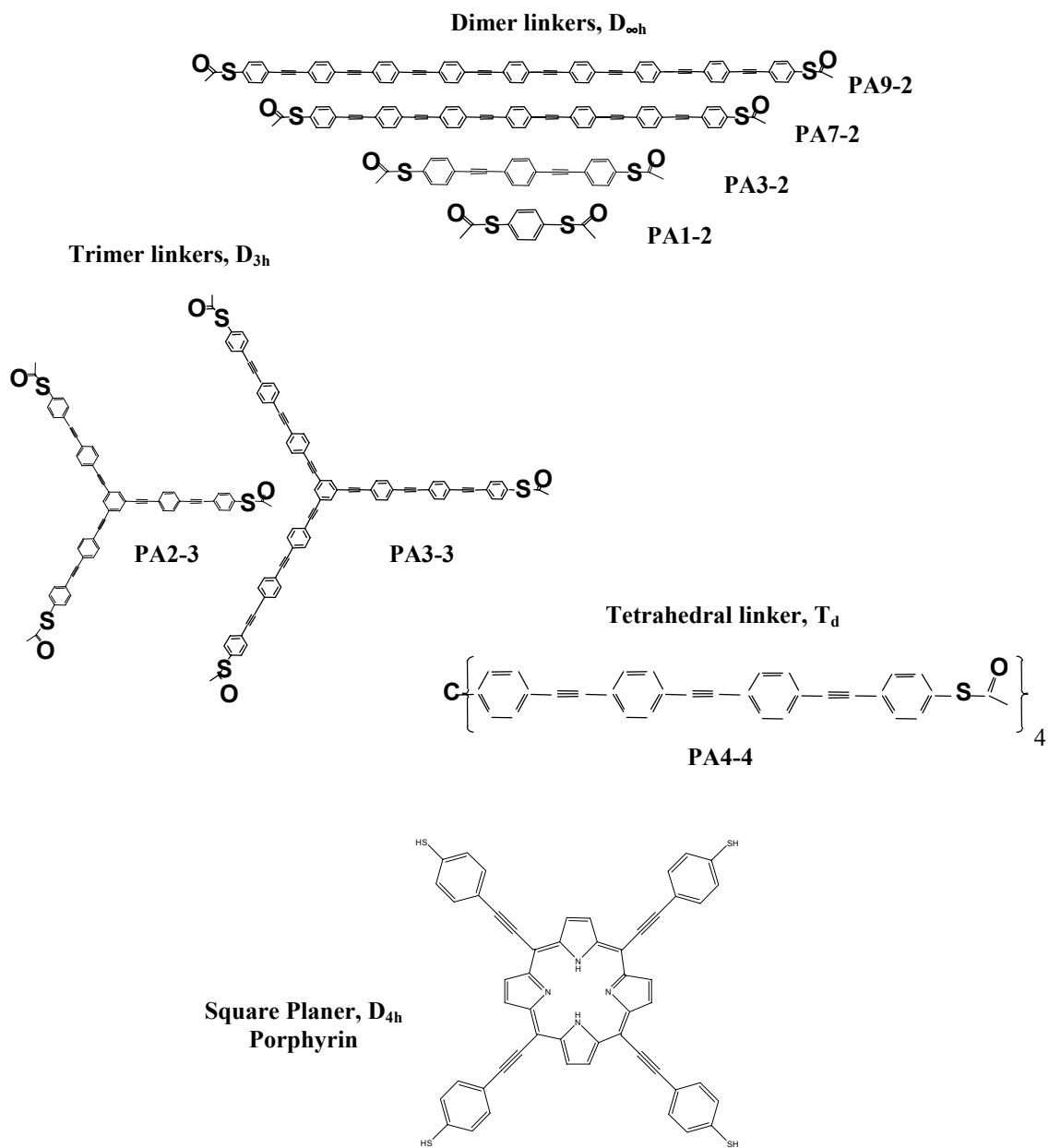


Figure 3.1 Phenylacetylene based linking bridge structures. Core geometry dictates symmetry of molecule and nanoparticle arrays.

The general linking procedure for the gold nanoparticle arrays is as follows. Two solutions are prepared and then mixed together. The first is the nanoparticle sol that is diluted. 2.00ml of nanoparticle solution is diluted with 2.50ml of a 3mM citrate solution. The citrate is used to buffer the stability of the particles. A second solution is prepared by adding a stoichiometric amount of linker from a 1μM stock solution and diluting to 500μl with the 2:3 THF ethanol solvent. While stirring, the linker solution is added in controlled aliquots over a period of 1-1.5 hours. This is usually done with 50μl aliquots at 10-minute intervals until completely delivered. The solutions are left to stir for an additional two hours to complete the linking procedure.

The procedure to link the Ag nanoparticles is slightly different. 100 μl of a 1μM linker solution was diluted with 5 ml of 3:2 EtOH/THF and 10 ml of water. 2 ml of a 1nM Ag nanoparticle sol was quickly added while stirring. The solution was then stirred for one day.

The thiol-terminated linkers are added in the acetyl-protected form. The slightly basic conditions (~pH=8) of the 3mM citrate is enough to deprotect the linkers *in situ*. If desired, spiking a 10ul amount of concentrated NH₄OH can accelerate the deprotection and facilitate nanoparticle linking. This is usually not performed in the gold samples due to irreversible agglomeration. The base is added to the Ag sols as the thiol-Ag bond is not formed as readily when protected.

During the linking procedure, linear optical properties were monitored. These are discussed in the next chapter.

Upon completion of the linking procedure the samples are analyzed using Transmission Electron Microscopy (TEM). Grids are formvar coated Cu with a 400 mesh from Ted Pella, Inc(#08121). The grid preparation is as follows. One drop of the reaction is placed on the grid, film side up, whilst holding with tweezers on the edge. The drop is held to the surface by surface tension. The grid is then touched to a Chem-wipe or filter paper so that the liquid is drawn through the grid and not off the outside. The contents of the drop are then deposited on the surface of the grid. A total of 5-8 drops are added to each grid depending on concentration of the initial gold sol. Less concentrated sols required more drops. TEM was used to observe the structures and count the reaction yield. Yields were estimated by counting 50-100 structures and noting the symmetry.

An important aspect of this procedure was the incompatibility between the solvents of the metal sols and the organic linkers. These organic linkers were only soluble in very soluble, relatively polar solvents such as DCM, CHCl_3 , Et_2O and THF. We were able to solublize very small quantities of linkers in an 3:2 ethanol/THF mixture. This works out well as the particle sols are in the nM range, so the required amount of linker is small. This ethanol/THF mixture is then soluble in water. If the linker is added to the sols using a immiscible liquid it will cause the particles to precipitate on the liquid-liquid interface or the walls of the container. If too much organic solvent is added, it disturbs the dielectric constant and therefore

the double layer repulsion mechanism that stabilizes the particles. This will cause an irreversible aggregation of the particles in the sol characterized by a dark blue color in the sample. This color change can be followed by precipitation depending on the amount of organic solvent added. The total amount of organic solvent added should not exceed 25% by volume in order to retain solubility and stability of the nanoparticle sol. Of course, the less organic content the more stable the nanoparticle solution.

Results and Discussion: Au Nanoparticle Arrays

When a di-thiol linker such as PA7-2 is introduced to the solution, structures with two particles are seen. The estimated yield is about 30% dimers and 70% unreacted monomers. As can be seen from the TEM images (Figure 3.2) there are no other structures than the expected dimers and unreacted species. Control experiments using 1,6-hexane dithiol under similar conditions did not yield the same desired structures. When the experiment is repeated using the tri-thiol linker, PA3-2 trimer type structures with a pseudo-D_{3h} symmetry are seen. These structures, such as the ones shown in Figure 3.3, are seen with about a 25% yield. The remaining structures are unreacted monomers (55 %) and partially reacted dimers (20%). Again there are no other structures other than the desired trimers and the un- or partially reacted particles. Other symmetries can also be made.

A tetra-substituted carbon core linker yielded about 10% tetrahedral 10 nm nanoparticle structures as shown in Figure 3.4. A porphyrin based core yielded

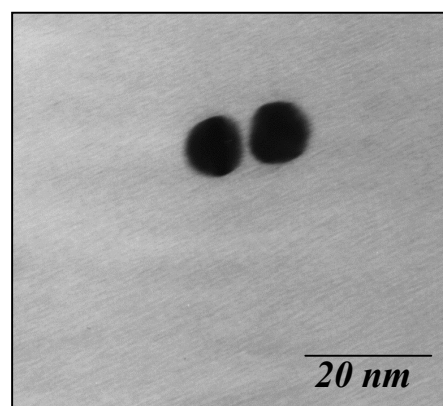
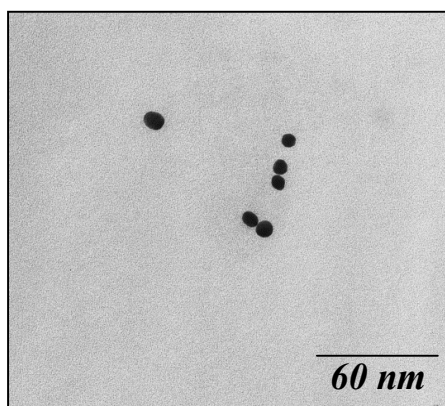
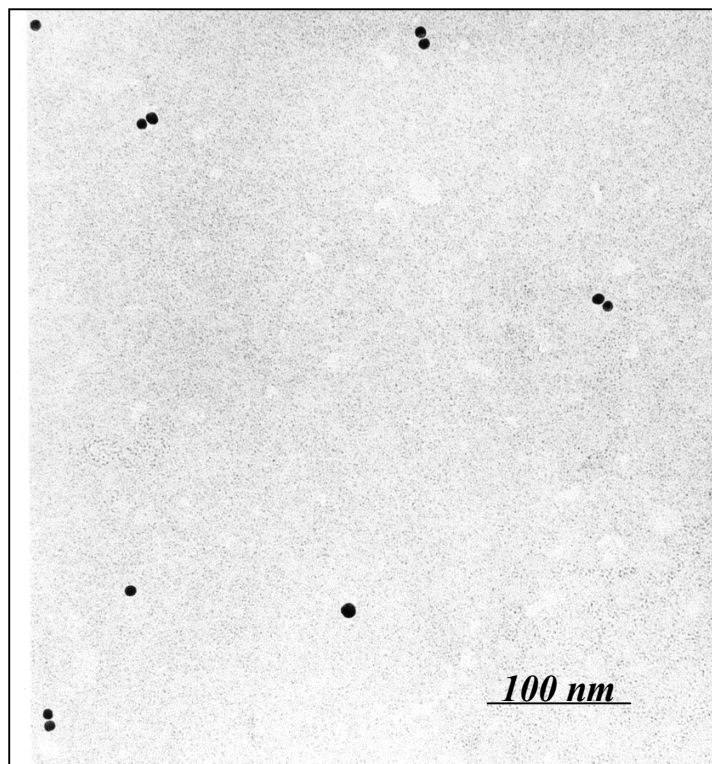


Figure 3.2. Transmission Electron Microscopy images of templated nanoparticle dimers. Images show that nanoparticles are not touching. Symmetry matches that of PA7-2 used in experiment.

square planer 5 nm nanoparticle structures. The interparticle distance measured using the porphyrin template was measured at 2.3nm. This is consistent with the

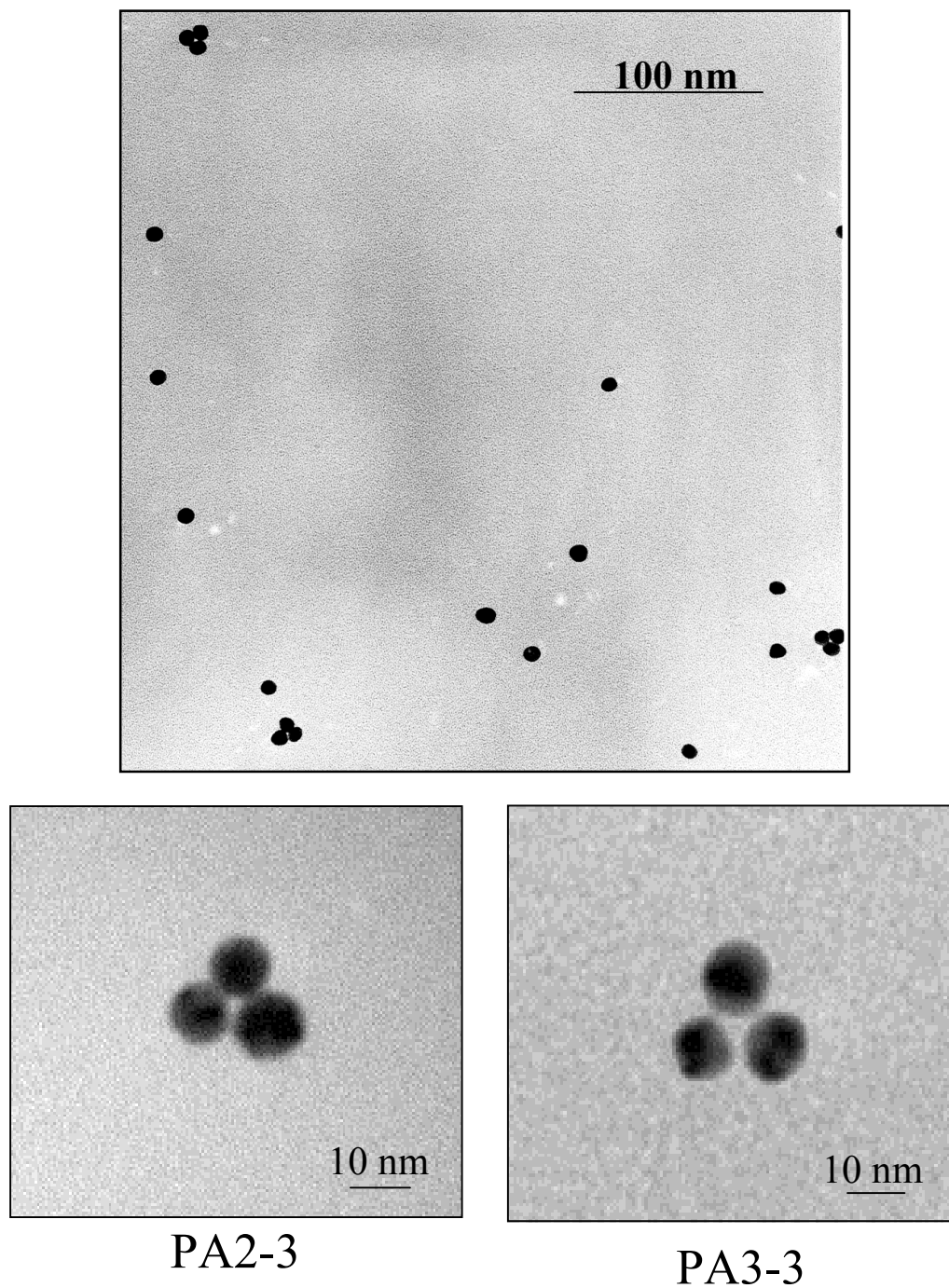


Figure 3.3. Transmission Electron Microscopy image showing 10 nm Au nanoparticle trimers. Longer linker PA3-3 shows greater interparticle distance compared to PA2-3.

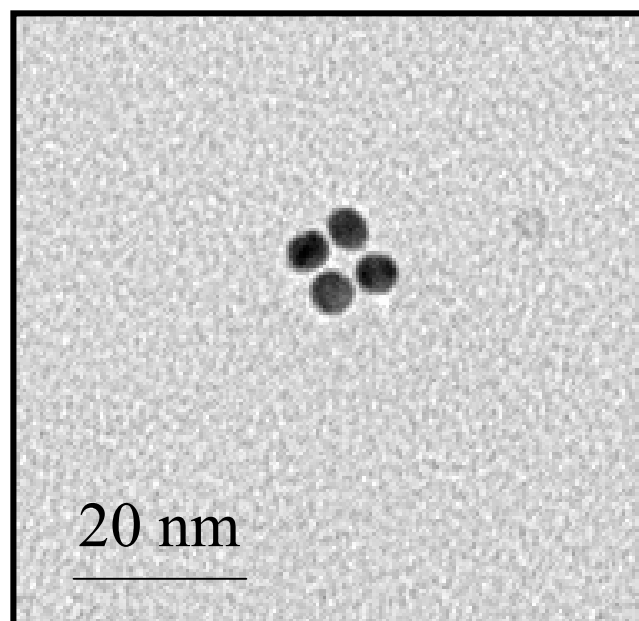
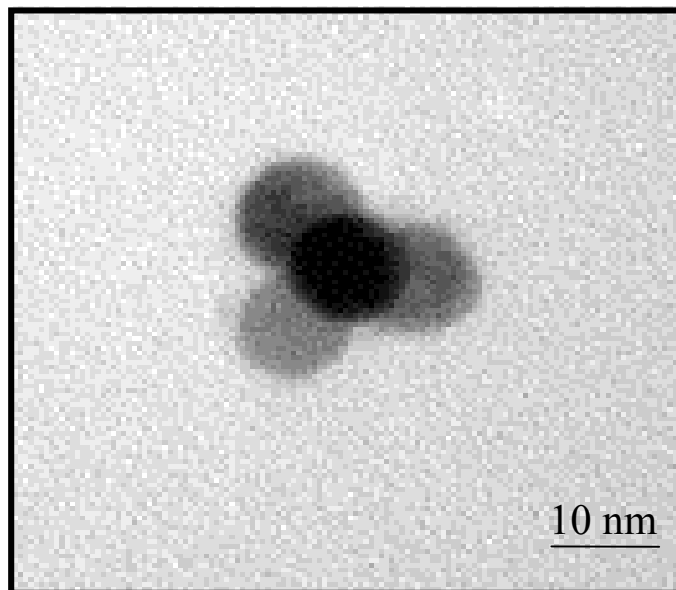


Figure 3.4. TEM images of 10 nm Au nanoparticle arrays. PA4-4(top) linker yield tetrahedral array symmetry. Tetra-thiol porphyrin(bottom) linkers yield square planer 5 nm nanoparticle arrays. Measured interparticle distance of 2.3nm is consistent with porphyrin dimensions.

distance between opposite thiol groups on the molecule. It is important to note that the porphyrin-based structures were present in very low yields. Due to synthetic requirements, a benzyl-protecting group was used instead of acetyl group in the synthesis. This benzyl group is difficult to deprotect under mild conditions. The harsh conditions (sodium azide) would likely decompose the sample prior to linking. As we see from the various TEM images, structures of varying symmetry can be prepared based on the linking molecule.

In addition to controlling symmetry we can control the interparticle separation. Various lengths of the tri-thiol linkers were synthesized. These arms would hold the particles at corresponding increased separation. These separation distances can be seen in Figure 3.3 b and 3.3 c. Similar experiments with linear linkers provided different results. It appears that we are unable to observe a difference in interparticle separation using TEM. One explanation could be the thiol bond exists on the surface of Au at an angle up to about 30° from normal. This is usually on flat substrates in SAM chemistry¹⁰. While this is usually attributed to maximizing the interaction between neighboring molecules, it tells us that the Au bond is flexible. When considering the size of the particles compared to that of the linker we see that a 5 deg change in bond angle can result in a several nanometer change in perceived particle separation distance. This may not be observed in the trimer structures due to the steric interference of neighboring particles.

Results and Discussion: Ag Nanoparticle Arrays

Similar structures can be made with Ag as with Au. 30 nm Ag dimers have been made and investigated for optical properties described in subsequent chapters. These dimer structures are shown in Figure 3.5. Due to the lack of suitable sizes of particles, the Ag dimers were the first synthesized. The two linkers used in these experiments, PA7-2 and PA3-2 respectively should show a difference in interparticle distance. This, like with the Au particles, is not seen. We believe that the same reasons apply for these nanoparticles as described above for the Au nanoparticles.

The trimer linkers will not allow for linking of 30nm particles. The arm length would have to be another two units long. A simple calculation can be derived to calculate the required distance from the core of the molecule to the surface of the particle. This was discussed in Chapter 2. In each equation, X is the length of the arm in nm and R is the radius of the nanoparticle in nm. For trimers: $X = R/\text{Cos } 30^\circ - R$ (3.1). For tetrahedron: $X = R/\text{Cos } 35^\circ - R$ (3.2). However, if 10nm Ag particles are used, trimer structures can be made using the appropriate linker. Figure 3.6 shows TEM images of these 10nm Ag trimers. The yields for the Ag nanoparticle arrays, dimers and trimers, are consistent with those of the Au experiments. That is, approximately 30% and 20% trimers are seen with no other symmetries other than those of the desired structures are observed.

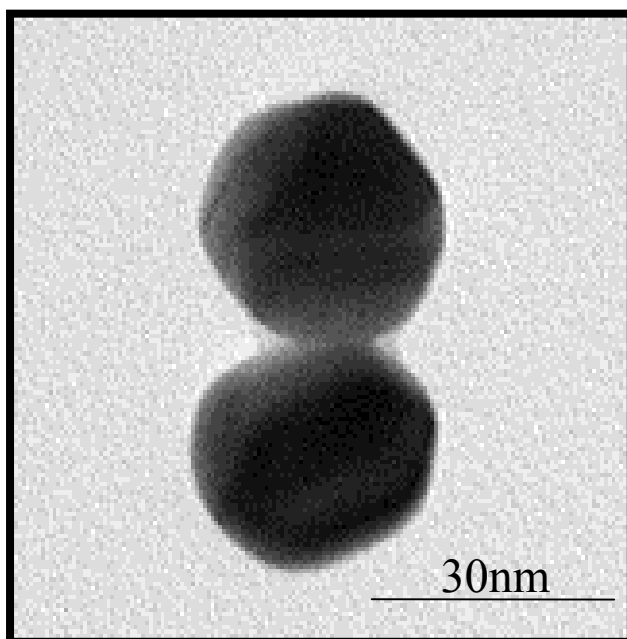
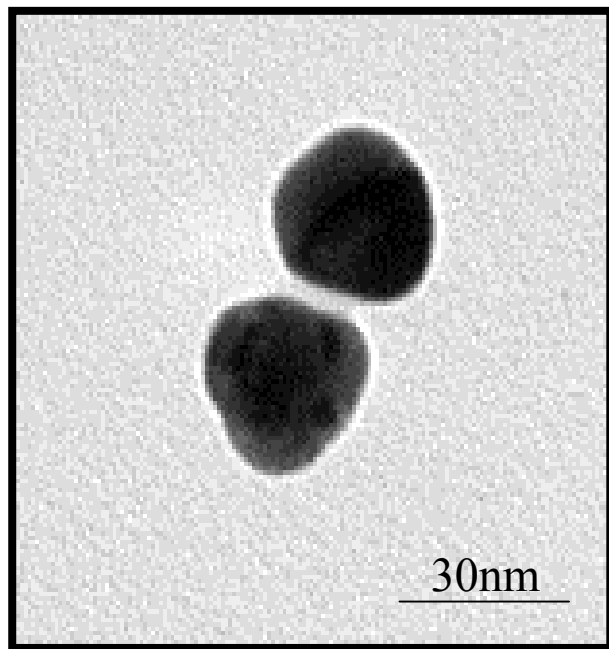


Figure 3.5. TEM image of 30 nm Ag dimers. Particle arrays were linked With PA7-2(top) and PA3-2(bottom).

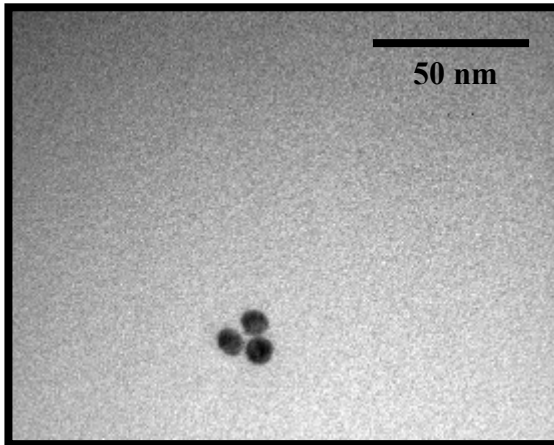
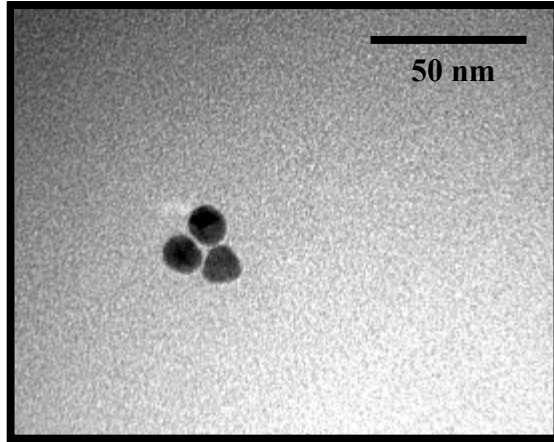


Figure 3.6 Transmission Electron Microscopy image of 10 nm Ag trimers.

Conclusions

As can be seen from the TEM images, nanoparticle arrays with controlled symmetry can be synthesized using an organic linker. The symmetry of the linker controls the symmetry of the nanoparticle arrays. An increased separation distance in the nanoparticle array was observed by changing the length of the arm on the linker. The separation distances measured were consistent with the dimensions of the template.

Chapter Three References

1. *Clusters and Colloids* G. Schmid, Ed. VCH, Weinheim, **1994**
2. a) DL Feldheim, CD Keating, *Chem. Soc. Rev.* **1998**, 27, 1; b) P. Mulvaney, *Langmuir*, **1996**, 12, 788; b) RF Khairutdinov, *Colloid J.* **1997**, 59, 535; c) P Mulvaney, *Langmuir*, **1996**, 12, 788; d) MM Alvarez, JT Khoury, TG Schaff, MN Shafigullin, I Verzner, RL Whetten, *J. Phys. Chem. B* **1997**, 101, 3706; e) S Peschel, G Schmid, *Angew. Chem. Int. Ed Engl.*, **1995**, 34, 1442; f) VL Colvin, AN Goldstein, AP Alivisatos, *J. Am. Chem. Soc.* **1992**, 114, 5221
3. a) KV Sarathy, PJ Thomas, GV Kulkarni, CNR Rao, *J. Phys. Chem. B* **1999**, 103, 399 b) CB Murray, CR Kagen, MG Bawendi, *Science*, **1996**, 270, 1335; c) JJ Shiang, JR Heath, CP Collier, RJSaykelly, *J. Phys. Chem. B* **1998**, 102, 3425
4. S. Henrichs, CP Collier, RJ Saykelly, TR Shen, JR Heath, *J. Am. Chem. Soc.* **2000**, 122, 4077
5. a) CA Mirkin, RL Letsinger, RC Mucic, JJ Storhoff, *Nature*, **1996**, 382, 607
6. H Hohltjen, AW Snow, *Anal. Chem.* **1998**, 70, 2856
7. a) LC Brousseau, III, JP Novak, SM Marinakos, DL Feldheim, *Adv. Mat.* **1999**, 11, 447; b) JP Novak, DL Feldheim, *J. Am. Chem. Soc.*, **2000**, 122, 3979
8. RP Feynman, *Engineering and Science*, **1959**, 22
9. Chuck Martin, *Acc. Chem. Research.* **1995**, 28, 61.
10. A Ullman, *Chem. Rev.* **1996**, 1533
11. micelles CdSe prep that Miles used?
12. V Chechik, M Zhao, RM Crooks, *J. Am. Chem. Soc.* **1999**
13. a) J Zhang, JS Moore, Z Xu, RA Aguirre, *J. Am. Chem. Soc.*, 1992, 114, 2273 b) D Su, FM Menger, *Tett. Lett.* **1997**, 38, 1485 c) O. Levastre, S Cobioc, PH Dixneuf, *Tetrahedron*, **1997**, 53, 7595 d) RP Hsung, JR Babcock, CE D Chidsey, LR Sita, *Tetrahedron*, **1995**, 36, 4525 e) RP Hsung, CED Chidsey, LR Sita, *Organometallics*, **1995**, 14, 4808
14. a) RP Andres, Jp Bielefeld, JI Henderson, DB Janes, VR Kolagunta, CP Kubiak, WJ Mahoney, RG Osifchin, *Science*, **1996**, 273, 1960; b) DL Klein, PL McEwen, JE Bowen-Katari, R Roth, AP Alivisatos, *App. Phys. Lett.* **1996**, 68 (18)

2574; c) M Dorogi, J Gomez, RG Osifchin, RP Andres, R Reifenberger, *Phys. Rev. B* **1995**, 52 (12), 9071; d) SJ Green, JJ Stokes, MJ Hostetler, J Pietrum, RW Murray, *J. Phys. Chem.* **1997**, 101, 2663

15. J Turkevich, PC Stevenson, J Hillier, *Discuss. Faraday Trans.* **1951**, 11, 55; RG Freeman, KC Graber, KJ Allison, RM Bright, JA Davis, AP Guthrie, MB Hommer, MA Jackson, PC Smith, DG Walter, MJ Natan, *Science*, **1995**, 267, 1629; b) RG Freeman, KC Graber, KJ Allison, RM Bright, JA Davis, AP Guthrie, MB Hommer, MA Jackson, PC Smith, DG Walter, Natan, *J. Am. Chem. Soc.* **1996**, 119, 1148

16. Lee, Meisel, *J. Phys. Chem.*, **1982**, 86, 3391

17. Van Der Zande, et al, *Langmuir*, **2000**, 16, 459

Chapter 4

**Electromagnetic Coupling in Organically-Bridged
Nanoparticle Arrays**

Introduction

Recent interest in the optical properties of metal nanoparticles continues to evolve as new synthetic methods for controlling their size and shape¹ are developed. Optical properties of individual particles and aggregates of nanoparticles, both in solution and attached to surfaces, have been investigated. Linear optical properties have been studied on bulk solutions using UV-Vis absorbance. In addition, small groups of particles have been studied using Scanning Tunneling Microscopy (STM)³, Atomic Force Microscopy (AFM), Surface Enhanced Raman Spectroscopy (SERS)⁴, electron microscopy, and near field optical methods.

Nanoparticles made from noble metals act like their bulk counterparts. These metal clusters have free electrons in sizes greater than 2 nm⁵. Due to their size and shape, These free electrons are confined to the surface of the particles and contribute to the surface plasmon resonance⁶ (SPR). The SPR gives the nanoparticles a characteristic, intense absorbance in the visible region.

The surface plasmon resonance is due to electrons oscillating coherently with light. Electrons “slosh” back and forth off the surface of the particle and can be described by the polarizability of the particle. The polarizability of each particle creates a dipole. There is interaction between particles as they come close enough for the dipoles to couple. Basically this means the closer the particles are to each other, the more they interact. This chapter describes the linear optical properties of

metal nanoparticles. It describes the changes in the visible spectra based on interparticle distance between particles and compares them to calculated results.

Theoretical Considerations

Many groups have performed calculations that model the optical properties of nanoparticles⁷. Predicted Visible spectra exist for noble metal nanoparticles, such as gold and silver⁸, as well as semiconductor nanoparticles. The calculated spectra are generally derived from bulk dielectric functions of the composing material and particle diameter. These calculations can be quite involved when considering multiple particle interactions. Small, simple systems of particles with small aggregation numbers have been modeled.

Much of the theoretical work to study nanoparticles is based on Mie Theory. This allows for an analytical solution of the optical extinction spectra for single, isolated spheres. These calculations can be quite involved due to the large number of parameters in each equation^{7,8,9}. These adjustable parameters include the wavelength of radiation, dielectric functions of the metal, refractive indices of the metal and surrounding medium, structure, size, and shape of the particles as well as the density, orientation and distribution of the particles in the medium. Essentially, these Mie Theory calculations are based on the electrodynamic responses of the nanoparticles.

Since Mie Theory is used most often lets consider some of the calculations. The collective extinction^{9a} of the nanoparticles is given by:

$$C_{\text{ext}} = 2\pi/k^2 \sum (2n+1) \text{Re} (a_n + b_n) \quad (4.1)$$

The electric and magnetic scattering functions are a_n and b_n , respectively. Equation 4.1 tells us that the collective optical response can be divided into separate electronic, a_n , magnetic, b_n , and independent multi-pole contributions. In other words, the entire electromagnetic components for each particle must be summed to obtain an exact solution. In order to calculate interactions between particles, we must first look at individual particles.

The solutions to the above equations can show the electrodynamic response of an isolated sphere of arbitrary size and material is equivalent to that of a coherent collection of point multipoles with individual polarizabilities^{9a}. Each mode in the optical response is a collective response of the individual dipoles in a particle, i.e. each atom in the nanoparticle has its own polarizability and contributes to the collective optical property. The exact dipole polarizability is then described using the Quasi-static limit. This gives the Clausius-Mossotti expression of particle polarizability:

$$\alpha_1 = [4\pi\epsilon^0 a^3/3L_x][\epsilon_m - \epsilon_h/\epsilon_m + \kappa\epsilon_h] \quad (4.2)$$

Where ϵ^0 is the permittivity in a vacuum, a is a radius of a particle, L_x is the depolarization factor, ϵ_m and ϵ_h are the complex dielectric constants of the particle and surrounding medium and κ is the screening factor. This expression holds true for an isolated sphere of any size and material. It also accounts for the properties as a function of surrounding medium. This expression states mathematically that the dipole response of the particles, surface plasmon resonance, will shift to longer

wavelengths and broaden with increasing particle size. This is predicted by equation 4.2. Increasing the diameter, a , causes an increase in polarizability and a red shift in the visible spectra.

After studying the properties of single particles, the interactions between particles can be explored. The Maxwell-Garnett theory allows us to modify Mie Theory to look at interacting particles¹⁰. Maxwell-Garnett theory makes two important approximations. First, Individual polarizable entities are treated as dipoles. This means that only one collective dipole per particle is considered. Second, only dipole-dipole interactions are considered. First the dipole for each individual particle must be identified. These are usually expressed as:

$$\mu_n = \alpha_n \epsilon_h E_n \quad (4.3)$$

where μ_n is the dipole of the particle, α_n is its polarizability, ϵ_h is the dielectric constant of the metal and E_n is the electromagnetic field. The subscript n denotes the specific particle in question. The electric field felt by the particle is given as:

$$E_1 = E + g(\mu_2/\epsilon_h \epsilon^0 d_{12}^3) \quad (4.4)$$

a function of the applied field, E , the shape of the particle, g , the dipole moment of the adjacent particle, μ_2 , and the distance between them, d . Next, the average polarizability must be found for the two interacting particles by averaging the dipole expressions..

$$\frac{1}{2}(\mu_n + \mu_n) = \frac{1}{2}(\epsilon_h)(\alpha_1 E_1 + \alpha_2 E_2) = \epsilon_h \langle \alpha \rangle E \quad (4.5)$$

Solving for the average polarizability of each structure gives:

$$\langle \alpha \rangle = \frac{1}{2} [\{\alpha_1(1 + g(\alpha_2/d_{12}^3)) + \alpha_2(1 + g(\alpha_1/d_{12}^3))\}/(1 - g^2(\alpha_1\alpha_2/d_{12}^6))] \quad (4.6)$$

To apply the Maxwell-Garnett theory, equation 4.2 can be modified to fit two interacting particles since we now know the average polarizability. The particle radius is changed to reflect a shape factor between particles. The screening factor and depolarization constants are substituted to reflect the changes based on interparticle interactions. The spectra can also be fit for a change in incident angles with respect to polarizability¹⁰.

Another method, The Discrete Dipole Approximation (DDA) uses advanced electrodynamic theory to describe the spectra¹¹. In DDA, each particle is broken down into a finite array of individual dipoles derived from the bulk dielectric constants for the given metal¹¹. Each array is then subject to the perturbation of an electromagnetic field and a resultant spectrum is obtained. DDA is a more rigorous treatment of the above-described theories. While the different methods yield slightly different results, they have one idea in common: increased interaction with decreased interparticle distance.

The optical properties of coupled nanoparticles show some general trends that are described using calculations⁷⁻¹¹. The first trend is due to the number of particles in an aggregate. As the number of particles is increased, the plasmon resonance will red shift. When particles are organized into more linear chains, the plasmon resonance will divide into two resonances. One is along the short axis, called the transverse mode. The energy of this mode rarely changes, as the diameter of particles is constant. The longitudinal mode is along the long axis. This will decrease in energy as the number of particles increases. This shift in

spectra is caused by interactions between particles. The coupling causes the chain of particles to act like a long rod. The ability to experimentally observe these two modes in a solution of coupled nanoparticles is difficult due to a lack of suitable assembly methods for controlling the interactions of nanoparticles.

Many of the optical coupling experiments presented in the literature have shown that large 2D and 3D aggregates produce very noticeable changes in the optical spectra¹². Some examples have been shown using DNA based aggregation and interface films of particles to produce changes¹³ large enough to be seen with the naked eye. Optical coupling has also been observed using particles aligned in a template¹⁴. These changes are all based on the interaction of tens to hundreds of nanoparticles. Interactions of small numbers (less than 5) of nanoparticles has not been shown until now.

Using the method previously described methods, small assemblies of nanoparticles with controlled aggregation number were investigated for electromagnetic coupling. This chapter describes the synthesis of Au and Ag nanoparticle arrays and the changes in the visible spectra. The changes in the visible spectra are then compared to theoretical calculated spectra.

Experimental

Nanoparticle arrays were synthesized using previously described methods¹⁵. Briefly, A stoichiometric amount of a highly dilute linker solution was slowly titrated into a diluted nanoparticle solution. Absorbance spectra of these solutions

were then taken vs. time. UV-VIS spectra were obtained on a Hewlett-Packard 8453 diode array using a computer interface run by HP software.

Results and Discussion-Au Nanoparticle Arrays

The first attempt to identify optical coupling was from adding the particles to the linker solution. This resulted in a broadband absorbance (Figure 4.1) at approximately 600 nm. This result is characteristic of large aggregation, similar to the results of Mirkin's DNA sensor¹³. This was confirmed by TEM groups of particles with large aggregation numbers. The large amount of aggregation was overcome by changing the order of assembly. Adding the linker to the particle solution increases the chance of one linker per particle and complete binding of particles to each reactive group on the linker. The absorbance spectra showed no changes over a period of several hours. These spectra can be seen in Figure 4.2. When the PA7-2 di-thiol linker was added to the particle solution changes were observed. The wavelength of the plasmon resonance red-shifted about 10nm from the initial value of 525nm and an overall increase in absorbance intensity was observed. This is shown in Figure 4.3. In contrast, the tetrahedral linker, PA4-4, showed no change in absorbance.

These results are consistent with calculations found in the literature. Kriebig's group has modeled small aggregates of nanoparticles using Mie Theory^{7b}. Spectral changes for 10nm Au particle aggregates are summarized in Figure 4.4. A dimer of particles would result in a red shift of 10nm. This is assigned to the

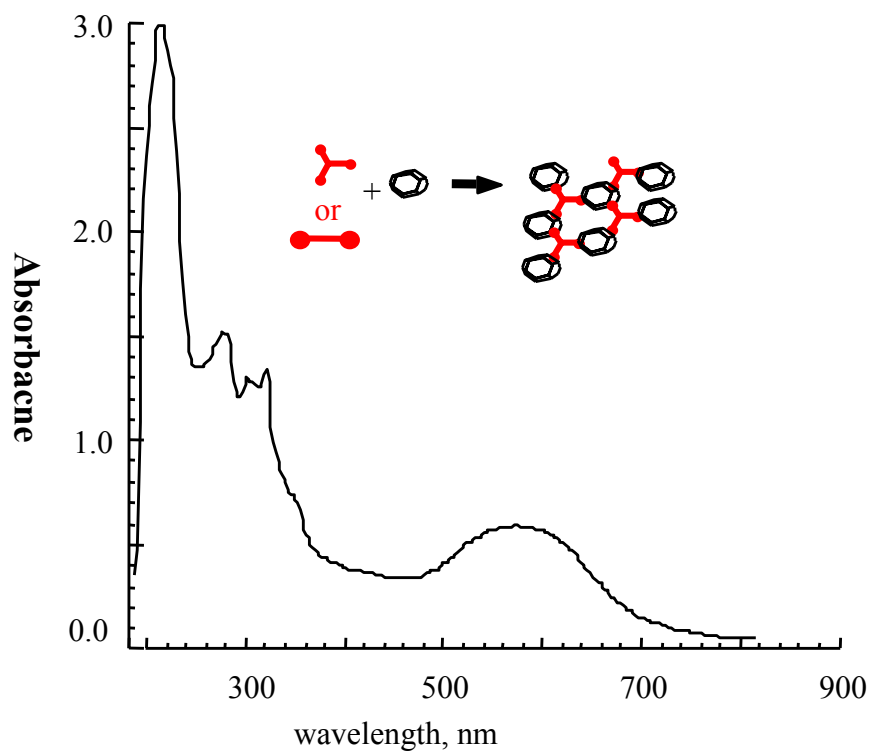


Figure 4.1. Resultant UV-Vis absorbance spectra obtained by adding 10nm Au nanoparticle sol to linker solution. Broad absorbance at 600nm is characteristic of irreversible aggregation.

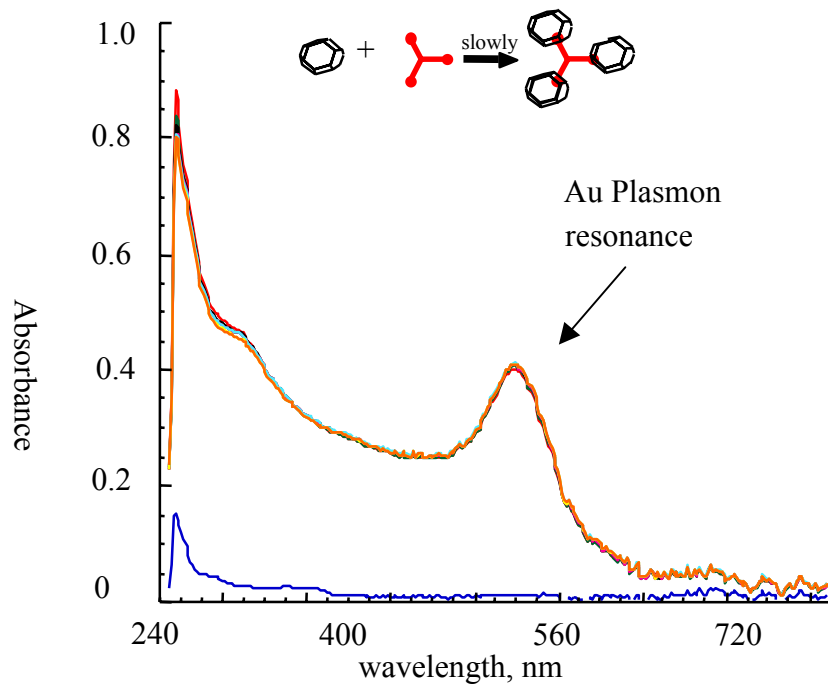


Figure 4.2. UV-Vis absorbance spectra for 10nm Au trimers versus time. No change in the surface plasmon resonance is observed over 1 hour.

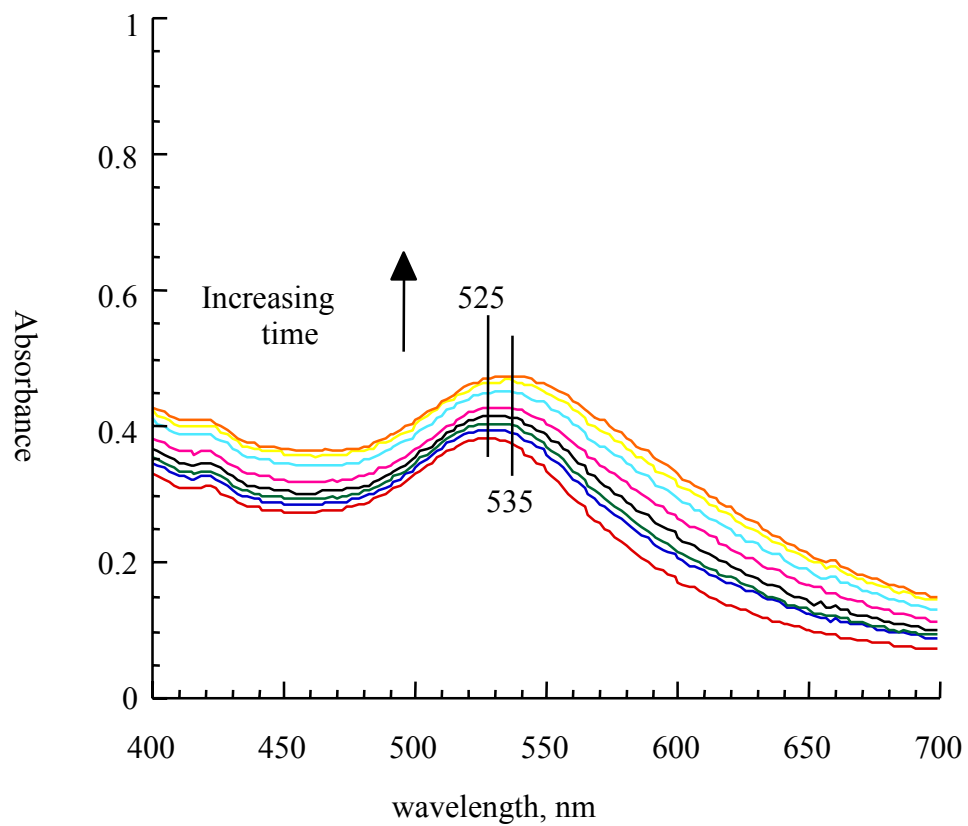
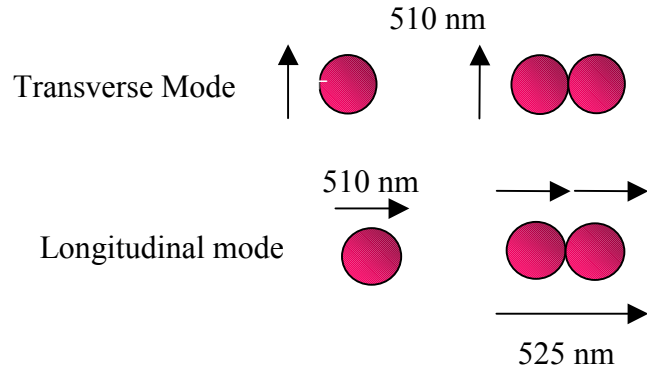


Figure 4.3. UV-Vis absorbance spectra for 10 nm gold dimer arrays versus time. Overall time change is 40 min.

Linear Particle Arrays



Non-linear particle arrays

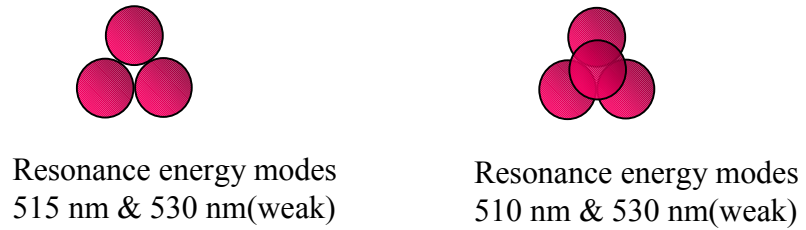


Figure 4.4. Calculated extinction maxima for Au nanoparticle arrays as a function of symmetry. Adapted from M. Quinten; U. Kreibig, *Surf. Sci.* **1986**, 172, 557

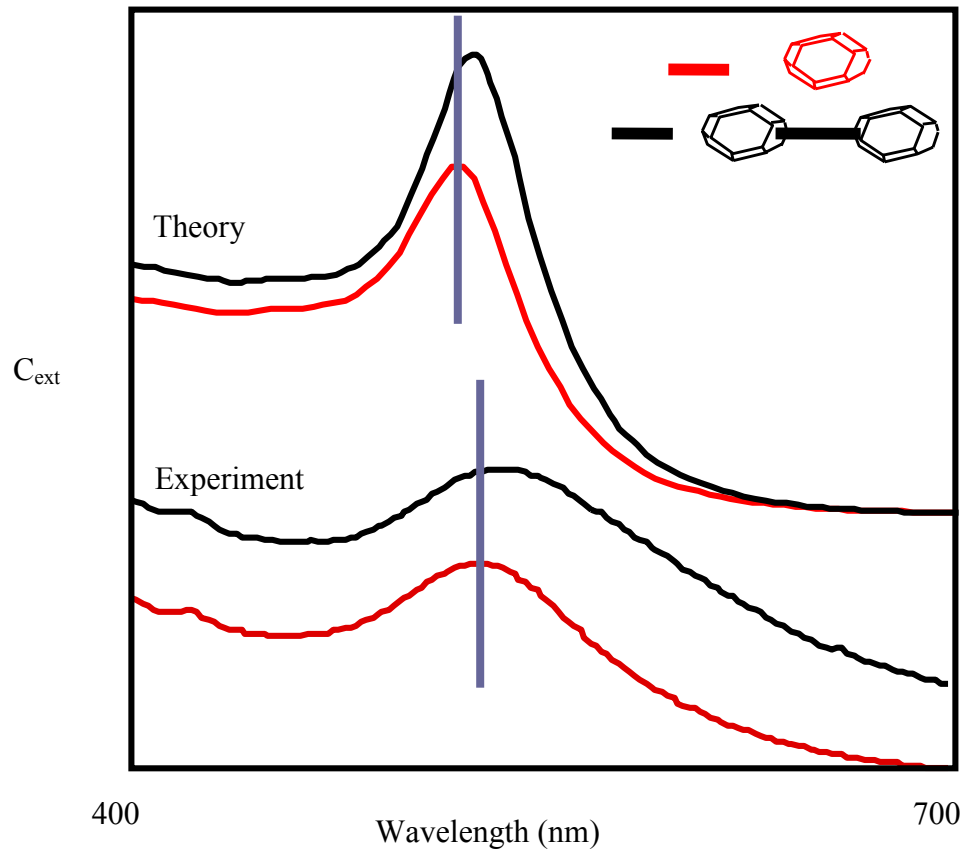


Figure 4.5. Calculated extinction spectra compared to experimental observations for Au dimers(black) and monomers(red). Calculated spectra were modified to account for concentration and orientation averaging. Courtesy CA Foss, Jr.

longitudinal mode between the particles. This mode also accompanies an increase in intensity. Colby Foss performed additional calculations taking into account the concentration of our particle arrays and the rotational average in solution. These spectra are seen in Figure 4.5. The calculated spectra show an increase in absorbance and a red shift of approximately 10nm for the dimers. These two example calculations are in good agreement with our experimental observations.

Due to their symmetry, the particle interactions of non-linear aggregates are not explained by a true transverse or longitudinal mode. These are now described by resonance energy modes. The high-energy mode is the excitement of a single particle in the aggregate. The absorbance of the coupled particles is described by multiple combined energy modes that are individually very weak. In order for an absorbance to be seen for this mode, each of these combined transitions must be excited simultaneously. Due to sample orientation in solution, the probability of this occurring is most likely very low. We believe that this mode is not observed due to the low concentration of desired aggregates in solution and the relative strength of these transitions. Again the calculated spectra were in good agreement with our experimental results.

Results and Discussion-Ag Nanoparticle Arrays

Electromagnetic coupling as a function of interparticle distance was investigated using 30nm Ag particles. Silver dimers were synthesized using dithiol phenyl acetylene linkers. The 9, 7, and 3 unit chains with lengths of ca.

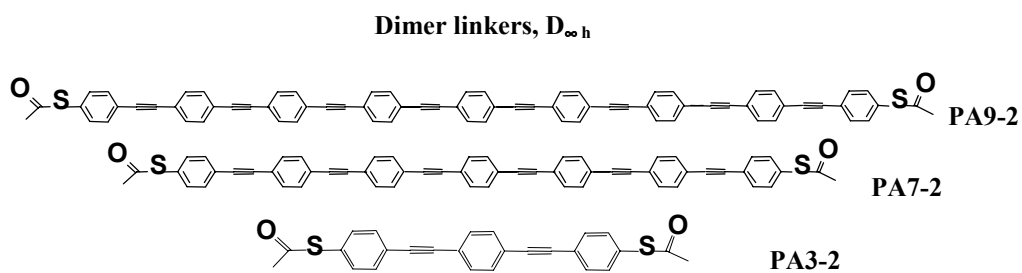


Figure 4.6. Molecular structures of phenylacetylene linkers used to template Ag dimers.

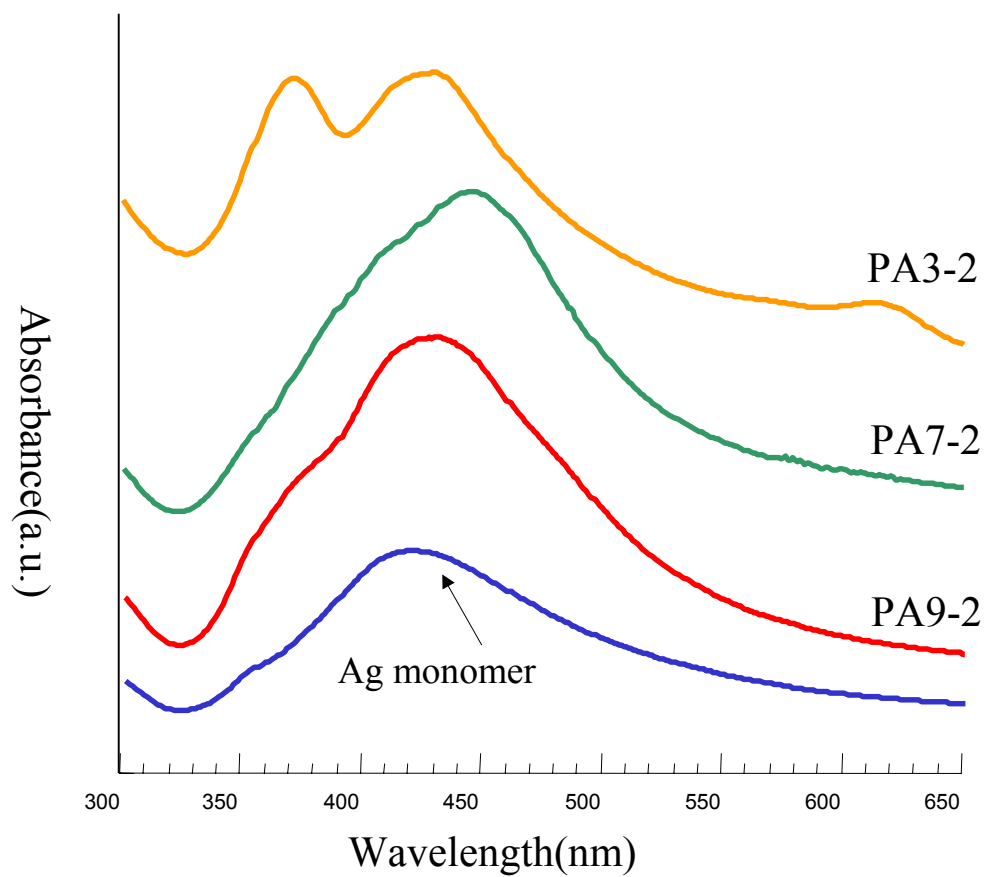


Figure 4.7. UV-Vis spectra of 30nm Ag dimers as a function of interparticle separation. Scans are offset for clarity.

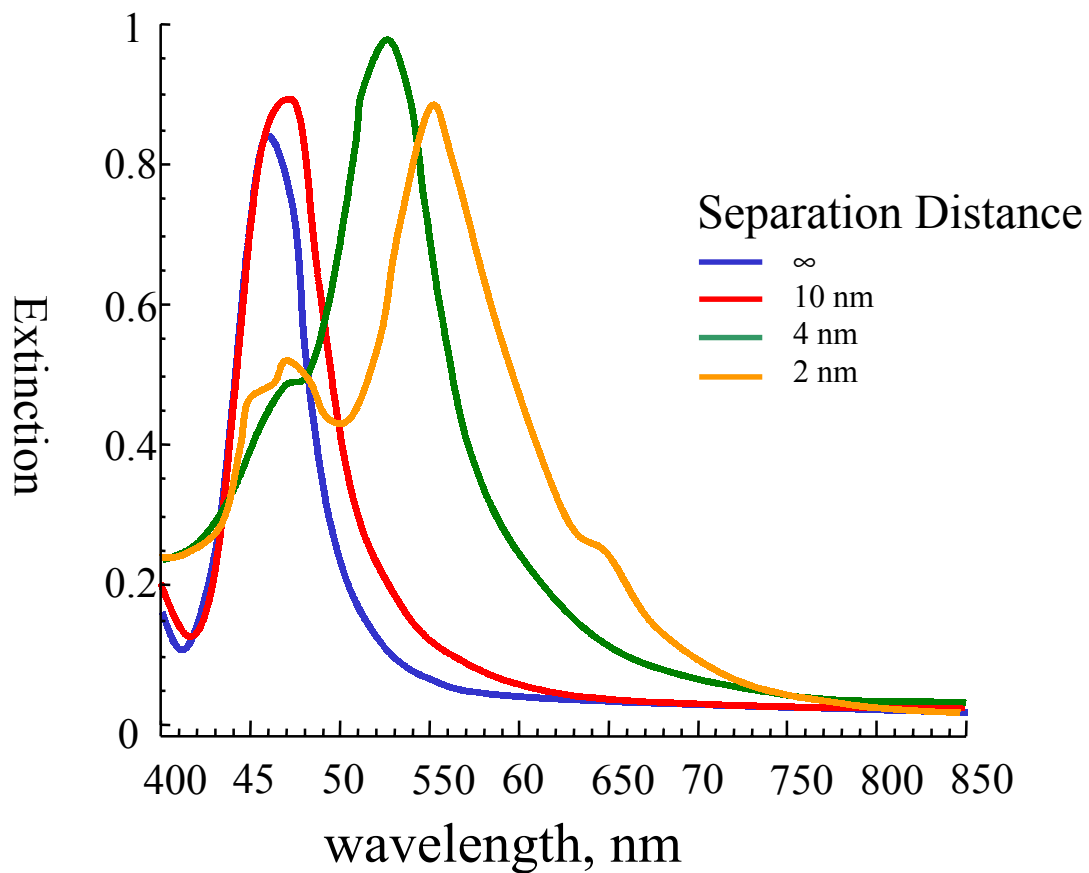


Figure 4.8. Calculated extinction spectra for 60nm Ag dimers as a function of separation distance. Adapted from Jensen, T.; Kelley, L.; Lazarides, A.; Schatz, G. *J. Cluster Science*. **1999**, 10, 295

7.2nm, 5.6nm, 2.4nm respectively, were used to bridge the particles. These structures are shown in Figure 4.6. UV-Vis spectra were taken as a function of bridge length.

Figure 4.7 shows the experimental spectra. Each curve was offset on the Y-axis for clarity. The lower trace is the Ag monomer solution. It has a maximum absorbance at 420 nm that corresponds to the surface plasmon resonance (SPR). When the particles are linked using the PA9-2, dithiol linker, the spectrum changes. There is a 15nm red-shift as well as an increase in absorbance. Decreasing the interparticle distance using the PA7-2 linker yields a greater red-shift of 40nm. Further decrease in interparticle distance using PA3-2 shows some new features in the spectra. The initial band does not change much from the previous linker. However, a high energy peak is now present at 370nm and a low energy shoulder is present at 630nm. This shows remarkable evidence for interparticle coupling.

A trend is observed when comparing the spectra as distance is decreased. The plasmon absorbance shifts to lower energy as the particle distance is decreased. This is consistent with explanations of the coupling dipole between the particles. The closer the particles are together, the more interparticle coupling between them. As the coupling is increased, the energy of the longitudinal mode is decreased. The high-energy shoulder at 370nm is attributed to a high-order quadrupole moment. This has been seen in 2D films of Ag particles¹⁶. The large intensity of this band has not been explained.

Calculations have been performed that illustrate these points. George Schatz's group at Northwestern University published calculations and spectra that model the interaction of 60nm Ag nanoparticles as a function of interparticle distance¹¹. An adaptation of this data is shown in figure 4.8. The calculated spectra show an absorbance of about 375nm for the Ag monomers. When the interparticle distance is decreased to 30nm the plasmon absorbance red-shifts about 10nm. Interparticle distance is decreased to 4nm the SPR shifts approximately 60nm to 450 and there is a high-energy shoulder emerging below 400nm. This becomes more pronounced as the interparticle distance is decreased to 2nm. The plasmon resonance is now red shifted 130nm to 500nm. A high-energy band is now present at 390nm and a low energy shoulder is present at 610nm. These calculations are very similar to our experimental results, however there are some differences.

Some of the differences between the experimental and calculated spectra arise from the parameters of the experiment. The calculations are performed on 60nm Ag particles. Our experiments were done with 30nm nanoparticles. The spectra is very size dependent. In addition, the amount of coupling between particles is a function of the particle diameter and distance. If a 60nm Ag nanoparticle and 30nm Ag nanoparticles are both held at the same fixed distance, the 60nm particles would couple more strongly. Additional changes in the spectra could arise from the optical properties of nanoparticles are based on dielectric

constants of the surrounding solvent. The calculations were performed for particles in a vacuum. Our experimental spectra were performed in water.

Conclusions

We have shown that nanoparticles couple electromagnetically. This coupling is based on the dipole interactions between particles and is observed by monitoring changes in the visible spectroscopy. The magnitude of the coupling is shown to be distance dependent and is consistent with theoretical calculations. However, while the coupling can be observed between nanoparticles, the results are subtle, especially for the Au structures. It is also noted that changes in symmetry do not show changes in the linear optical properties. A more sensitive method for investigating the interparticle coupling based on symmetry would be nonlinear optical techniques.

Chapter Four References

1. a) G. Schmid ed. "Clusters and Colloids" New York, VCH, **1994** b) G. Schmid *Chem. Rev.* **1992**, 92, 1709 and references therein c) **Pt**- TS Ahmadi, ZL Wang, TC Green, A Henglein, MA El-Sayed, *Science* **1996**, 272, 1924 d) **Pd**- MT Reetz, W. Heilbig, *J. Am. Chem. Soc.*, **1994**, 116, 740 e) **Au** -M Brust, M Walker, D Bethell, JJ Schriffin, RJ Whyman, *Chem Comm.* **1994**, 801; RW Murray, et al *J. Am. Chem. Soc.*, **1996**, 118, 4212 f) **Ag**-PC Ohara, DV Leff, JR Heath, WM Gelbert, *Phys. Rev. Lett.* **1995**, 75, 3466 g) RL Whetten, *Adv. Mat.* **1996**, 8, 428 h) RP Andres, *Science* **1996**, 273, 1690 i) KC Graber, *Langmuir*, **1996**, 12, 2353 k) PC Lee, D Meisel, *J. Phys. Chem.* **1982**, 86, 3391
2. DL Feldheim, KC Graber, MJ Natan, TE Mallouk, *J. Am. Chem. Soc.* **1996**, 118, 7640
3. a) RP Andres, T Bein, M Dorogi, S Feng, JI Henderson, CP Kubiak, W Mahoney, RG Osifchin, R Reifengerger, *Science*, **1996**, 272, 1323 b) LC Brousseau, III, Q Zhao, DASchultz, DL Feldheim, *J. Am. Chem. Soc.* **1998** 120 (30), 7645
4. a) S Nie, SR Emory, *Science*, 1997, 275, 1102; b) SR Emory, S Nie, *J. Phys. Chem. B* **1998**, 102, 493; c) SR Emory, WE Haskins, S Nie, *J. Am. Chem. Soc.* **1998**, 120, 8009; c) AM Michaels, M Nirmal, LE Brus, *J. Am. Chem. Soc* **1999**, 121, 9932;
5. DL Feldheim, CD Keating, *Chem. Soc. Rev.* **1998**, 27, 1
6. RG Freeman, KC Graber, KJ Allison, RM Bright, JA Davis, AP Guthrie, MB Hommer, MA Jackson, PC Smith, DG Walter, MJ Natan, *Science*, **1995**, 267, 1629; b) RG Freeman, KC Graber, KJ Allison, RM Bright, JA Davis, AP Guthrie, MB Hommer, MA Jackson, PC Smith, DG Walter, MJ Natan, *J. Am. Chem. Soc.* **1996**, 119, 1148
7. a) M.L. Sandrock, CA Foss, Jr. *J. Phys. Chem. B* **1999**, 103, 11398 and references therein; b) M Quinten, U Kreibig, *Surface Science* **1986**, 172, 557; c) U. Kreibig, A. Hilger, H. Hovel, M. Quinten, "Optical Properties of Free and Embedded Metal Clusters: Recent Results" in *Large Clusters of Atoms and Molecules*, TP Martin(Ed.) Kluwer, Netherlands, **1996**, 475-493
8. a) EJ Zeman, GC Schatz, *J. Phys. Chem.* **1987**, 91, 634; b) WH Yang, GC Schatz, RP Van Duyne, *J. Chem Phys.* **1995**, 103(5) 869

9. a) WT Doyle, *Phys. Rev. B.* **1989**, 39(14)9852 b) BT Draine, J. Goodman, *The Astrophysical Journal*, **1993**, 405, 685 c) EM Purcell, CR Pennypacker, *The Astrophysical Journal*, **1973**, 186, 705
10. ML Sandrock, CA Foss, Jr, *J. Phys. Chem. B.* **1999**, 103, 11398
11. T. Jensen, L. Kelley, A. Lazarides, G.C. Schatz, *J. Cluster Science*, **1999**, 10,(2)295
12. a) CA Mirkin, RL Letsinger, RC Mucic, Jj Storhoff, *Nature*, **1996**, 382, 607; b) H Wohltjen, AW Snow, *Anal. Chem.* **1998**, 70, 256
13. a) JJ Shiang, JR Heath, CP Collier, RJSaykelly, *J. Phys. Chem. B* **1998**, 102, 3425; b) KV Sarathy, PJ Thomas, GV Kulkarni, CNR Rao, *J. Phys. Chem. B* **1999**, 103, 399 c) CB Murray, CR Kagen, MG Bawendi, *Science*, **1996**, 270, 1335; d) CP Collier, RP Saykelly, JJ Schiang, SE Henrich, JR Heath, *Science*, **1997**, 277, 1978
14. CR Martin, *Acc. Chem. Res.* **1995**, 28, 61
15. a) LC Brousseau, III, JP Novak, SM Marinakos, DL Feldheim, *Adv. Mat.* **1999**, 11, 447; b) JP Novak, DL Feldheim, *J. Am. Chem. Soc.*, **2000**, 122, 3979
16. G. Chumanov, K Sokolov, T.M. Cotton, *J. Phys. Chem.* **1996**, 100, 5166

Chapter 5
NLO Properties of Symmetrically Controlled
Nanoparticle Arrays

Introduction

The study of metal nanoparticles has created an exciting new area of chemistry. Taking advantage of new assembly methods, nanoparticles have shown potential in medical screening¹, chemical sensing², and single electron devices³. Nanoparticles also show potential for use in optical data transfer using a photonic device⁴. One of the desirable characteristics for good optical data transfer is nonlinear optical (NLO) response. To achieve good NLO response, the system must maximize the second or third harmonic generation.

To maximize the non-linear response requires several conditions to be met. First the system must be highly polarizable. This makes donor-acceptor type molecules with large dipoles and nanoparticles with highly polarizable free electrons good candidates. The system must also fit a non-centrosymmetric point-group, in other words it must lack a center of inversion. In order for large NLO signals to be achieved, there must be long range order in the system. This requires that all the dipoles align in the same direction to give off a coherent signal. It is difficult to orient molecules in the same direction due to the dipoles alternate alignment in order to minimize energy. Hyper-Rayleigh Scattering (HRS) is a NLO technique that overcomes these alignment requirements. It measures non-coherent light scattered by the chromophores in solution. This chapter will describe the use of Hyper Rayleigh Scattering to obtain the nonlinear optical (NLO) response of ordered nanoparticle arrays in solution.

Background

Many molecular systems have shown large second harmonic generation (SHG) response. These molecular systems usually have large dipole moments due to donor-acceptor groups at opposite ends of the molecule. Polarizing these molecules by light or an electric field allows them to meet the symmetry requirements. Attaching the molecule to a surface can also break the symmetry. Information from SHG experiments has been used to show surface symmetry⁵, surface charge⁶, adsorbate coverage⁷, and adsorbate orientation⁸.

The magnitude of the frequency-doubled light is directly related to the dipole moment of the molecule, described above, and the strength of the electric field. Looking at the equation for asymmetric polarizability⁹ we can see this.

$$\mu_i = \mu_o + \alpha E + (\beta/2)E^2 + (\gamma/6)E^3 + \dots \quad (5.1)$$

Where μ_i is the total polarizability, μ_o is the dipole moment and E is the applied electric field. The coefficients, α , β , γ ... describe the magnitude of the higher order terms that contribute to the total polarizability. This expression (equation 5.1) describes the molecular polarization. When looking at SHG the magnitude of β is the important contributing factor. It describes the magnitude of second order light that is generated from the incident field. Since we are concerned with optical properties, E can be described as some electromagnetic wave. For example, $E = E_o \cos(\omega t)$. If the magnitude of E is large enough, then the higher order terms will start to make contributions to the total polarization. Of course, whether they are

visible or not depends also on the magnitude of the hyper-polarizability coefficients such as β .

The second hyper-polarizability coefficient, β , is based on several factors. One factor is the polarizability of the system. A molecule can have increased polarizability by increasing conjugation between the donor and acceptor groups. β can also be increased by using a highly polarizable metal nanoparticle. These nanoparticles have free electrons, which are highly polarizable. With extinction coefficients on the order of 10^7 - 10^9 , nanoparticles are highly efficient at interacting with light compared to molecular systems. Increasing the electromagnetic coupling between adjacent nanoparticles can increase this polarizability, possibly leading to an increase in β .

Another aspect for the magnitude of β is the symmetry requirement. NLO requires a non-centrosymmetric system. This requirement is derived from group theory. While there will not be a lengthy discussion here, decreasing symmetry adds terms to matrices that are fundamental in deriving NLO equations. As more symmetry terms contribute to these sums, the magnitude of the coefficients in the NLO expression increases. Experimentally, this break in symmetry can be built into a molecule by having a donor-acceptor group on each end or placing the molecule on a medium interface. These interfaces are usually liquid-liquid or liquid-solid. When discussing nanoparticles the task of decreasing symmetry is slightly more difficult. We are able to assemble geometrically controlled nanoparticle arrays as discussed in Chapter 3 of this dissertation. The two factors

of polarizability and lack of symmetry make our gold nanoparticle arrays, trimers specifically, ideal candidates for NLO measurements.

One of the drawbacks for making NLO measurements are the experimental requirements. In order to measure β , special experimental conditions must be met^{9,10}. Molecules must be orientated so that all the donor and acceptor ends are coherently aligned. This can be performed by aligning the molecule in an electric field. This describes Electric Field Induced Second Harmonic Influence (EFISHG). These techniques usually apply to systems attached to a surface or embedded in a polymer matrix. The field can also serve to polarize the molecule, which can increase SHG. Since our nanoparticle arrays are solution based, another technique must be employed.

Hyper Rayleigh Scattering (HRS)¹⁰ is a NLO technique that measures incoherently scattered light from a solution. HRS has been shown to allow for a direct measurement of the second hyper-polarizability factor, β , using the relationship

$$I(2\omega) = G \langle N_s \beta_s^2 + N_a \beta_a^2 \rangle I^2(\omega) e^{(-N_a \alpha l)} \quad (5.2)$$

Where $I(2\omega)$ is the intensity of the frequency double light, $I(\omega)$ is the intensity of the incident light, G is a collection efficiency term taking into account the local field corrections, N is the number density in particles/cm³, β is the first hyper-polarizability coefficient, α is the absorption cross section at 2ω , and l is the pathlength of the cell. The exponential term accounts for absorbance losses of the scattered light.

One of the drawbacks of HRS is an incredibly small signal compared to other NLO techniques¹¹. Despite the difficulties involved with measuring such small signals, HRS does not have the size limitation associated with other NLO techniques. Many systems that do not normally allow for NLO measurements can be investigated using HRS. Many of these systems consist of an analyte dissolved in a solvent, such as charge transfer salts and metal nanoparticles. One reason is the lack of symmetry created by the analyte/solvent interface. HRS has been used to investigate silica particles¹² and molecular adsorbates on silver nanoparticles. HRS has also been used to investigate the hyper-polarizability of nanoparticles^{12d}.

It has been shown that Au nanoparticles have large NLO response. HRS was used to determine that Au nanoparticle sols have HRS responses that exceed semiconductor solutions by factors of at least 10^5 . There were several reasons to describe this observation. One is the effect of resonance enhancement. The nanoparticle absorb light around 520nm. The transition that occurs is due to the Surface Plasmon Resonance. Since the SPR occurs near the frequency doubled output (532 nm) from a 1064 nm laser, the particle is in a state of resonance enhancement. This resonant enhancement has also been seen in other spectroscopy, such as Surface Enhanced Raman Spectroscopy (SERS)¹³, where the interaction between the analyte and light are increased. Another explanation for the observation of large HRS signals was the lack of symmetry in the individual particles. Nanoparticles are spherical, however they are not perfect spheres. The individual particles have various facets and vertices that reduce the symmetry.

These structural features act like individual scatterers, each contributing to the overall NLO response of the particle. The same experiments noted that reducing the symmetry salt aggregation increased the HRS signals. While these results show that symmetry is important, its true role was not addressed. This can be addressed using symmetry-controlled arrays of nanoparticles.

Experimental

Nanoparticle arrays were synthesized according to previously published methods¹⁴. This is described in detail in Chapter 3 of this dissertation. All measurements were taken in four-sided quartz cuvettes. Each cuvette was washed in *Aqua Regia* then rinsed thoroughly prior to sample addition. The solutions were diluted (1:5, 1:10, 1:15, 1:20, 1:25) and HRS measurements were taken using a setup similar to the cartoon shown in **Figure 5.1**. The general experimental setup

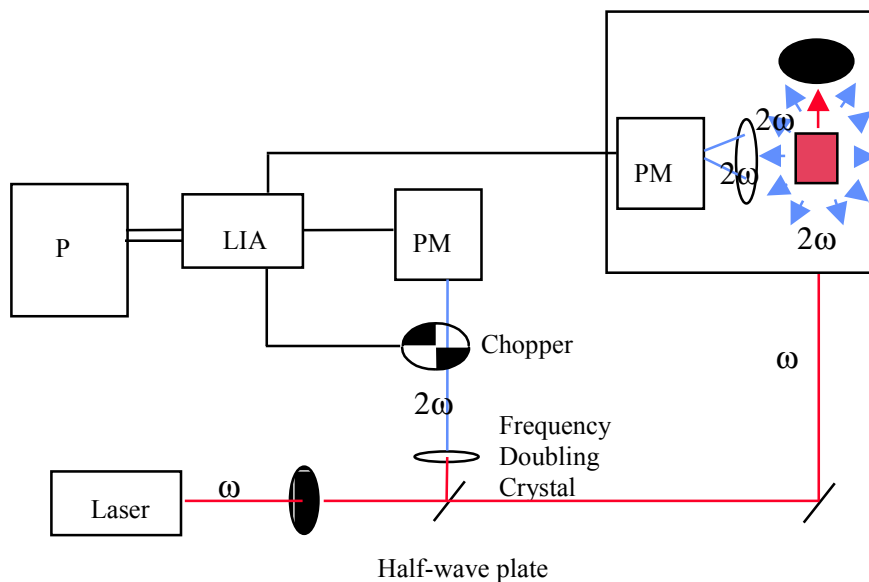


Figure 5.1. Hyper Rayleigh Scattering Apparatus.

is as follows. A laser is focused on a sample through a series of mirrors and lenses. An inline beam-splitter is used before the sample to create a reference path and a sample path. The reference line is passed through a tuned frequency doubling crystal. This line is then focused on a PMT through a chopper. The laser light in the sample path passes through a chopper and is focused on the sample. The scattered light is collected through a collection lens and focused on the PMT through the appropriate filter. A digital lock-in amplifier is used to keep track of the reference and sample path. The data is collected using a PC and analyzed with LabView™.

Each sample of the Au nanoparticles was analyzed by the following experiments. A power dependence curve was taken to verify HRS signals and not emission. This was done by collecting the intensity of the frequency doubled scattered light compared to the intensity of the incident light. The power from the laser was passed through an iris to change the intensity. As a control experiment this procedure was repeated with the detector set below, at and above 2ω . The fact that no signal was observed except when the detector was set at 2ω reveals that the signal is HRS and not emission. Concentration plots were obtained by measuring $I_{2\omega}$ of each dilution with constant I_ω . Polarization experiments were performed by inserting a polarizer between the sample and the detector. $I_{2\omega}$ vs. I_ω data was taken by rotating the polarizer from 0° to 360° in 20° increments. The resulting data points were fit to $y = a (\cos^2 (x-c)) + b^{11}$; where y is $I_{2\omega}/I_\omega^2$, x is the angle, and a and b are the curve's maxima and minima respectively.

Experiments were performed exciting at 1064 nm using a Q-switched Nd/YAG laser. This was the on-resonance experiment where the scattered light is in resonance with the plasmon absorbance of the nanoparticles (532 nm). The laser was operated with 300ps pulse at 10Hz.

Results and Discussion

Considering the symmetry of the nanoparticle arrays one would expect the monomers, dimers, trimers, and tetramers to scatter at different intensities²⁰. This was confirmed by overlaying samples on a scattering plot, Figure 5.2. The intensity of the frequency doubled light is graphed versus the intensity of the incident light squared. This is in accordance with equation 5.2. This plot clearly shows that the trimers scatter more frequency double light than either the

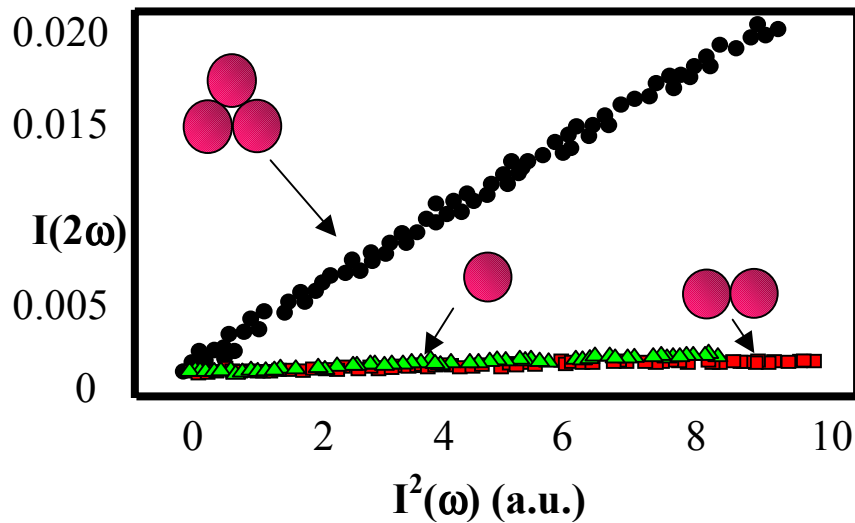


Figure 5.2. Hyper-Rayleigh Scattering Plot. As expected non-centrosymmetric structures scatter more intensely than centrosymmetric structures.

monomers or the dimers. This is an expected result as the trimers lack a center of inversion. This non-centrosymmetric structure is the simplest that can be made from a solution of Au nanoparticles. It is interesting to note that the monomers and dimers scatter at approximately the same intensity.

While the results in Figure 5.2 show a qualitative representation of the data,

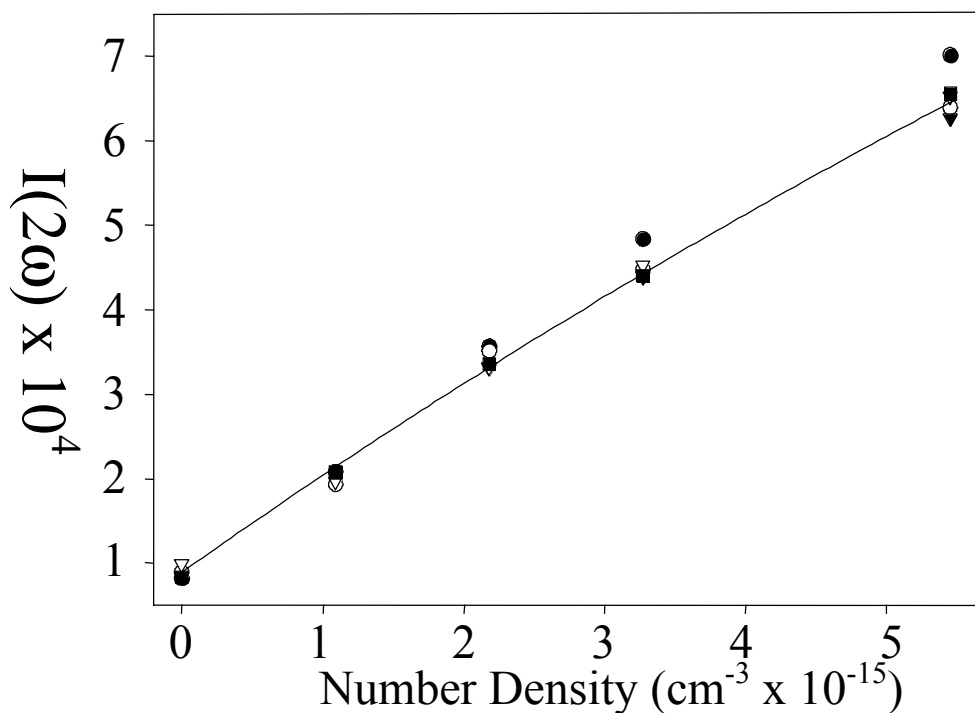


Figure 5.3. Concentration Dependence plot for nanoparticle arrays. First hyperpolarizability values can be calculated from the slope of the fit line. Linear dependence indicates HRS signal.

Figure 5.3 allows for the quantitation of β . Figure 5.3 shows a concentration dependence plot. The intensity of the frequency doubled scattered light is graphed vs. concentration. Since the intensity of the incident frequency is held constant, β

can be calculated according to equation 5.2. The factors that are needed for this

Table 5.1. Selected first hyperpolarizability values for gold nanoparticle arrays

Array; Calc.	Au—Au Distance (nm)	$\beta/(x 10^{-30} \text{ esu})$	Depolarization Ratio (β_v/β_h)
Tetramer	PA4-4; 2.9	4300	1.4±0.2
Trimers	PA2-3; 1.4	3800	1.57±0.07
	PA3-3; 2.8	2700	1.64±0.02
Dimers	PA1-2; 0.6	1300	1.9±0.2
	PA7-2; 6.2	1100	1.9±0.2
	PA9-2; 7.0	1530	2.1±0.1
	Monomer; n/a	1800	1.84±0.04

calculation are the absorbance at the scattering frequency and the first hyperpolarizability and concentration of the solvent. Calculated values for β for different samples are shown in Table 5.1. Values were calculated based on sample composition. The β values of the monomers were calculated and then other values were corrected based on TEM derived concentrations. These correction were performed using Equation 5.1. Summing contributions for each component in solution. For example, once the β value for just the monomer are known then β_{dimers} can be determined if the concentration of dimers is known. Values reported are normalized to the number of atoms in each particle.

The experimental values for β confirm our earlier hypothesis. The first hyper-polarizability values are higher for the tetramers and trimers than the monomers and dimers. The values for the tetramers and trimers are 4300 and 3800 [$\times 10^{-30}$ esu] respectively. As can also be seen, the values for the monomers and dimers are non-zero. In fact, they are quite large themselves. This is consistent with earlier findings by Vance and co-workers^{12D} where the individual non-spherical nature of the particles is causing large NLO activity. The individual particles are not precise spheres due to the vertices and facets in the shape. The values of the monomers and dimers are similar. This suggests that the dimers are scattering as individual particles and not two electromagnetically coupled particles in an array.

Interparticle distance was also investigated. Listed in Table 5.1 are the β values based on linker length. Linkers are shown in Figure 5.4. There appears to be some distance dependence on the NLO response. The longer trimer, PA3-3, appears to have a smaller β value than PA2-3. The values are 3800 and 2700 ($\times 10^{-30}$ esu) respectively. This leads us to believe that the interparticle coupling is decreasing with an increase in interparticle distance. This is similar to the linear optical experiments discussed in Chapter 4 of this document. Because there are only two samples we have not yet confirmed this observation. Additional lengths need to be investigated. When we look at the β values of the dimers as a function of distance we again see there is no real correlation. It appears that the dimers are

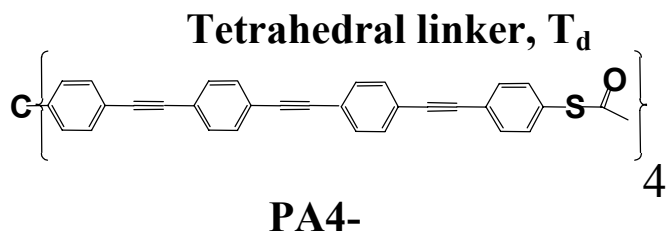
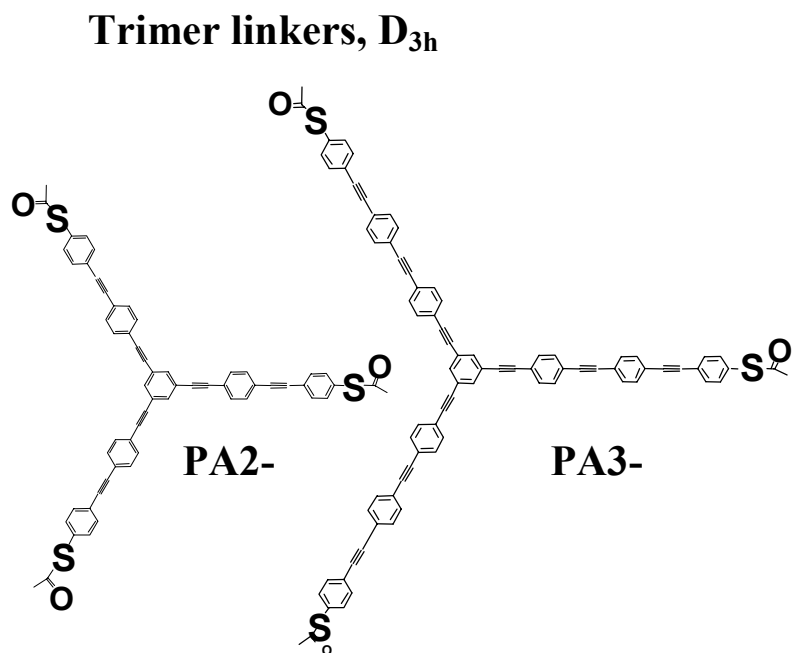
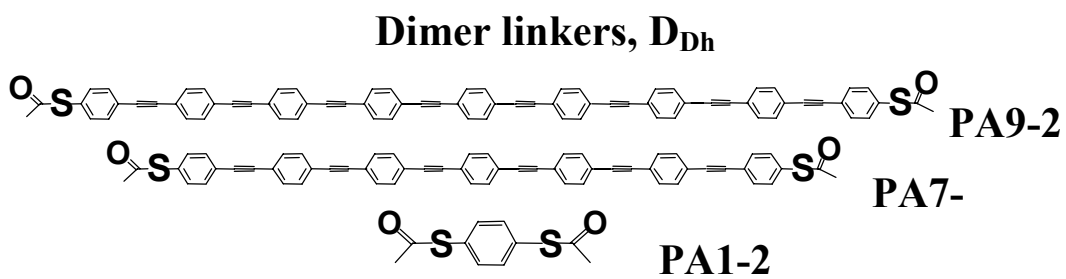


Figure 5.4. Molecular structures of Phenylacetylene bridges used in HRS experiments.

acting as single particles, not as electromagnetically coupled arrays. This is in contrast to the linear optical experiments discussed in Chapter 4.

One of the drawbacks in determining the symmetry of the particle arrays is the number of available techniques. Transmission Electron Microscopy (TEM) is the method of choice for determining the symmetry of these arrays. It has been argued that these particles are not templated by the linker and they have organized themselves during the grid preparation. We now have spectroscopic evidence to the contrary.

One experiment that can be performed with HRS is a depolarization ratio. This experiment uses a polarizer between to scattering sample and the collection optics. The intensity of the frequency-doubled light is graphed versus polarization angle. A fit to this line using the function $y = a (\cos^2 (x-c)) + b$ allows for β to be calculated in the horizontal and vertical plane polarized light. The ratio of these two values gives what is described as a depolarization ratio. Depolarization ratios are listed in Table 2. We would expect a depolarization ratio of 1.5¹⁵ for the non-centrosymmetric tetramers and trimers. As you can see this is very close to the experimental values of 1.4, 1.57, and 1.64. The value of 1.5 indicates that these groups are scattering with an octupolar moment. This moment clearly is a function of symmetry and also the electromagnetic coupling between the particles²¹. The fact that the value increases slightly with an increase in interparticle distance, for the trimers, indicates that there is a decrease in interparticle coupling. This is the

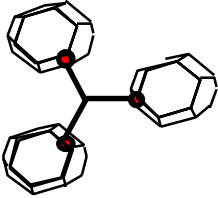
same conclusion that can be derived from looking at the first hyper-polarizability values.

The monomers and dimers should scatter like individual particles. Their interaction with light has been described by an oscillating surface plasmon resonance, often considered a dipole. A theoretical depolarization ratio of 2.0 indicates a dipole scattering mechanism. The values of 1.9, 1.9, and 2.1 are experimentally close to the calculated value.

The depolarization ratios clearly confirm the symmetry. They also show evidence that the particles are electromagnetically coupled. These results confirm the electromagnetic coupling in the linear optical spectra that is demonstrated with the dimer nanoparticle arrays. In contrast, the symmetry of the tetramers and trimers do not lend themselves to be studied for electromagnetic coupling using a linear optical technique. The enhanced sensitivity of the NLO experiments confirms that these lower symmetry nanoparticle arrays are indeed coupling electromagnetically.

It has been reported that the monomer nanoparticle sols have incredibly large first hyper-polarizabilities^{12D}. We have shown that decreasing the symmetry of these nanoparticle arrays while retaining interparticle coupling can increase the NLO activity. Table 5.2 shows some β values of some other well-known NLO chromophores. These β values can be reported in different ways. They can be normalized to the molecule (or particle) or normalized due to the number of atoms in the molecule (or particle). The later is done as each atom has contributions to

Table 5.2. Comparison of first-hyperpolarizability values of nanoparticle trimers to well known molecular chromophores

Chromophore	β^2 /molecule ($\times 10^{-30}$ esu)	β^2 /atom ($\times 10^{-30}$)
H ₂ O	0.3	0.032
PN	900	4
Push-Pull Porphyrin	2.5×10^7	3000
	3.5×10^{16}	5.8×10^6

the overall scattering of the molecule. As water is the solvent in these experiments, it is shown to have an incredibly small β value. When the dipole moment is increased and conjugation is added the value increase quite significantly, as for p-nitroaniline. PNA¹⁶ is routinely used as a calibration standard for these NLO apparatus. When the conjugation is greatly improved by using a porphyrin-based core¹⁷, the β value jumps by orders of magnitude. When we consider the large dipole moment of the individual particle, the electromagnetic coupling between particles and the purposeful break in symmetry, whether considering a per molecule or per-atom basis, the first hyper-polarizability (β) value is several orders of magnitude larger than some of the best known NLO molecular chromophores.

Conclusion

The creation of Non Linear Optical materials takes some consideration. The polarizability, symmetry, and electronic structure of the system must be considered. We have demonstrated the design of non-centrosymmetric, electromagnetically coupled nanoparticle arrays. Hyper Rayleigh Scattering was used to confirm the existence of interparticle coupling in systems that did not show results by linear optical techniques. HRS was also used to confirm the symmetry of the Au nanoparticle arrays.

In addition to the Au nanoparticles, Ag nanoparticle arrays and mixed metal arrays could change this response. As described in a previous chapter of this dissertation, The Ag nanoparticles showed increased interaction as indicated using visible spectroscopy. These Ag or Au/Ag structures might show even further NLO activity.

Acknowledgements

I would like to thank Prof. JT Hupp and (previous) members of his research group at Northwestern University. Specifically, Dr. Fred Vance, Dr. Buford Lemon, and Mr. Bob Johnson for assisting in these experiments. This collaboration is ongoing and Ag nanoparticle arrays are currently being investigated.

Chapter Five References

1. JJ Storhoff, R Elghanian, R Mucic, CA Mirkin, RL Letsinger, *J. Am. Chem. Soc.* **1998**, 286, 101
2. WL Shaiu, DD Larson, J Vensneka, E Henderson, *Nuc. Acids Res.* **1993**, 21, 99
3. RP Andres, T Bein, M Dorogi, S Feng, JI Henderson, CP Kubiak, W Mahoney, RG Osifchin, R Reifengerger, *Science*, **1996**, 272, 1323.
4. S Foglia, L Suber, Mtighini, *Colloid Surface A* **2001**, 1, 177
5. a) DA Koos, GL Richmond, *J. Phys. Chem.* **1992**, 96, 3770, b) I Yagi, S Nakabayashi, K Uosaki. *J. Phys. Chem. B.* **1998**, 102, 2677
6. Z. Shi, J. Lipkowski, S. Mirwald, B. Pettinger, *J. Electronanal. Chem.* **1995**, 396, 115
7. C. Jung, O Dannenberger, Y Xu, M Buck, M. Grunze, *Langmuir*, **1998**, 14, 1103
8. D Yang, D bizzotto, J. Lipkowski, B. Pettinger, S. Mirwald. *J. Phys. Chem.* **1994**, 98, 7083
9. a) GD Stucky, SR Marder, JE Sohn, "Linear and Nonlinear Polarizability, A primer" in. *Materials for Nonlinear Optics, Chemical Considerations* , SR Marder, JE Sohn, GD Stucky, Ed, ACS Symposium, **1991**, ACS, Washington, DC
b) GU Bublitz, SG Boxer, *Ann. Rev. Phys. Chem.* **1997**, 48, 213 c) SR Marder, WE Torruellas, M Blanchard-Desee, V Ricci, GI Stegeman, S Gilmore, JL Breolas, J Li, GU Bublitz, SG Boxer, *Science*, **1997**, 276, 1233 d) JR Heath, *J. Phys. Chem. B.* **1998**, 102, 3425
10. a) K Clays, A. Persoons, L DeMaeyer, "Hyper Rayleigh Scattering in Solution" in *Modern Nonlinear Optics #3*, M Evans, S Kielich, Ed. **1994**, John Wiley, NY b) E Hendrickx, K Clays, A Persoons, *Acc. Chem. Res.* **1998**, 31, 675
c) P Keatz, DP Shelton, *Rev. Sci. Instrum.* **1996**, 67 (4), 1438

11. FW Vance, PhD Thesis, Northwestern University, **1999**
12. a) CK Johnson, JA Soper, *J. Phys. Chem.* **1989**, 93, 7281; b) K Clays, E Hendrickx, M Triest, A Persoons, *J. Mol. Liq.*, **1995**, 67, 133; c) AV Baranov, K Inoue, K Toba, A Yamanaka, VI Petrov, AV Federov, *Phys. Rev. B.: Condens. Matter B* **1996**, 53, R1721; d) FW Vance, BI Lemon, JT Hupp, *J. Phys. Chem. B* **1998**, 102, 10091; e) P Galletto, PF Brevet, HH Girault, R Antoine, M Broyer, *J. Phys. Chem. B*, **1999**, 103, 8706
13. M Moskovits, *Rev. Mod. Phys.* **1985**, 57 (3) 78318.
14. a) LC Brousseau, III, JP Novak, SM Marinakos, DL Feldheim, *Adv. Mat.* **1999**, 11, 447; b) JP Novak, DL Feldheim, *J. Am. Chem. Soc.*, **2000**, 122, 3979
15. a) FW Vance, JT Hupp, *J. Am. Chem. Soc.* **1999**, 121, 4047; b) J. Zyss, I. Ledoux, *Chem. Rev.* **1994**, 94, 77 c) J. Zyss, Cdhenaut, T Chauvan, I. Ledouz, *Chem Phys. Lett.* **1993**, 200, 409
16. P Kaatz, DP Shelton, *J. Chem. Phys.* **1996**, 105(10) 3918
17. SM LeCours, HW Guan, DG DiMagno, CH Wang, MJ Therien, *J. Am. Chem. Soc.* **1996**, 118, 1497

Chapter 6

**Single Molecule Surface Enhanced Raman Spectroscopy
of Organized Nanoparticle Arrays**

Introduction

The characterization of nanoscale materials is pushed to the limits as assembly processes are developed that involve single or tens of molecules. It is not possible to simply look at single molecules through a microscope to see how many are used to make up a material. Certain techniques can be adapted to obtain information of few molecules. The assembly of geometrically controlled metal nanoparticles using molecular templates has been demonstrated and described in the previous chapters. One question still remains. Is there one single linker molecule holding these nanoparticles together? This chapter will describe some spectroscopic experiments that suggest a single molecule is templating the geometrically controlled nanoparticle arrays.

Microscopy has led the way in single molecule investigations. The STM can be used to obtain molecular resolution¹. This ability to image on a molecular scale has brought great advances in surface science, especially with self-assembled monolayers¹. High Resolution Transmission Electron Microscopy (HRTEM) has also shown molecular resolution. It has been used to image individual atoms making up a nanoparticles² and carbon nanotubes³. These techniques have been invaluable in nanostructure characterization.

Spectroscopic measurements, on very few molecules, are more difficult to perform. This has been demonstrated using fluorescence⁴ and the STM⁵. Fluorescence of molecules has been detected at the single molecule level⁴. While this ultimate limit of detection can be done it is limited to fluorescent molecules.

There are very few molecules that fluoresce, even fewer that have efficiencies large enough to be detected on a single molecule level. Surface Enhanced Raman Spectroscopy (SERS) is another technique where, under the right conditions few molecules can be studied⁶. These experiments exceed the factor of a Raman signal, 10^5 - 10^6 , from a molecule adsorbed on a prepared metal surface⁷.

The SERS enhancement was first observed in 1974 when a group of scientists looked at the Raman spectrum of pyridine adsorbed on a silver electrode⁸. The electrode had been cycled through several electrochemical steps. They noticed that the signal strength from the adsorbed analyte was greatly increased. The initial thoughts were that the increased surface area from the redeposition of silver onto the electrode allowed more molecules to sit on the surface. This would in fact allow for a stronger signal. Several years later, Van Duyne⁹ and Creighton¹⁰ independently determined that the increase could not be accounted for by surface area alone. They determined that surface area alone could only account for one order of magnitude of signal enhancement. These early studies prompted increased activity in electrostatic and electromagnetic theory as the phenomena was linked to radiating multipoles near metal surfaces. The discovery of SERS helped explain other processes such as enhanced photoemissions of gratings¹¹, light emission from metal particles¹², and the excitations of surface plasmons¹³. The discovery was also responsible for physicists to explore the unfamiliar territory of electrochemistry¹⁴, charge transfer, and chemical adsorbates. The discovery of SERS was responsible for new momentum in the world of Surface Science.

Raman spectroscopy is defined by detecting the inelastic scattering of light by a molecule. Several types of Raman can be done with different results. Resonance Raman is performed by having the incident frequency in resonance with that of an absorbance frequency of the analyte. This typically gives enhancement factors of 10^2 - 10^4 . SERS increases this enhancement factor to 10^3 - 10^6 . SERS is Raman enhancement by electromagnetic resonances of a local field between a surface and an analyte. The local field is usually generated by the metallic surface. The effect is not usually seen on a flat polished surface due to the continuum of states. When surface roughness is added there can be intense localization of the energy which can cause enhancement. Any molecule in close proximity to the surface can “feel” the local field. This local field is dependent on the roughness factor and also the incident frequency of light. If the frequency is in resonance with the surface large local fields are created and enhancement factors of 10^6 - 10^8 have been reported.

The SERS enhancement can be demonstrated on many substrates¹⁴. These systems generally consist of many coupled microscopic metal domains. Several examples of these SERS-active substrates include the following. (1) Electrode surfaces that have been subject to oxidation-reduction cycles. This example has been described above. The best results are observed when the average size of the surface features is approximately 20 nm as determined by scanning electron microscopy (SEM). (2) Island films (5-20nm in diameter) of metal particles on glass or quartz substrates¹⁵ prepared by metal vapor deposition at cold

temperatures. Surface geometry is not controllable due to the limited surface mobility during deposition. (3) Lithographically prepared metal spheroids create regular periodic arrays of metal coated silicon surfaces¹⁶. The regularity allows for increased coupling between features. These types of systems can not be made in the small regime for large enhancements. (4) First observed in 1982, strong signals are observed from molecules adsorbed on surfaces of Metal nanoparticles¹⁷ in solution. These signals were further enhanced upon particle aggregation. More recent experiments using this technique are describe below.

The investigation of single molecule SERS has been led by the work of Emory and Nie at Indiana University. They were able to detect single molecules of Rhodamine dyes in aggregates of silver nanoparticles¹⁸. Their studies included particle aggregates of different shape, aggregation number and size. They were able to determine that small aggregates of particles containing two or three nanoparticles in a linear shape had the highest enhancement due to the collective resonance between particles. These “hot” particle aggregates yield a reported enhancement factor of 10^{14} - 10^{15} . Combing these large enhancements with the large extinction coefficients in molecules allows for single molecule SERS. Despite the novelty of the results, their experiments still raise questions.

The first area of question is the position of the dye molecule. The particles and the dye are mixed together. The particles are then aggregated with a salt solution causing the dye to be adsorbed onto the aggregates. The authors note that not all of the particle aggregates show the single molecule spectroscopy. This is

due to the dye molecule not being present at the precise position of the field of enhancement between particles. Additional questions arise due to the use of salt aggregation to create the particle aggregates. This method does not allow for the control of aggregation number or interparticle symmetry. A precise method for controlling nanoparticle symmetry and interparticle distance would eliminate questions regarding which particles were “hot.” Our method for using a linker molecule to precisely control the particle aggregation number and geometry may answer some questions regarding optimal particle geometry to maximize SERS enhancement.

Using a rigid linker to template nanoscale particle aggregates places the linker in only one place- directly between the nanoparticles¹⁹. Due the electrostatic repulsion forces between nanoparticles, the linker is forced to be at the shortest distance between particles. One interesting fact is the linker, directly between particles, is centered at the point of maximum electromagnetic interaction. If spectroscopic enhancement occurs based on dipole interactions or polarization transfer to the analyte from the surface of the particle, the linker is in optimal position for maximum enhancement.

Experimental

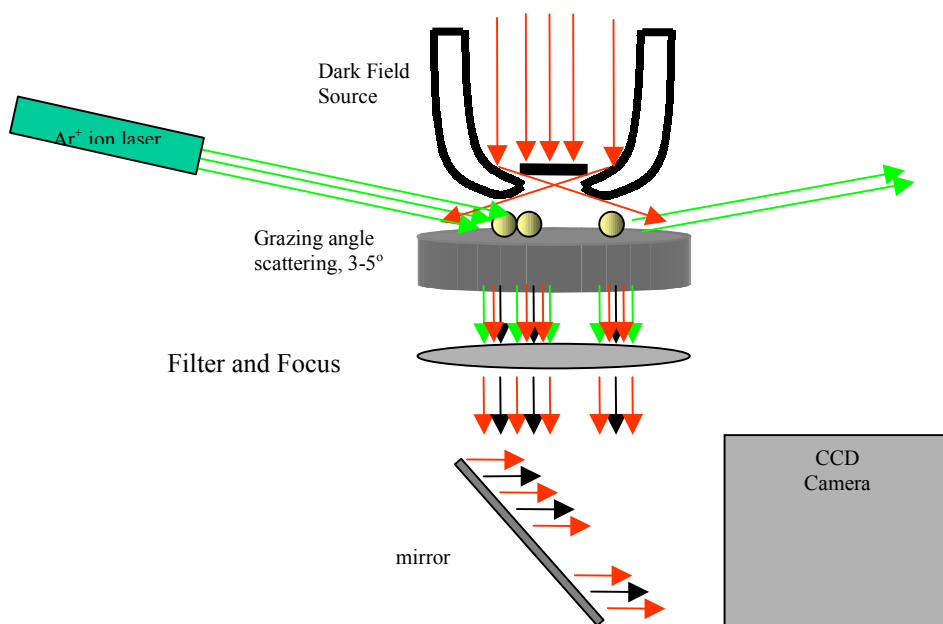
Nanoparticle aggregates were prepared using methods described in Chapter 3 of this dissertation. 30 nm Silver nanoparticle dimers were synthesized and characterized using UV-Vis and TEM¹⁹. SERS measurements were performed at Columbia University in the laboratory of Professor Louis E. Brus. The optical

samples were prepared by spincoating 2-5 drops of the linked nanoparticle solution onto a quartz slide covered with poly-lysine. AFM images were obtained using a Digital Instruments Bioscope III in tapping mode. The SERS experiments were performed using a grazing angle setup as shown in Scheme 1a²⁰. Briefly, a Coherent Innova 308 Ar⁺ (514.8nm, 35 mW) laser was focused onto the quartz slide with an angle of incidence of 3-5°. The scattered light was captured at 90° to the surface through a notch filter. The light was then reflected onto a cooled CCD liquid N₂ camera to obtain a SERS image. The SERS image shows which particles emit a Raman signal. The SERS image can be used to correlate with a dark-field image or AFM to identify which particle aggregate is showing Raman activity. A Raman spectra is obtained by focusing the scattered light through a slit, onto a grating and then to the CCD as shown in Scheme 1b. This separates the light through the slit into its component colors, which is converted into a Raman shift vs. Intensity plot. The sample holder is a stainless steel disk that can be rotated allowing for polarization studies.

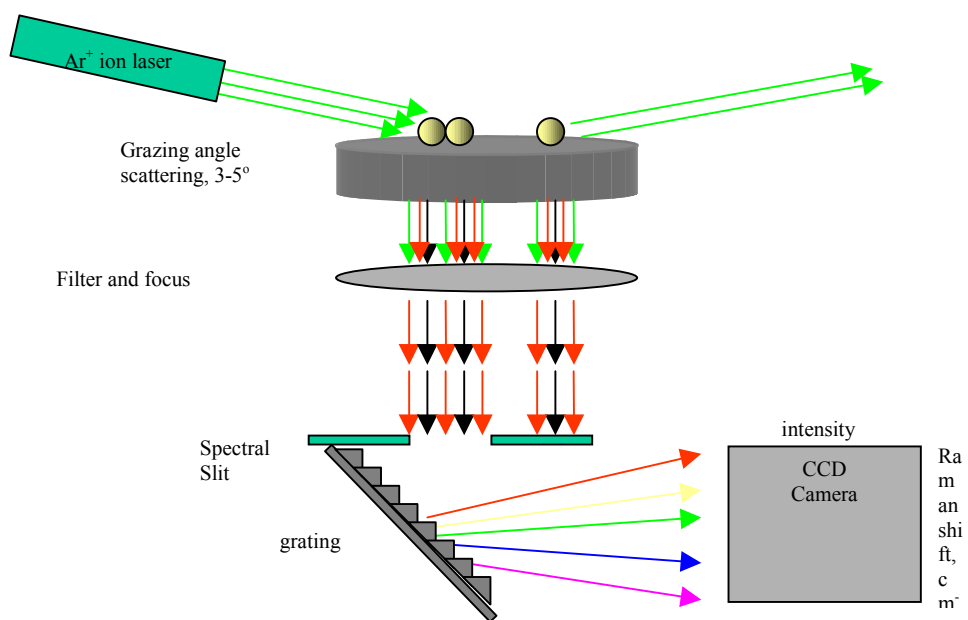
Results and Discussion

Figure 6.1 shows an AFM image of 30nm Ag dimers. This particular scan shows several dimers in the five-micron window. These are marked with arrows. The dimers resolve with a decrease in scan size. The height is consistent with the TEM derived diameters. The AFM image confirms the existence of Ag dimers

A. Collection of a Raman or Dark field image



B. Collecting Single Molecule SERS Spectra



Scheme 6.1. Apparatus for obtaining Dark-field or Raman images(A.) and Raman spectra(B.).

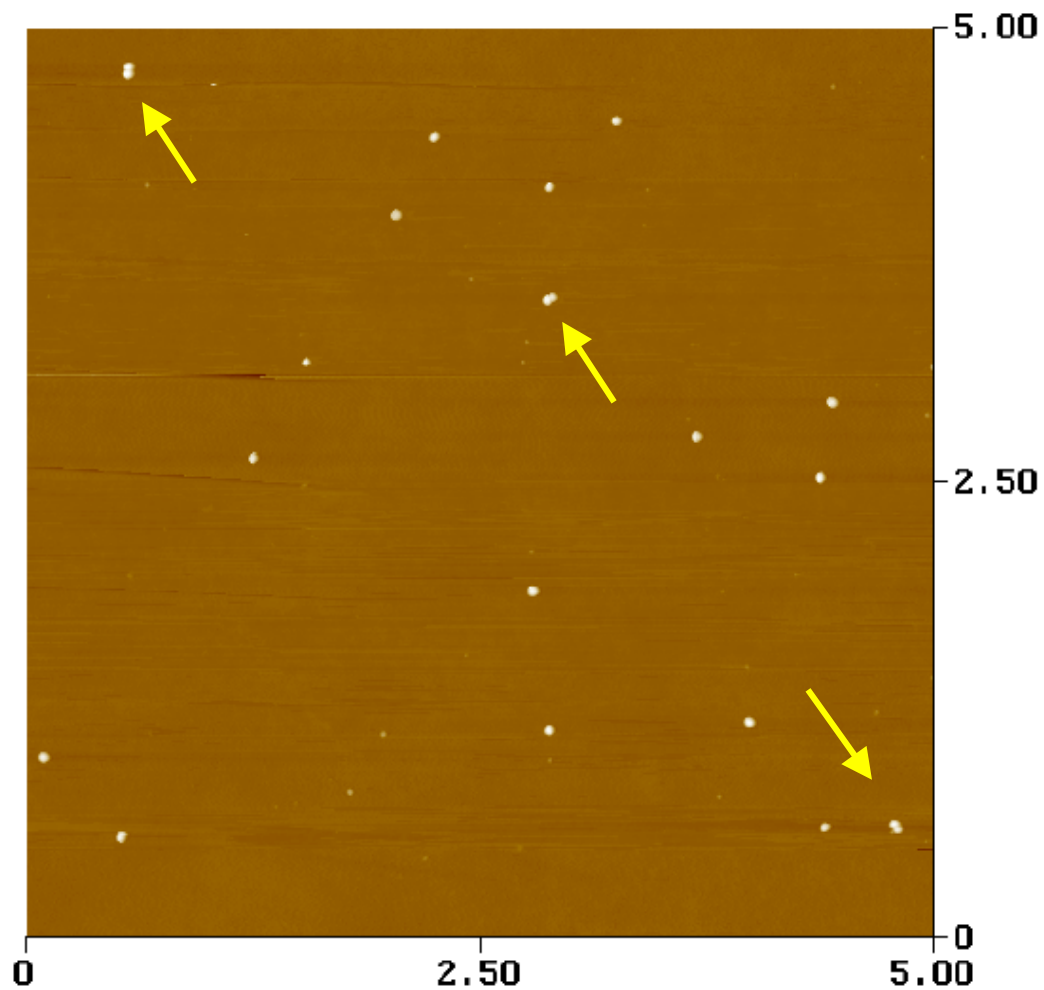


Figure 6.1. AFM image of 30nm Ag dimers on Quartz. Arrows indicate Ag dimers.

with no other aggregates present. This is also consistent with the TEM observations¹⁹ discussed in the previous chapters.

Figure 6.2 shows a corresponding Dark-field image and Raman image. Each image corresponds to an X-Y coordinate system with the colors (dark to light) representing and increase in the scattered light. Shown in the dark-field image (Figure 6.2a) are bright areas indicating strong Rayleigh scattering from nanoparticles. The Raman image (Figure 6.2b) is obtained from the same position

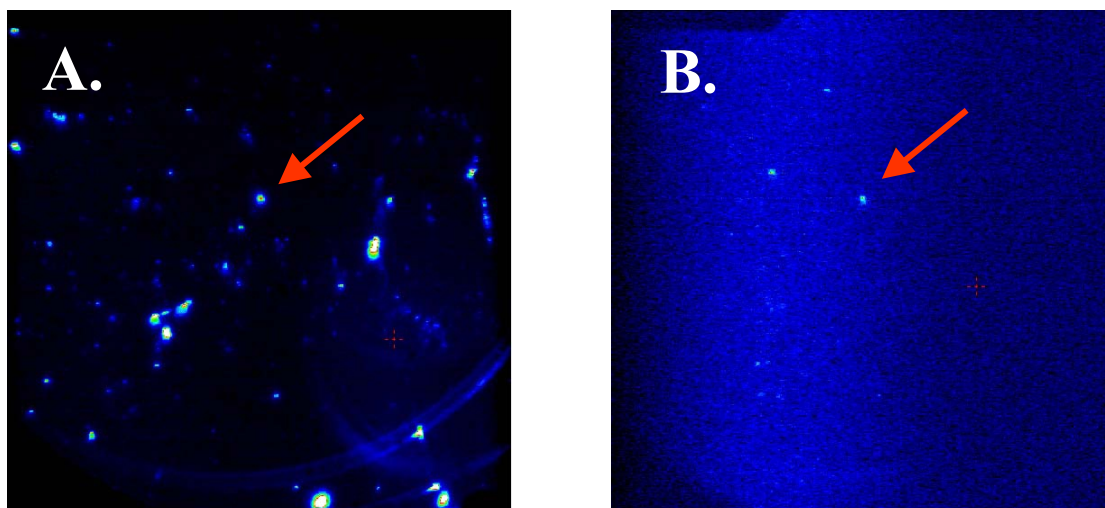


Figure 6.2 Dark-field(A.) and Raman (B.) images of 30 nm Ag nanoparticle dimers. Raman spectra(C.) from indicated particle.

on the sample slide. The two optical setups can be interchanged without disturbing the sample position. When looking at the Raman image we see that there are several areas that scatter Raman light. One particular spot is marked with an arrow. The same position is marked on the Dark-field image. This particular particle, while not being a strong Rayleigh scatterer, is a Raman scatterer. A Raman spectrum can be taken for single particle. The particle marked by the arrow is centered horizontally. The scattered light is then divided using the grating to produce a Raman spectrum. A scale can be set based on the Rayleigh line, which is the first bright line in the spectra. This is the light scattered from the laser light.

An example of a Raman spectrum is shown in Figure 6.3. We believe that this spectrum is obtained from a single linker molecule from a single nanoparticle dimer. The spectrum shows characteristic peaks that could be assigned to a phenyl-acetylene structure. There is a group of peaks centered around 1500 cm^{-1} that correspond to the aromatic C=C stretch and the alkyn stretch. The alkyn stretch is

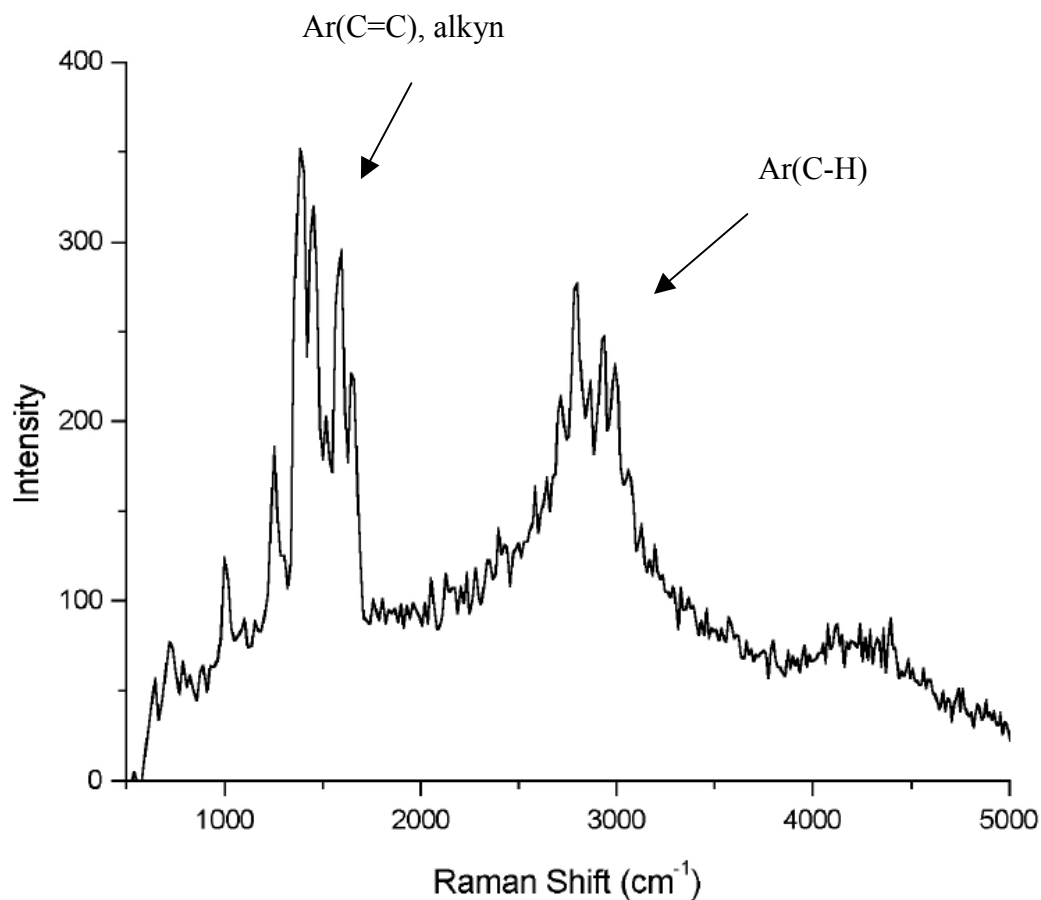


Figure 6.3. Single molecule SERS spectra for phenyl-ethynyl based nanoparticle linker. Marked peaks correspond with positions normally assigned for molecular functional groups.

normally seen at 2300cm^{-1} . The difference from position could easily arise from mechanical coupling due to conjugation²¹. The aromatic stretch is usually observed around 1600 cm^{-1} . There is also a set of peaks that are assigned to the aromatic C-H stretch. As expected, these peaks are visible just around 3000 cm^{-1} . The spectrum shows multiple peaks for each assignment. We believe that these are the multiple rings in the linker chain. In addition, there is the possibility for

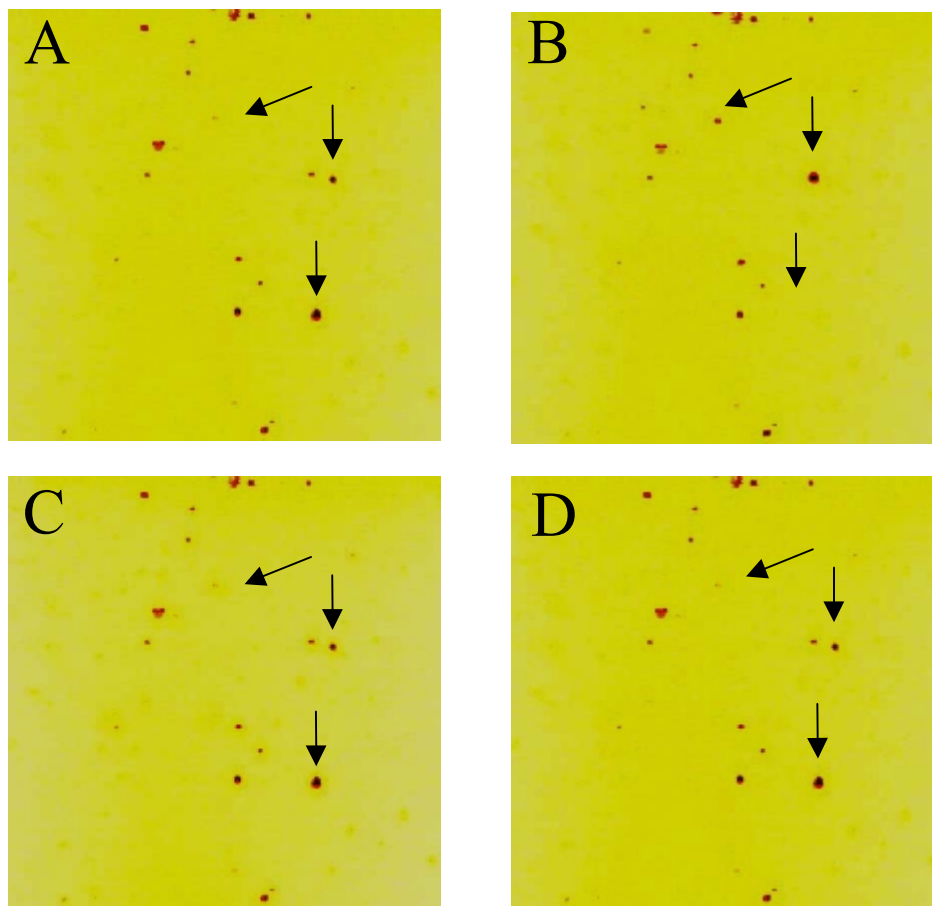


Figure 6.4. Concurrent SERS images of 30 nm Ag dimers. Scans are one second integration taken 10 seconds apart. Marked particles exhibit “blinking” associated with single molecule spectroscopy.

different modes to be present due to only a single molecule being excited. Each single molecule may respond to the incident radiation in a different way compared to a bulk measurement. While this spectrum is encouraging due to the existence of peaks that can be assigned to the linker, it does not indicate single molecule measurements.

To consider these measurements there are key experimental observations that lead us to determine that the signal is due to a single linker molecule. A single molecule spectroscopic experiment usually shows a signal that “blinks”. This

blinking is a signal that turns on and off with some time scale. Previously reported time scales are in the seconds to tens of seconds. Figure 6.4 shows a sequence of Raman images taken 10s apart with 1s integration times. Several particles are marked with arrows. Following image 6.4a through 6.4d we see that several Raman scatterers are on and turn themselves off or vice versa. Several other explanations for this blinking phenomenon have been suggested although it is not completely understood. The most widely accepted explanation for this is due to perturbation in the electronic states²².

In addition to the blinking of the particle aggregates, polarization experiments suggest that the Raman spectrum is from single molecules. As mentioned previously, the sample stage is comprised of a disk that can be rotated. The laser light is polarized parallel to the sample surface. Rotating the sample while simultaneously watching the dark-field image allowed the polarization experiments to be completed. Combined with the X-Y positioner, the sample can be rotated while keeping the individual particle aggregate in the same position. The results of these experiments can be seen in Figure 6.5, which shows the Raman spectra versus the sample angle. An aggregate was selected and its Raman spectrum was obtained. The sample was then rotated 90° and a Raman spectrum was taken. This procedure was repeated for the angles of 180°, 270° and 360°. The figure shows the spectral features are present for 0°. These peaks disappear when rotated 90°, then reappear at 180°. The features again disappear at 270° and do not

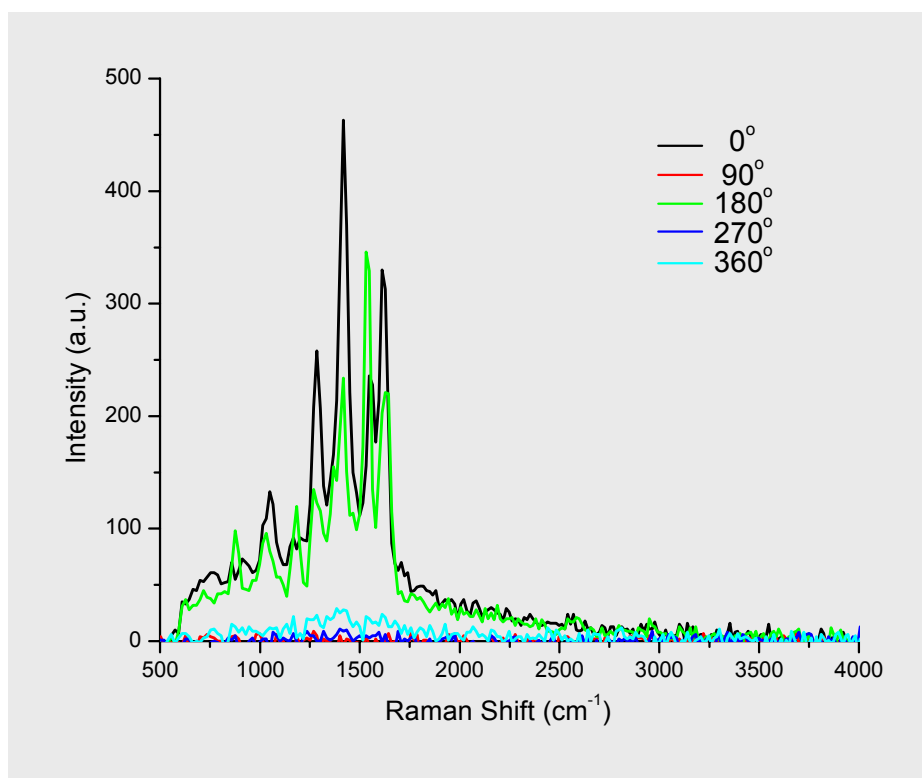


Figure 6.5. Polarization dependence on SERS spectra of 30 nm PA7-2 linked Ag dimers.

reappear at 360° . These experiments show the angle dependence on the Raman Spectra.

The explanation of this angle dependence is depicted in the cartoon in Figure 6.6. The only time a high field should exist directly between particles is when the aggregate is orientated parallel with the direction of light propagation. We believe this is the case when the spectrum is obtained at the initial angle. When the sample is rotated 90° , the aggregate is now orthogonal to the direction of light propagation. The linker is now located in a node of the electric field. In this position the linker can receive no enhancement from the particle and no Raman is observed because the signal is too weak. If there were multiple linkers present, A

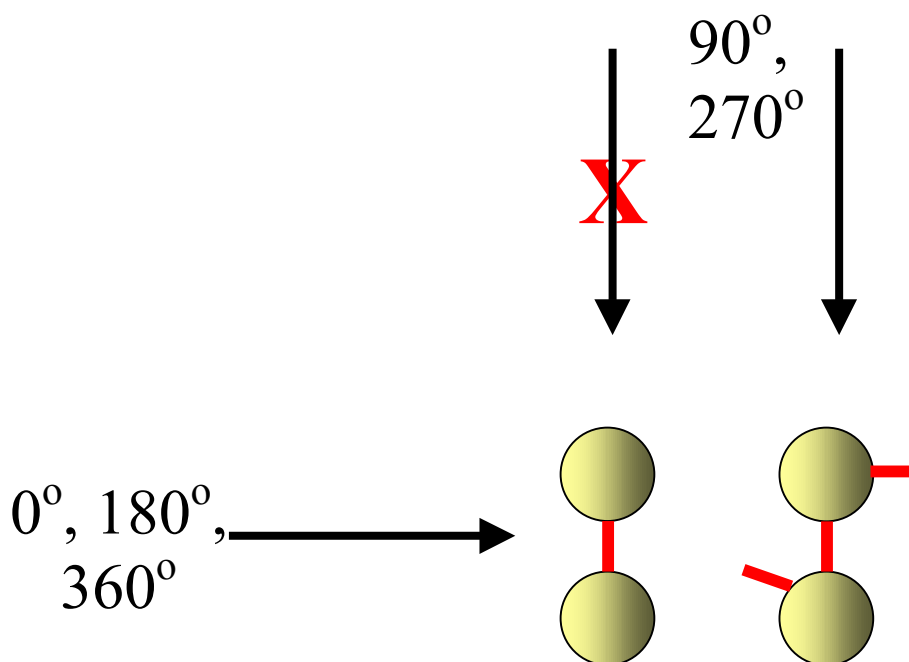


Figure 6.6. Cartoon of expected results from SERS polarization experiments. Enhanced field between particles allows linker spectra to be obtained when dimer is parallel (a.) to and not perpendicular (b.) to incident beam. Electric field lines between coupled particles show node for perpendicular orientation.

signal may be observed at this angle or at an angle between 0° and 90° . Rotating the sample 180° returns the particle to a position similar to the initial state.

Enhancement is now returned as the linker is directly in a position of greatest coupling between particles. This trend continues for the next angle, 270° . We would expect that the signal return at 360° , however this is not what is observed.

The signal does not return at 360° when the dimer is returned to its original position. We believe that this may due to photobleaching or the molecule “blinking” off. These experiments are time consuming and the sample stability in the laser is questioned at this point.

We must point out that the spectra obtained in the polarization experiments are difference than the spectrum shown in Figure 6.3. We reason that these spectra

are different due to the fact that we may be observing a single molecule. Others have shown that a different spectrum can be observed from different single molecules. This is generally attributed to the positioning of the molecule¹⁸ and surface selection rules¹⁵.

These experiments suggest that only one molecule is present between these particles. If there was more than one molecule present on the surface of the nanoparticles in the dimer, then a Raman signal should be detected at more than one angle. These experiments are also important when one considers that a phenyl acetylene linker should not be as strongly Raman active as some other dye molecules such as the Rhodamine dyes. With this in mind, the enhancement factors must be at their maximum to observe these signals. Collection efficiencies and enhancement factors have not yet been measured.

Conclusions

The experimental evidence suggests that there is only a single linking molecule templating the particles. The blinking in the Raman image is consistent with single molecule spectroscopy. In addition, the polarization experiments suggest that there is only one molecule templating these nanoparticles due to spectra matching the linker are not observed except at certain angles. We believe this is also excellent evidence for the strength of electromagnetic coupling between particles. The linker is placed in a position of maximum field strength, therefore largest enhancement in Raman signals.

These experiments are a good start to investigating the role of interparticle symmetry and interparticle distance on Raman scattering. As this dissertation is being written, additional samples are being measured. Ag trimers made with 10nm nanoparticles using the PA2-3 and PA3-3 linkers have been sent to our collaborators at Columbia University where the laser experiments are performed. Additional results are pending completion.

Acknowledgments

I would like to thank Prof. L. E. Brus's group at Columbia University. Especially his student Jiang Jiang for taking most of these measurements.

Chapter Six References

1. TA Jung, RR Schlittler, JK Gimzewski, *Nature*, **1997**, 386, 696; b) La Bumm, JJ Arnold, MT Cygan, TD Dunbar, TP Burgin, L Jones, DL Allara, JM Tour, PS Weiss, *Science*, **1996**, 271, 1705
2. G Schmid, *Chem. Rev.* **1992**, 92, 1709
3. AC Dillon, PA Parilla, JL Allaman, JD Perkins, MJ Heber, *Chem. Phys. Lett.* **2000**, 316, 13
4. . XH Xu, ES Yeung, *Science*, **1997**, 275, 1606
5. JET Anderson, JD Zhang, Q Chi, AG Hansen, JU Nielson, EP Friis, J Ustrop, A Buisen, H Jensen *Trends in Analytical Chem.* **1999**, 18, (11) 665
6. P. Hildebrandt, M Stockburger, *J. Phys. Chem.* **1984**, 88, 5935; b) K Kneipp, Y Wang, H Kneipp, I Itzkan, RR Dasari, MS Feld, *Phys. Rev. Lett.* **1996**, 76, 2444; c) K Kneipp, Y Wang, H Kneipp, LT perelman, I Itzkan, RR Dasari, MS Feld, *Phys. Rev. Lett.* **1997**, 78, 1667; d) K Kneipp, H Kneipp, B Kartha, R manoharan, G Deinum. I Itzkan, RR Dasari, MS Feld, *Phys. Rev. E.* **1998**, 57, R6281.
7. A Otto, I Mrozek, H Grabhorn, W Akemann, *J. Phys.: Condens. Mater.* **1992**, 4, 1143; b)G. Schatz, *Acc. Chem. Res.* **1984**, 17, 370; c) A Champion, *Chem. Soc. Rev.* **1998**, 4, 241
8. M Fleischmann, PJ Hendra, AJ McQuillan, , *Chem. Phys. Lett.* **1974**, 26, 163
9. DL Jeanmarie, RP Van Duyne, *J. Electro. Chem.* **1977**, 84, 1
10. MG Albrect, JA Creighton, *J. Am. Chem. Soc.* **1977**, 99, 5215
11. JG Endriz, *Appl. Phys. Lett.* **1974**, 25, 1961
12. J. Lambe, SL McCarthy, *Phys. Rev. Lett.* **1976**, 37, 923
13. RG Freeman, MB Hommer, KC Graber, MA Jackson, MJ Natan, *J. Phys. Chem.* **1996**, 100, 718
14. M Moskovits, *Rev. Mod. Phys.* **1985**, 57 (3) 783
15. M Moskovits, *Chem. Phys. Lett.* **1983**, 98, 498

16. PF Liao, JG Bergman, DS Chemla, A Wokaun, J Melngailis, AM Hawryluk, NP Economou, *Chem. Phys. Lett.* **1981**, 82, 355

17. JA Creighton, in *Surface Enhanced Raman Scattering*, edited by RK Chang, TE Furtak, Plenum, New York, 1982; b) H Abe, K Manzel, W Schulze, *J. Chem. Phys.* **1981**, 74, 792; c) K Manzel, W Schulze, M Moskovits, *Chem. Phys. Lett.* **1982**, 85, 183

18. a) S Nie, SR Emory, *Science*, **1997**, 275, 1102; b) SR Emory, S Nie, *J. Phys. Chem. B* **1998**, 102, 493; c) SR Emory, WE Haskins, S Nie, *J. Am. Chem. Soc.* **1998**, 120, 8009

19. JP Novak, DL Feldheim, *J. Am. Chem. Soc.* **2000**, 122, 3979

20. AM Michaels, M Nirmal, LE Brus, *J. Am. Chem. Soc.* **1999**, 121, 9932

21. JB Lambert, HF Shurvell, DA Lightner, R G Cooks, *Organic Spectral Spectroscopy*, Prentice-Hall, Inc. New Jersey, 1998

22. Accepted theory involves perturbation of electronic states. Small changes in single molecule levels are not averaged out by the existence of many molecules. Perturbation could be from vibrations in the electromagnetic field.

Chapter 7

Electronic Coupling in Nanoparticle Arrays

Introduction

The optical experiments described in the previous chapters give insight into electromagnetic coupling between metal nanoparticles. To probe electronic coupling between particles we must use electrochemical techniques. Electronic coupling between particles is different than electromagnetic coupling since interactions are based on charge and the work required to add charge to a particle. With optical coupling, the interactions are due to the perturbation of the plasmon resonance.

Electrochemical methods that investigate charge interactions are not new. Nearly 30 years ago, di-ruthenium molecules were made with different distances between the metal centers¹. These Creutz-Taube complexes were the first to establish mechanisms for charge transfer. The interactions were found to be electrostatic when the metal centers were far apart, or quantum mechanical when very near. Some of these experiments have been performed on large (micron-scale) lithographically prepared quantum dots² with similar results. Electronic coupling between metal nanoparticles could bridge the size gap between the molecular scale and the micron scale. This chapter describes the electronic coupling between linked nanoparticles as a function of distance.

The literature is full of studies of reversible redox reactions of bridged dinuclear metal complexes². These investigations have probed the mixed-valence charge states. The type and magnitude of interactions between metal centers determine the electrochemical and spectral behaviors. These interactions are

determined by the degree of electron delocalization between metal centers. Lets start with a simple explanation of these interactions.

A single metal center will change charge at a given energy, $\Delta E_{1/2}$. In a molecular system this is a redox event. In a nanoparticle this is a charging event based on the capacitance of the particle. The energy required to change the charge on a particle is found using the relationship, $\Delta E=e/C$ (7.1) where e is the fundamental charge and C is the capacitance. As two metal centers, or nanoparticles, move close together there is some interaction between them. The type of interaction depends on the distance between the metal centers.

One type of interaction is electrostatic. This can be explained by simple classical equations⁴. Let's begin by starting with two metal centers, i and j . These centers are held together by some rigid bridge at a fixed distance, with the same charge. In this example we begin with the charges both neutral, $0/0$. The work required to charge i in the presence of j is $W_a=Q_iQ_j/4\pi\epsilon\epsilon_0R_{ij}$ (7.2). Next we change the charge on one particle so there is a mixed valence state, $0/+1$. The work to change the charge of one particle is $W_b=Q_i(Q_j+1)/4\pi\epsilon\epsilon_0R_{ij}$ (7.3) The difference in work to change these charges is then given as:

$$\Delta W = W_b - W_a = Q_i/4\pi\epsilon\epsilon_0R_{ij} \quad (7.4)$$

Q is the charge in coulombs on the respective metal center, ϵ is the dielectric constant of the surrounding medium, ϵ_0 is the permittivity of a vacuum and R is the separation distance between metal centers. Equation 7.4 tells us that the work required to split the valence state is dependent on the existing charge of the first

particle and inversely proportional to the distance separating the metal centers. It also tells us the resulting redox wave associated with the change in charge is split according to $\Delta E_{1/2} = 1/4\pi\epsilon\epsilon_0 R_{ij}$ (7.5). The peak splitting will increase as the bridge length is decreased. This splitting can be measured by deconvoluting a broadened peak using special techniques⁴ or spectroscopic measurements⁵ of charge transfer bands.

Another type of interaction between particles is exchange coupling. This is also known as delocalization or the electron (or hole) is free to roam back and forth between metal centers. This has been described as putting a $1/2$ charge on each coupled metal center. This can occur when the metal centers are incredibly close to one another or when the bridge has no energy barrier for the electron to cross.

In reality, there is no exact transition between electrostatic and delocalized coupling. There is usually a mixture between the two. The degree of comproportionation, K_c , tells the amount of interaction between metal centers. The interactions are largely electrostatic, however it is nearly impossible to distinguish between effects due to coulombic interactions or delocalization. A large K_c value means that entirely electrostatic interactions are present^{1a}.

Many studies have been done that show interaction between metal centers. Taube and co-workers first showed this¹. Their work showed electrochemical splitting from Di-ruthenium complexes. While this work started it all there are literally thousands of papers that cover the subject of poly-nuclear charge transfer. Many different bridges have been used that cover a wide range in inter-nuclear

distance and ability to transport electrons through the bridge. The work generally shows the same interactions. The inter-nuclear coupling is decreased as the distance is increased or the conductivity of the bridge is decreased. Examples can be found in the work of Ferrere⁴ and Bottomly⁷.

Most electrochemical studies have been done on molecular systems. There have been a few done with metal nanoparticles. Electrochemical studies of nanoparticles are experimentally difficult. The first major obstacle is size dispersity. Nanoparticles must all be the exactly the same size in order to observe charging events. Even most “monodisperse” particle samples have the accepted 5-10% size variations. This variation will cause the characteristic peaks to wash together and not be observed. Murray’s group developed a way to synthesize octane thiol coated nanoparticles based on the Brust Prep. Their adaptation uses a size selective precipitation method to obtain very monodisperse nanoparticles⁸. These thiolate-protected colloids also overcome the problem of stability often associated with nanoparticle sols.

The monodisperse nanoparticles charge with the same energy. This coherent charging of single particles is possible due to the narrow size distribution. The particles are all the same size; therefore, they all have the same capacitance. Performing electrochemistry, in the form of Differential Pulse Voltammetry (DPV), shows individual reversible charging peaks as electrons are added or removed from the particles. We will use these charging peaks to investigate the electronic coupling between nanoparticle dimers. The theoretical full width at half-maximum

(FWHM) for the peak shape is given as $90m^9$. Common values given in the literature and in our lab show the FWHM to be 112mV. The increase arises from the slight monodispersity issues and also the slower diffusion associated with a dense metal particle. Changes in peak shapes will give clues as to the type of interactions between coupled nanoparticles.

As described above interactions between particles will cause the charging peak to split. The type of splitting will allow us to determine the mechanisms of interactions between the particles. Several cartoon examples of the types of peak splitting are shown in Figure 7.1. When an electrostatic mechanism is dominant, the type of splitting should resemble Figure 7.1A. The first peak will charge with the same energy as a single, uncoupled particle. The second particle will then charge with a higher energy. The magnitude of this splitting is dependent on the

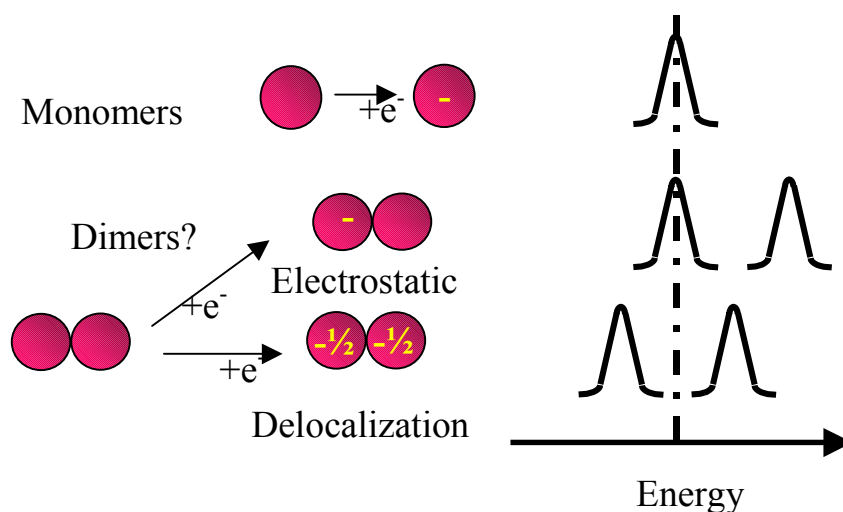


Figure 7.1. Possible mechanisms for peak splitting for redox events on coupled nanoparticle dimers. Also shown are possible shifts in the voltammogram that would be observed based on each mechanism.

interaction between particles and is described by K_c . When a delocalized mechanism is dominant we would expect to see splitting like Figure 7.1B. This splitting should be symmetrical with respect to the initial charging energy. The first particle would charge at a lower energy compared to an uncoupled particle. This is due to the added electron being able to freely roam between adjacent particles. There is still a splitting associated with the coupled particles. The magnitude of this splitting should be close to the same energy as the electrostatic mechanism. That is because the amount of work required to add that second electron is the same. This is represented in equation 7.1. A third mechanism could be one of stabilization. This mechanism is modeled after the analogous electromagnetic coupling. The longitudinal mode, where electrons couple along the long axis of a linear array of particles, shows a lower energy compared to a single particle. If this mechanism could take place, the entire energy of the dimer would be lowered. This would manifest itself with a shift to lower overall energy of the system.

Experimental

Alkane-thiol coated nanoparticles were synthesized in our lab using the methods of Murray and Brust⁸. These particles were then size selectively precipitated using the method outlined by Murray. The nanoparticles were then linked and reprecipitated to isolate the linked dimers as follows. 28.3 mg thiolate colloids were dissolved in 5 ml of 50 mM Bu_4NClO_4 . The sample was then split into two equal parts. 50 μ l of a 1M linker (PA7-2 and PA3-2) solution was added

and each sample stirred for three days. Upon completion the solvent was removed and the sample suspended in 2ml toluene and 1ml acetone (cut 1). After sitting overnight, the sample was centrifuged for 30 minutes at 1800 rpm. After centrifugation, the supernatant was removed via pipette. The leftover plug of particles was suspended in 2.5 ml of 50mM Bu_4NClO_4 . This procedure was repeated using 1ml toluene, 1ml acetone (cut 2) and then again with 1ml acetone/2ml toluene (cut 3). The solvent was removed from the remaining supernatant to make cut 4. DPV was run on each sample.

Monodisperse PPh_3 coated particles were also measured for electronic coupling. These were synthesized in our lab as follows: The precursor $(\text{PPh}_3)_3\text{AuCl}_2$ was made starting with 20 ml of 1% HAuCl_4 (aq) and 20ml 95% EtOH. This solution was added dropwise while stirring rapidly to 0.62 g PPh_3 in 100ml EtOH. The mixture was stirred for 3 hours and then solvent removed by rotary evaporation to obtain white crystals. The remaining PPh_3 is needed for capping layers in the reduction step. 101.4 mg of $(\text{PPh}_3)_3\text{AuCl}_2$ was dissolved in 50 ml EtOH. The Au salt was reduced with 3 ml of 0.5 mg/ml NaBH_4 (aq) added dropwise to the stirring solution. The mixture was stirred for an additional 2 hours then the solvent removed by rotary evaporation. The remaining orange solid was dissolved in 3 ml benzene and refrigerated overnight. The mixture was filtered through a medium glass fritted funnel and washed with an additional 3 ml of benzene. The solvent was then removed and the particles dissolved in 6 ml DCM.

The resulting solution was examined by DPV before linking. The sample was split equally into two samples. To each was added 20 μl of 2M KOH in EtOH and 50 μl of 1 μM linker (PA3-2 and PA7-2) solution and stirred overnight. The solvent was removed and the sample dissolved in Benzene then extracted with water. The solvent was removed from the resulting organic phase and redissolved in 1.5 ml electrolyte solution.

Differential Pulse Voltammetry (DPV) (10mV/S scan rate, 5mV step height, 50mV pulse height, 50mV pulse width) was used to obtain the charging peaks. All samples were dissolved in 0.05M Bu_4NClO_4 in CH_2Cl_2 . The samples were purged with argon for 5 minutes prior to scans. Usually the volume was adjusted to accommodate the evaporation during the degas phase. The window scanned was from 400mV to -600mV for the alkane thiolate samples and +1V to -1V for the phosphine samples. Wider windows allowed the peaks to be buried in noise. A PAR 273A potentiostat and corresponding software (M270, V4.3) was used to obtain the data. The data was exported to Kaleidagraph software for graphing.

Results and Discussion: Thiolate Covered Particles

Figure 7.2 shows a DP voltammogram for 2 nm, monodisperse, unlinked nanoparticles. This voltammogram shows periodic peaks associated with the collective charging of the nanoparticles. The peak splitting is consistent and equal to about 300mV. This is the monomer sample with no interaction between

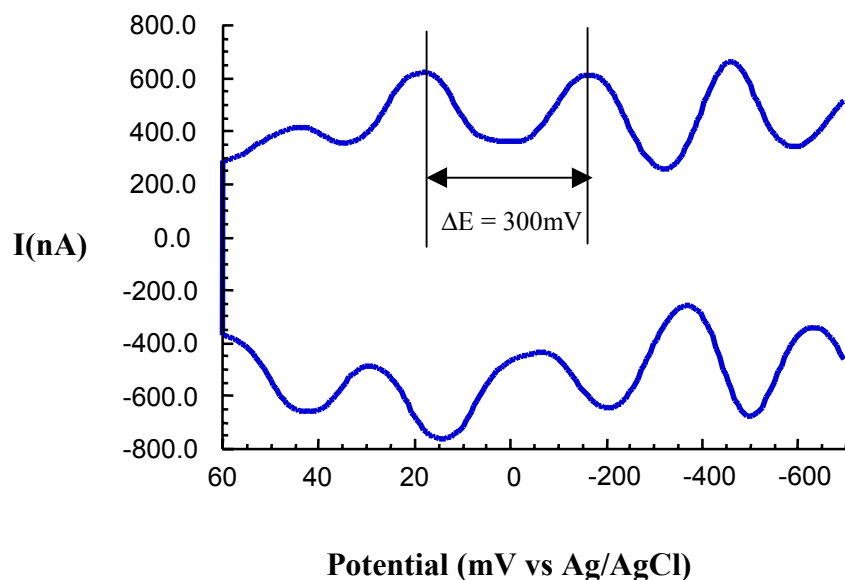


Figure 7.2. Differential pulse voltammogram of C8-SH coated Au nanoparticles.

particles. Figure 7.2 shows the same trace of monomers overlaid with the trace for the nanoparticle dimers linked with the PA7-2 dithiol linker. As can be seen there is no change in the peak positions. Figure 7.3 shows the monomer voltammogram overlaid by the dimers linked with the PA3-2 dithiol linker. The voltammogram from the linked particles clearly shows a shift in position.

The monomer samples have an infinite interparticle distance. That is to say that they are far enough apart to prevent any interaction between particles. Figure 7.3 shows that there is no change in the voltammogram as nanoparticles are brought within 7 nm, using PA7-2. This distance is the center to center distance and includes the length of the linker and the radii of two adjacent particles. We believe that the nanoparticles are still sufficiently far enough apart to prevent any electronic interactions. We contrast this to the electromagnetic experiments, discussed in Chapter 4, where interaction was observed at this distance. We

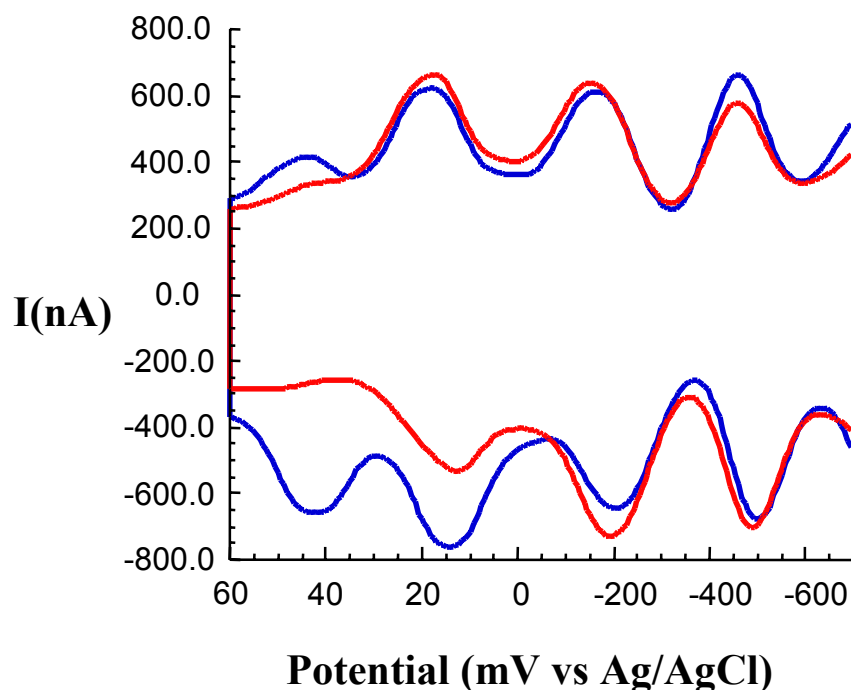


Figure 7.3. Differential Pulse Voltammogram of C8-SH coated Au nanoparticle dimers. Monomer(blue) and PA7-2 dimers(red) taken in 50mM Bu_4NClO_4 in DCM.

believe that interactions are not observed in this sample as the particles are much smaller in diameter and the nanoparticles are coated with an insulating octane thiol layer.

When the interparticle distance is decreased to 4.2 nm using the PA3-2 linker an obvious shift is seen in the voltammogram. Based on the open circuit potential (+220mV vs. +168mV), we believe that the curve is shifted to a more positive position. While we have not yet figured out a way to verify the direction of shift we will make assumptions based on this direction. The shift to more positive potentials tells us that it requires less energy to charge a particle than before they were linked. This suggests some coupling between particles is observed. This has been observed in di-iron systems^{2b}. We also suspect coupling

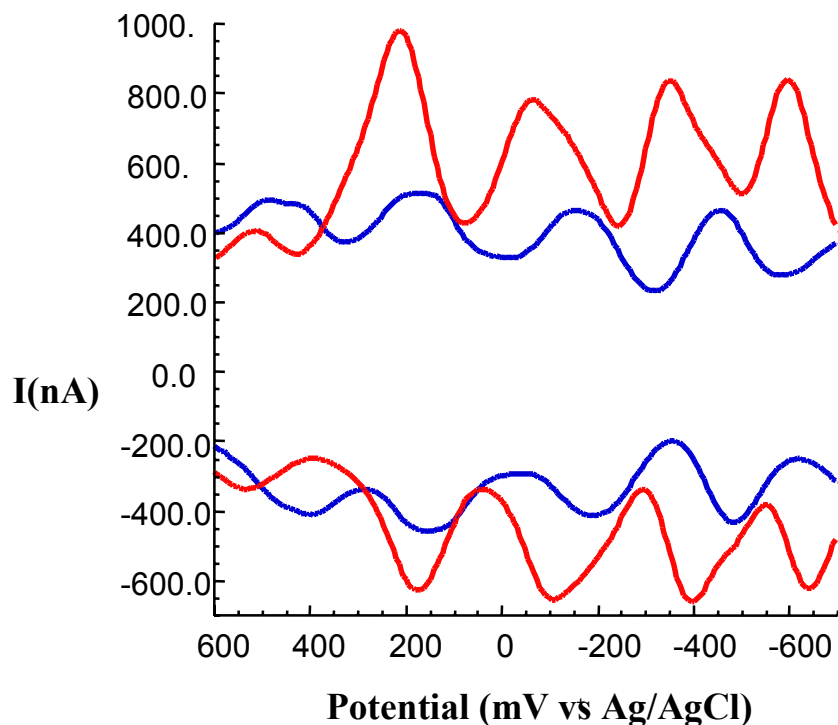


Figure 7.4. Differential Pulse Voltammogram of C8-SH coated Au nanoparticle dimers. Monomer(blue) and PA3-2 dimers(red) taken in 50mM Bu_4NClO_4 in DCM.

based on the increase in peak width and the appearance of shoulders on some of the peaks. It has also been suggested that these shifts could be due to a difference in ligands^{2b}.

One way to explain these results would be to study more bridge lengths. The other lengths available are a PA9 and benzene dithiol. These experiments were not performed for several reasons. Since the PA7-2 linker did not show any interaction, the longer chain would probably not show any interaction. A shorter linker is needed. The shorter benzene dithiol is not long enough. While the aromatic thiol would easily displace the alkane thiolate on the particle¹¹, the length would prevent it from linking particles. The linker would have to be at least twice as long as two octane thiol capping ligands. The linker has to penetrate the layers

on two particles for linking to occur. This prompted us to look at particles with the possibility of greater interaction.

Results and Discussion: PPh₃ Particle Dimers

Due to the highly insulating effects of a tightly packed alkane thiolate layer on a nanoparticle, 2.3nm particles with PPh₃ layers were synthesized. The PPh₃ capped particles should show a difference in the voltammetry compared to the thiolate covered Au based on the capping ligand. The phosphine should attach like an umbrella, one point of attachment from the lone pair of electrons on the phosphorous and a large coverage layer from the phenyl rings. This limits the damping of the surface electrons by the ligand. As these surface electrons might be less damped, there is a possibility of greater interactions between nanoparticles in an array.

Voltammograms of the PPh₃ coated nanoparticles are shown in Figure 7.5. This figure has three overlaid plots. Only the forward scans are shown for clarity. The green line is the monomer particles. These are unlinked and are sufficiently far apart to have no interaction. The voltammogram shows two charging peaks from the nanoparticles. The second curve (blue) is a sample combined with the PA7-2 linker. The third curve (red) the nanoparticles combined with the shortest bridge, PA3-2. This curve shows two peaks that are shifted to more negative potentials compared to either the monomers or the longer linker.

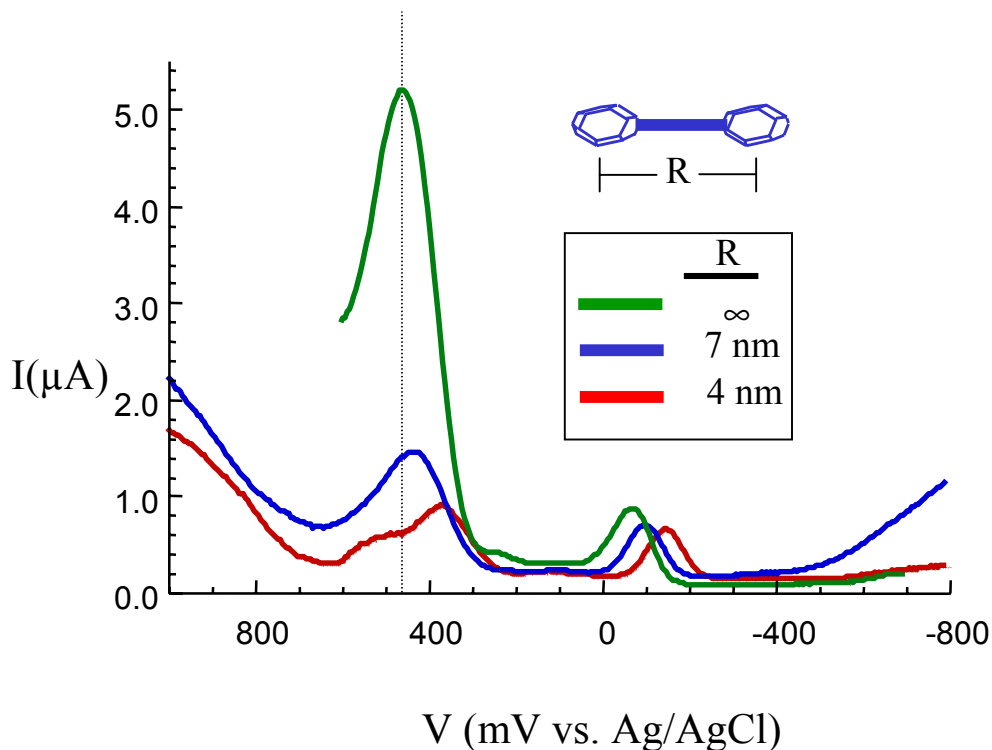


Figure 7.5. Differential Pulse Voltammogram of PPh_3 coated Au nanoparticle dimers versus separation distance. Monomers (green), PA7-2 (blue) and PA3-2 (red) scans taken in 50 mM Bu_4NClO_4 in DCM.

Looking more closely at these voltammograms, we observe several key factors. (1) The peaks do not have the same magnitude of current. We believe this may be due to changes in concentration between samples or the monodispersity within samples. It has also been shown that the voltammetry of nanoparticles still shows some unexplained results. One example from Murray's group⁸ shows current fluctuations within a sample that have been observed, yet unaccounted for. (2) Compared to the alkane thiolate covered Au, there are fewer electrochemical peaks. This could be due to the size difference between the two samples or the change in capping layer, phosphine vs. thiolate. (3) The curves for the PA3-2 sample shows even more changes than just the shift in potential. The left peak

(more positive) appears to split whereas the right peak (more negative) does not.

We are still unable to explain this but the splitting is addressed below.

The data suggests that the shift to more negative potentials is electrostatic in nature. This explains the shift to higher energy as suggested in Figure 7.1a. The longer linker the data for the 4 nm separation shows a shift to more negative potentials possibly showing increased interaction. The lower energy peak around 475 mV shows something a little different. This peak is marked with a vertical line at the position of the unlinked particle solution. The large intensity of the monomer solution is not yet explained.

The marked peak appears to have some type of splitting. The splitting appears to be symmetric with respect to the initial charging energy of the monomer. This splitting is not seen in the other peak. This could be due to equation 7.1. The change in work required depends on the charge on the particle. As the charge changes on the particle, the splitting should also change. The symmetric splitting in the low energy peak appears to be like the expected splitting from figure 7.1b. The splitting is characteristic of a more delocalized system, if we consider the overall peak position unchanged from the value of the unlinked sample. Therefore, it appears the peak does not shift consistent with a delocalized mechanism. The peak splitting is due to coulombic (electrostatic) repulsion between particles^{2b,d}. If the peak splitting is based solely on coulombic repulsion, then it appears there are electrostatic interactions between particles. The samples for the PA7-2 linker do

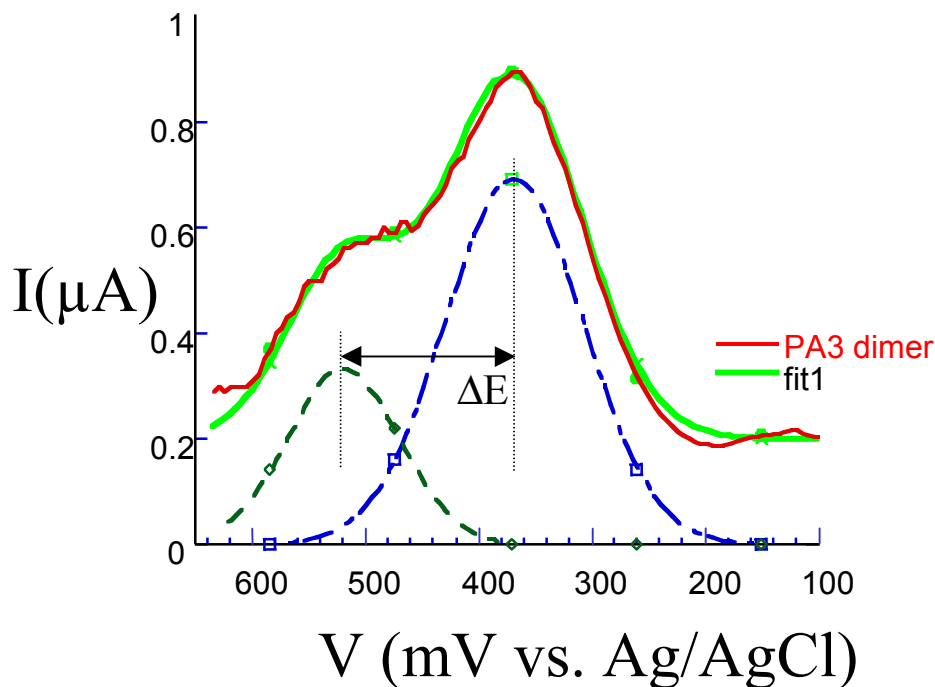


Figure 7.6. Data fit(green) to voltammogram(red) of PA3-2 linked PPh₃ coated Au nanoparticles. Deconvolution shows $\Delta E = 150$ mV

not show this behavior. This may be due to a smaller splitting that is buried within the peak width. We can take a closer look at this split peak.

Changing the scale allows us to zoom in on the peak that appears to be splitting. The red line in Figure 7.6 is the actual data. Summing two gaussian curves made a calculated fit. These curves were summed with a constant for background current and the resulting fit shown in green. This is an oversimplified method for deconvoluting the combined peaks. While not a rigorous treatment of the data fit, qualitative look at the peak splitting can result. The $\Delta E_{1/2}$ value is determined to be about 150mV.

Table 7.1 shows some calculated splitting for different interparticle distances based on equation 7.2. The value of the dielectric constant is that of benzene. This is close to the PPh₃ capping layer of the nanoparticle surface. The

trend shown in Table 7.1 reveals what we expect. As the interparticle distance decreases, the peak splitting increases. The peak splitting value for the longer linker is calculated to be about 80mV. When the distance is 4 nm, as for the PA3-2 linker, the peak splitting is calculated to be 158mV. This is remarkably similar to the 150mV obtained by the simple deconvolution of the split peak. Of course, we have to remember that the dielectric constant chosen may be different than our

Table 7.1 Calculated peak splitting

$\Delta E = e/4\pi\epsilon_0\epsilon R$	
$\epsilon = 2.28$	
ΔE (mV)	R (nm)
42	15
80	8
158	4
211	3

actual system. Small changes in the value for the dielectric constant can produce large changes in the peak splitting. Using peak splitting to back-calculate a dielectric constant may be one way of determining the interactions between particles.

Conclusions

These experiments represent, to the best of our knowledge, the first evidence of interparticle coupling in a solution based nanoparticle system. The data follows trends seen in coupled molecular systems. We see that the peaks, in both the alkane thiolate covered nanoparticles and phosphine-coated nanoparticles,

shift to higher energy. This is characteristic of electrostatic interactions. While not visible in the alkane thiolate particles, the phosphine coated particles exhibit characteristics that suggest a switch to a delocalized mechanism. It is clear the amount and type of coupling depends on the dielectric medium between particles. Solvent inclusion into the phosphine layer may be another area to investigate.

In order for these mechanisms to be identified, additional bridge lengths need to be investigated. In addition, the role of the linker should be investigated. A more or less conjugated bridge would identify this or possible photo-electrochemistry involving exciting the bridge while changing the charge might shed some light on this quandary. Spectro-electrochemistry may also be useful. The presence of intervalence charge transfer bands may be observed.

Chapter Seven References

1. a) DE Richardson, H Taube, *Inorg. Chem.* **1981**, 20, 1978 b) JE Sutton, H. Taube, *Inorg. Chem.* **1981**, 20, 3125 c) F Salaymeh, S Berhane, R Yusof, R de la Rosa, EY Fung, R Matamoros, K Lau, Q Zheng, EM Kober, JC Curtis, *Inorg. Chem.* **1993**, 32, 3895 d) JE Sutton, PM Sutton, H Taube, *Inorg. Chem.* **1979**, 18, 1017
2. a) S Nagaraja, JP Leburton, RM Martin, *Phys. Rev. B*, **1999**, 60 (12) 8759; b) Waugh, et al, *Phys. Rev. Lett.* **1995**, 75, 705
3. There are possible thousands of examples. Here are some selected papers. a) RJ Crutchly, *J. Adv. Inorg. Chem.* **1994**, 41, 273; b) C. Creutz, *Prog. Inorg. Chem.* **1983**, 30, 1; c) AC Benniston, V Goulle, A. Harriman, JM Lehn, B Marczinke, *J. Phys. Chem.* **1994**, 98, 7798; d) MA Haga, MM Ali, S Koseki, K Fujimoto, A Yoshimura, K Nozaki, T Ohno, K Nakajima, D Stufkens, *Inorg. Chem.* **1996**, 35, 3335.
4. S Ferrere, CM Elliott, *Inorg. Chem.* **1995**, 34, 5818 b) S. Ferrere, PhD Thesis, Colorado State Universtiy, **1994**
5. CM Elliott, DL Derr, S Ferrere, MD Newton, YP Liu, *J. Am. Chem. Soc.* **1996**, 118, 5221
7. LM Tolbert, X Zhao, Y Ding, LA Bottomly, *J. Am. Chem. Soc.* **1995**, 117, 12891
8. a) AC Templeton, WP Wuefling, RW Murray, *Acc. Chem. Res.* **2000**, 33, 27 b) S Chen, RS Ingram, MJ Hostetler, JJ Pietron, RW Murray, TG Schaff, TG Khoury, MM Alvarez, RL Whetten, *Science*, **1998**, 280, 2098 c) JF Hicks, AC Templeton, S Chen, KM Sheron, R Jasti, RW Murray, J Deburd, TG Schaff, RL Whetten, *Anal. Chem.* **1999**, 71, 3703 d) JJ Pietron, JF Hicks, RW Murray, *J. Am. Chem. Soc.* **1999**, 121, 3303
- 9 AJ Bard, LR Faulkner, Electrochemical Methods: Fundamentals and Applications, 2nd Ed., John Wiley and Sons, NY, **2001**
10. JP Novak, DL Feldheim, Unpublished results. ¹H-NMR experiments show that thiophenol will bind to a fully coated octane thiol nanoparticle at room temperature.

Chapter 8

Separation Methods for Templated Nanoparticle Arrays

Introduction

Working with nanoscale materials includes aspects of engineering and physics than more traditional chemistry. As chemists we continue the normal lab processes, such as reactions and separations even when working on a non-molecular scale. As new methods for designing nanoparticle based structures are developed, methods for purification struggle to keep up. This chapter describes a separation method that enhances the concentration of mixed solutions of linked nanoparticle arrays.

Nanoparticles have been used as building blocks for more complex nanostructures¹. Organic linkers were used to form nanoparticle arrays with discrete numbers of particles². The linkers allow for control over symmetry and interparticle distance. These methods only provide a relatively low yield in order to retain control over the linking conditions. Normal methods for separation do not allow for the desired structures to be isolated from the starting materials. This is due to particle stability.

Most aqueous based nanoparticles are unstable towards aggregation. Changes in ionic strength, solvent composition, and capping ligands can have dramatic, damaging effects on the solutions. Generally this causes the nanoparticles to aggregate together to form large clumps which become insoluble and thus useless to any further measurement. There have been several attempts at overcoming this stability problem. These generally involve capping the surface with a chemically bonded adsorbate, in most cases this is an alkane thiolate³.

These thiolate layers can make the nanoparticle soluble and stable in organic and aqueous solvents. These layers increase stability to the point of being able to perform wet chemistry techniques such as separations that are generally not possible due to low stability. The down side is that these thiolates damp the plasmon resonance⁴. This effectively removes most of the optical properties that are desirable in a nanoparticle-based structure.

As chemists, one of the duties of synthesizing new products is purification. However, due to their instability there are few examples that show separation of solution based nanoparticles. One method involves increasing the stability of the nanoparticles by capping with a water soluble phosphine, $\text{Ph}_2\text{P}(\text{PhSO}_3^-\text{Na}^+)_2$. The then capped particle aggregates were separated using capillary electrophoresis⁵. Other methods involve using surfactants or polymers to coat the nanoparticles or separating medium⁶. This was applied to separate nanoparticles from nanorods in one solution. While both of these methods seem to work, there is one major disadvantage to them. Only small amounts of solution can be separated. Due to the large number of structures required, these methods would not work if device applications are in the future. This chapter outlines two methods for nanoparticle separations. One strategy for separation involves centrifugation. Using a viscous medium to slow down the rate of migration, the fractional composition of nanoparticle arrays can be increased. The second method uses Size Exclusion HPLC (HPLC-GPC) to separate nanoparticle arrays based on size.

Experimental

Gold nanoparticle dimers and trimers were synthesized according to previous methods described in Chapter 3. 6 ml of the linked samples were mixed with 1mg/ml of $\text{PhP}(\text{PhSO}_3^-)_2$ and stirred for 3 hours. This solution was then transferred to a glass centrifuge tube and concentrated by centrifuging for 60 minutes at 6000 rpm. Approximately 5 ml of the supernatant was removed by pipette. This now concentrated nanoparticle solution is ready for separation.

2.00ml of 1M sucrose in water was added to a 12ml glass centrifuge tube. 100 μl of the concentrated nanoparticle was carefully added to the surface of the sucrose. A thin, ruby red disk should now appear on the surface of the sucrose solution. The nanoparticle solutions were then centrifuged for 30 minutes at 2000 rpm. Upon removal the samples have started to migrate toward the bottom of the tube. Most of the nanoparticle solution is still present at the top of the liquid. The solution was then spun for 30 minutes at 2500 rpm. At this point there was a dark precipitate present in the apex of the centrifuge tube. The collected plug was removed by carefully drawing into a pipette. Only as much sample was removed to ensure the plug was drawn into the pipette, usually about 2 drops. The collected fraction was then rinsed from the pipette into a vial with water. This same procedure was repeated while increasing the speed 500 rpms after every step until 5500 rpms. This procedure was carried out for nanoparticle dimers, trimers, and tetrahedral tetramers. Fractions obtained using this separation method were analyzed by TEM.

HPLC methods were developed using ideas from the work of Wang and co-workers⁶. They used a surfactant mobile phase to prevent irreversible adsorption of nanorods onto the column. A concentrated sample, as prepared above, was injected (25 μ l) into the GPC system. The system consists of a Waters UK6 injector, Waters 590 programmable solvent pump, and Rainin Dynamax UV-C UV-VIS absorbance detector set at 525nm. Two columns (Alltech Inc., Microsphere GPC, 500Å and 350Å pore size) were mounted in series. Mobile phase is 40mM SDS, degassed with argon. For development purposes, three samples were used. 10nm Au, 30nm Au, and a mixture containing 5 drops each of 10 and 30 nm.

Results and discussion: Centrifugation

Looking at these samples with TEM reveals some interesting results. The fractions obtained first show the very few aggregates that have more than four particles. As the speed was increased, the particle aggregates decreased in number. About 3500-4000 rpms was the optimal speed for separation. The left image on Figure 8.1 shows a TEM image of nanoparticle trimers obtained from the fraction spun at 3500 rpms. Figure 8.1 (right) shows a TEM image of nanoparticle dimers obtained from spinning at 4000 rpms. Both of these images show large compositions of the desired structures. It is interesting to note that the trimers did indeed spin out at a lower speed than the dimers. This is consistent with the mechanism of separation. The larger aggregates of nanoparticles obviously contain more nanoparticles. This increased number of particles increases the weight by a

factor equal to the number of particles. A trimer would be 3 times more massive than a monomer. This difference in mass is why the particles separate out.

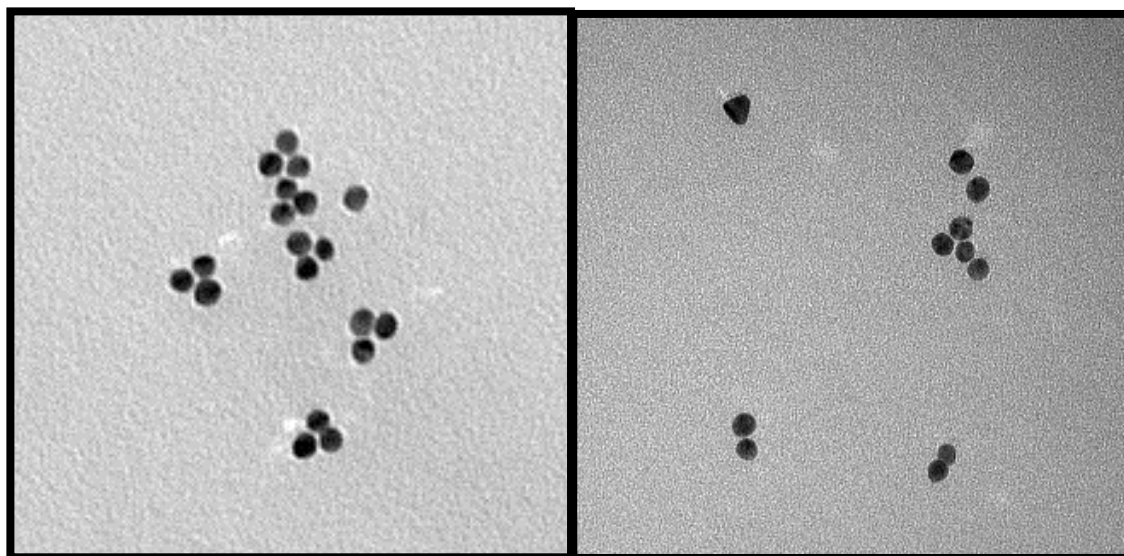


Figure 8.1. Transmission Electron Microscopy images of trimer(left) and dimer(right) Au nanoparticle arrays separated by centrifugation.

The separation of these nanoparticles has increased the fractional composition of the desired structures. Figure 8.2 shows a histogram of particle dimer yields before and after the separation. The graph shows the number of

Table 8.1. Percentage of nanoparticle arrays before and after separation by centrifugation.

sample	monomer	dimer	trimer	tetramer
di-thiol	70%	30%	0%	0%
di-thiol sep.	26%	51%	13%	10%
tri-thiol	53%	18%	24%	5%
tri-thiol sep.	20%	13%	55%	12%

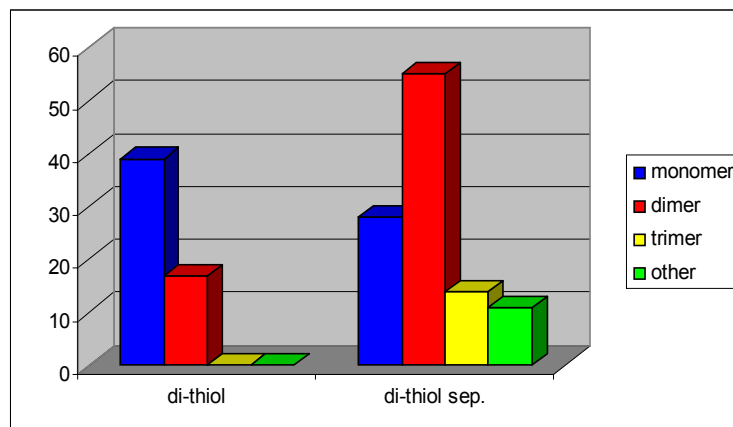


Figure 8.2. Histogram noting TEM nanoparticle dimer array concentration pre-(left) and post-(right) separation. Desired nanoparticle array concentration is increased by separation.

structures of each of monomers, dimers, trimers, and other structures. Other structures include larger numbers of aggregates. Table 8.1 summarizes the separation effectiveness. The di-thiol linker shows that there are 30% dimers and 70% monomers. This is consistent with previous numbers discussed in Chapter 3. Likewise, no other symmetries are observed. The separation shows an increase in dimers to 51%. The remaining structures are 26% monomers, 13% trimers, and 10% other. These numbers show that the centrifugation technique works for nanoparticle dimers.

Figure 8.3 shows a histogram for 10 nm nanoparticle trimers. Before separation, the trimers consist of 24% of the sample. Like the dimers, the main components are the unreacted dimers and desired trimers. Post separation, the composition of trimers jumps to 55% and is by far the main component. The remainder of the sample is still comprised of monomers, dimers, and other structures although they are at much smaller contributions.

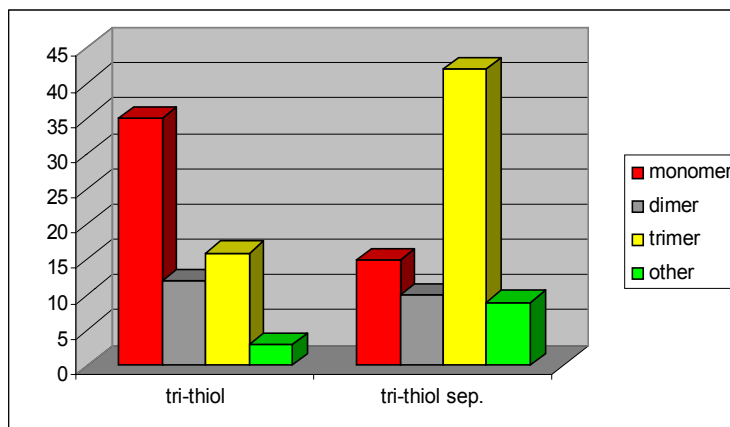


Figure 8.3. Histogram noting TEM nanoparticle trimer array concentration pre-(left) and post-(right) separation. Desired nanoparticle array concentration is increased by separation.

Tetrahedral samples were also separated using this method. The initial composition was 43% monomer, 19% dimers, 26% trimers, and 12% tetrahedral structures. The separation has been done and awaiting analysis by TEM. This data will be included in the final version of this dissertation.

Interesting aspects of these histograms are the changes that take place during the separation. For example, the dimer solution before the experiment does not show any trimers or other structures. The sample is limited completely to monomers and desired dimers. The post-separation sample has a number of these higher order aggregates. We believe that this is due to the centrifugation process. In order to separate these particles, they pack tightly in the bottom of the centrifugation tube. This might cause them to stick together. It is also interesting to note that the samples, when analyzed by TEM show many aggregates that look like dimers stuck together. It could be that the composition of dimers is higher than shown due to

these aggregates of dimers being counted as “other”. Similar observations were seen for the trimer samples.

Results and Discussion: HPLC-GPC Methods

Developing methods for nanoparticle separation proved to be quite difficult. When flowrates were 2.0 ml/min, individual nanoparticle solutions were eluted at different times (30s difference, not shown). When the mixture of particles was injected, Only one peak was present showing no separation of the 10 and 30 nm nanoparticles. Careful consideration brought forth one possibility.

Chromatography is based on mass transport and diffusion. It has been shown that nanoparticles have slow diffusion in electrochemical experiments⁷. Decreasing the flow rate would increase the particle/column interaction by increasing retention times. Separations were finally achieved at 0.25 ml/min.

The chromatograms for nanoparticle separations shown in Figure 8.4 were run at 0.25 ml/min. Test samples consisting of 10 nm, 30 nm, and a mixture of the two sized nanoparticles were developed. The curve (Figure 8.4a) of the 10 nm Au nanoparticles shows a small bump at 13:30 min. and a peak at 17.30. The 30nm Au nanoparticles elute with a single peak at 16:10 min. The mixture of the two samples shows a shoulder and two peaks with their retention times matching those of the individual samples of 10 nm and 30 nm nanoparticles, respectively.

The shoulder that is present on the 10 nm Au chromatogram is attributed to aggregation. This particular sample had been sitting on the bench top for several

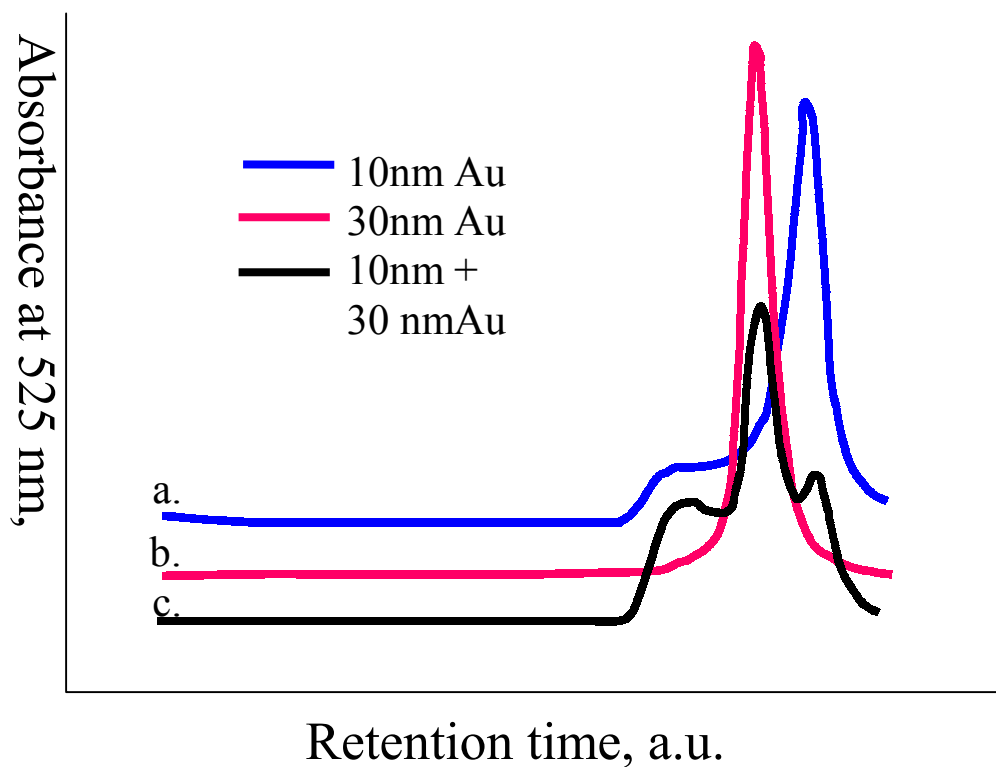


Figure 8.4. HPLC-GPC Chromatograms of a) 10nm Au, b) 30nm Au, c), d) mixture of 10nm and 30nm Au, and e) 10nm trimers.

months. The nanoparticle solutions are known for their instability. It appears that the spontaneous aggregation is now shown as a peak that elutes prior to our known sizes. These aggregates should be a larger size than the 30nm nanoparticles due to the shorter retention time. If this shoulder is indeed due to the aggregation, it may lead to a quick method for identifying and subsequently, removing the aggregation in a nanoparticle solution. These results show that we are able to separate nanoparticles based on their diameters.

While separating individual particles of different sizes may be useful, it was our intention to separate linked nanoparticles of the same size. The test system

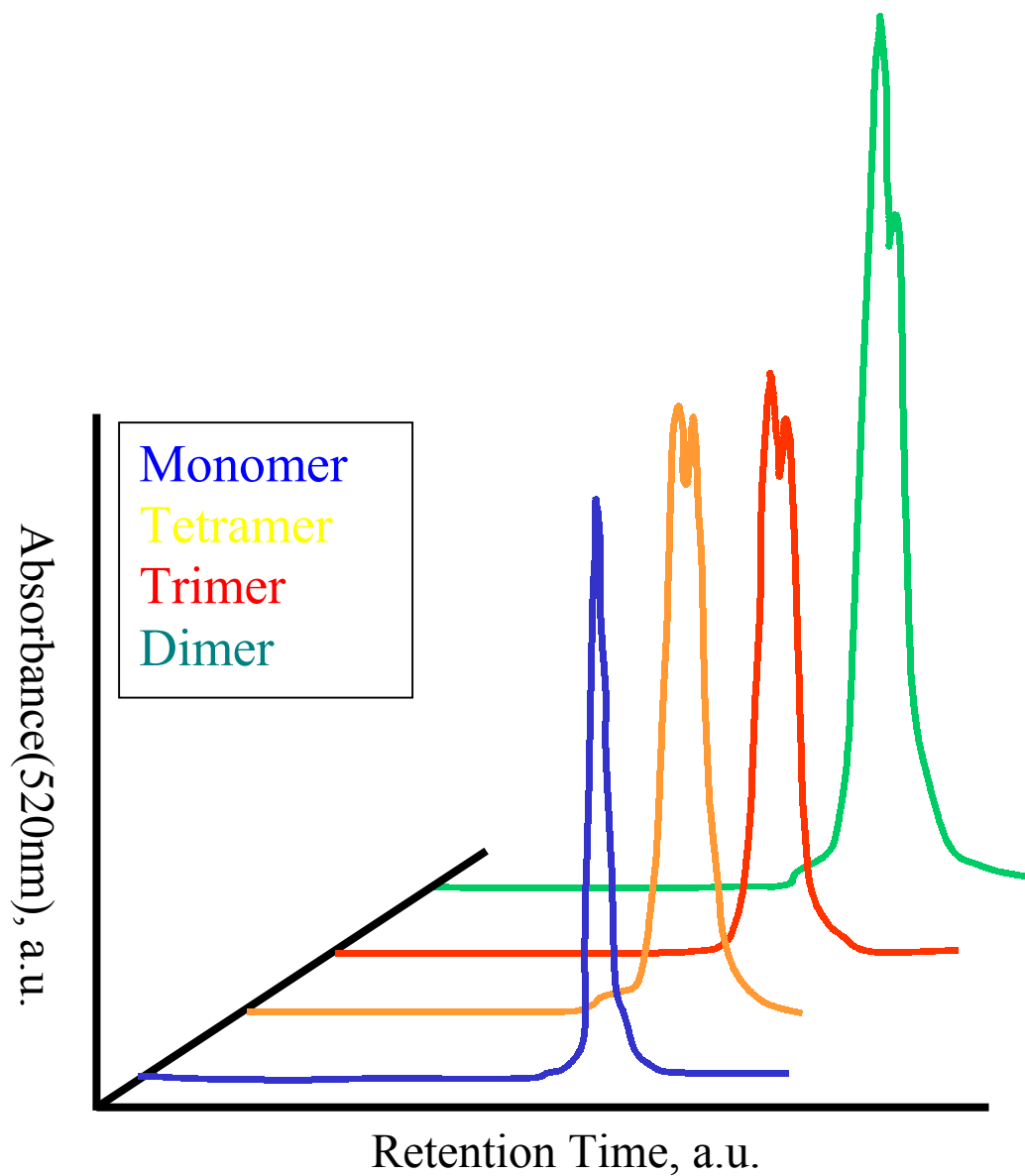


Figure 8.5. Separation of Au nanoparticle monomers, dimers, trimers, and tetramer arrays using HPLC-GPC.

confirms a separation of 10 nm and 30 nm nanoparticles. These were chosen as the 30 nm size is close to the expected hydrodynamic radius of a 10 nm Au trimer.

Several linked samples have been prepared and separated.

Chromatograms of the separation of these linked nanoparticle arrays are shown in Figure 8.5. We see chromatograms from unreacted monomers, and linked dimers,

Table 8.2. Retention times of linked Au nanoparticle samples separated by HPLC-GPC.

Retention time (min)	
Monomer	18.3
Tetramer	17.1 18.0
Trimer	17.4 18.0
Dimer	17.7 18.3

trimers, and tetramers. With the exception of the monomer sample, each chromatogram shows a split peak, which suggests that the samples are separating using this method.

The retention times for these peaks are shown in Table 8.2. The peaks are labeled as peaks 1 and 2. Peak 1 elutes with the shorter retention time. Lets look at the second eluting peak 2 first. The retention times observed in all four samples are close to that of the unlinked sample. This suggests that the second peak could be due to the leftover monomers in the linked solution. There is also a trend in the first peak that suggests separation. The retention times for the tetramers are shorter than the trimers which are shorter than the dimers. This suggests that the tetramers, groups of four particles, spend less time than the trimers, groups of three particles. We would expect that a larger array would spend less time on the column than a

Table 8.3. Percent composition of fractions obtained during the separation of the dimer sample in Figure 8.5.

	monomer	dimer
Peak 1	32%	62%
Peak 2	73%	27%

smaller array. This is exactly what we observed. The retention times match our expected results but how do we identify sample composition?

Fractions of the dimer sample were taken during the separation. Each fraction was 5 drops of the eluent. The fractions were analyzed by TEM for sample composition. The results are shown in Table 8.3. The fraction that corresponds to the first peak eluted was composed of 62% dimers and 34% monomers. The fraction corresponding to the second peak had 27% dimers and 74% monomers. These results confirm our thoughts about separation. The first peak has a composition that is a majority dimers. This matches the shorter elution time. As we transition to the second peak we see that the composition is now overwhelmingly monomers. These results show that separation of linked nanoparticle arrays is possible. We expect that the other three samples will behave in a similar manner.

Conclusions

We have shown that nanoparticle aggregates can be separated based on the differential masses, centrifugation, and differential sizes, HPLC-GPC, between aggregates. The centrifugation method can isolate approximately 60% of the desired structures. HPLC methods generate similar yields. Either method should be considered if separation of nanoparticles is required.

While the separations are not perfect, they overcome the disadvantages of particle aggregation and adsorption usually associated with nanoparticle

manipulations. Each method should be easy to scale up to obtain usable quantities needed for future device applications. This is important when nanoparticle solutions are usually in 10^{-9} M concentrations. Isolation of pure fractions, or enhanced concentrations, of nanoparticle arrays could result in new results in the experiments designed to investigate nanoparticle interactions.

Chapter Eight References

1. AN Shipway, E Katz, I Wilmar, *CHEMPHYSICHEM*, **2000**, 1, 18; b) AP Alivisatos, *J. Phys. Chem.* **1996**, 100, 13226; c) AP Alivisatos, 1996, 271, 933; d) DL Feldheim, KD Keating, *Chem. Soc. Rev.* **1998**, 21, 1
2. a) LC Brousseau, JP Novak, SM Marinakos, DL Feldheim, *Adv. Mat.* **1999**, 11, 447; b) JP Novak, DL Feldheim, *J. Am. Chem. Soc.*, 2000, 122, 3979
3. M Brust, M Walker, D Bethell, JJ Schriffin, RJ Whymann, *Chem Comm.* **1994**, 801; RW Murray, et al *J. Am. Chem. Soc.*, **1996**, 118, 4212
4. MJ Hostetler, JE Wingate, C-J Zhong, JE Harris, RW Vachet, MR Clark, JD londono, SJ Green, JJ Stokes, GD Wingall, GL Glish, MD Porter, ND Evans, RW Murray, *Langmuir*, **1998**, 14, 17
5. X. Peng, TE Wilson, AP Alivisatons, PG Schultz, *Angew. Chem. Intl, Ed. Engl.* **1997**, 36, 145;
6. GT Wei, FK Liu, CRC Wang, *Anal. Chem.* **1999**, 71, 2085
7. AJ Bard, LR Faulkner, Electrochemical Methods: Fundamentals and Applications, 2nd Ed., John Wiley and Sons, NY, **2001**

Reflection

Looking back at the work that was performed for this dissertation, I am reminded of several key results. The main result is the novelty of these discrete nanoparticle arrays. From the synthesis of the linkers, to the solution phase assembly, these discrete assemblies with controlled interparticle distance and symmetry are the first of their kind. Being able to control these dimensions, in such a small domain, is incredible. Using the control over array symmetry and interparticle distance to study optical and electronic coupling is another key area.

It is still amazing to me that we can observe communication between such small groups of particles. It is even more amazing that these small entities show such a distance and symmetry dependence on this communication. Whether electronic or electromagnetic coupling, these particles communicate within an array so strongly that they can be measured without a pure sample. I knew this project would be special ever since I read the first theoretical calculations paper on optical coupling between nanoparticles, and realized that this research may have experimentally repeated some of these calculations.

As I look toward the future I see so many possibilities. If nanoparticles are to ever be used in some electronic device, I know that some of my research might make it possible, maybe not from a nanoparticle array assembly point of view, but from the fundamental interactions between particles. It is these interactions which could get in the way if billions of nanoparticles are integrated onto a surface and forced to produce a desired function.